https://doi.org/10.1070/RCR4889

New trends in the development of electrophoretic deposition method in the solid oxide fuel cell technology: theoretical approaches, experimental solutions and development prospects

Elena G. Kalinina,[a, b]* Elena Yu. Pikalova [b, c]

[a] *Institute of Electrophysics of the Ural Branch of the Russian Academy of Sciences, ul. Amundsena 106, 620016 Ekaterinburg, Russian Federation*
[b] *Ural Federal University named after the first President of Russia B.N.Yeltsin, ul. Mira 19, 620002 Ekaterinburg, Russian Federation*
[c] *Institute of High Temperature Electrochemistry of the Ural Branch of the Russian Academy of Sciences, ul. S.Kovalevskoy 22/ul. Akademiceskaya 20, 620137 Ekaterinburg, Russian Federation*

The key features and challenges of the use of electrophoretic deposition for the formation of functional layers of solid oxide fuel cells are considered. Theoretical models and experimental results of the studies of electrophoretic deposition are presented. The analysis covers the physicochemical deposition mechanisms, methods for preparing suspensions and conditions necessary for obtaining thin-film electrode and protective single- and multi-layers with both dense and porous structure for solid oxide fuel cells. The prospects of theoretical simulations of the method and its potential practical applications are evaluated.
The bibliography includes 282 references.

Contents

1. Introduction 1180
2. Theoretical approaches to the description of electrophoretic deposition. State of the art of the research 1181
3. Preparatory stages for the conduction of electrophoretic deposition 1189
4. Application of electrophoretic deposition in the solid oxide fuel cell technology. Achievements and prospects 1199
5. Conclusion 1214

The following abbreviations and designations are used in the review:

AFL — anode functional layer;

ASR — area specific resistance;

BCGCu — gadolinium- and copper-doped barium cerate, $BaCe_{0.89}Gd_{0.1}Cu_{0.01}O_{3-\delta}$;

BCS — samarium-doped barium cerate, $BaCe_{0.8}Sm_{0.2}O_{3-\delta}$;

BCY — yttrium-doped barium cerate, $BaCe_{0.9}Y_{0.1}O_{3-\delta}$ (BCY10), $BaCe_{0.8}Y_{0.2}O_{3-\delta}$ (BCY20);

BL — buffer layer;

BMC-5 — butyl methacrylate copolymer with 5 mol.% methacrylic acid;

BZCY — yttrium-doped barium cerate–zirconate, $BaZr_{0.4}Ce_{0.4}Y_{0.2}O_{3-\delta}$;

CC — current collector;

CGO — gadolinium-doped ceria, $Ce_{0.9}Gd_{0.1}O_{2-\delta}$ (CGO10), $Ce_{0.8}Gd_{0.2}O_{2-\delta}$ (CGO20);

CSO — samarium-doped ceria, $Ce_{0.8}Sm_{0.2}O_{1.9}$ (CSO20);

CSSBO — samarium-, strontium- and barium-doped ceria, $Ce_{0.8}(Sm_{0.75}Sr_{0.2}Ba_{0.05})_{0.2}O_{2-\delta}$;

CTE — coefficient of linear thermal expansion;

DLVO — Derjaguin–Landau–Verwey–Overbeek theory;

EDL — electrical double layer;

EPD — electrophoretic deposition;

FC — fuel cell;

FL — functional layer;

LEC — laser evaporation followed by condensation;

IEP — isoelectric point;

E.G.Kalinina. PhD, Senior Researcher at the IEP UrB RAS, Assistant Professor at the Department of Physical and Inorganic Chemistry, UrFU. Telephone: +7(343)267–8782, e-mail: kalinina@iep.uran.ru
Current research interests: solid oxide fuel cells, electrophoretic deposition, nanopowders, suspensions of micro- and nanoparticles, thin films, composites, adsorption.
E.Yu.Pikalova. PhD, Senior Researcher at the IHTE UrB RAS, Assistant Professor at the Department of Environmental Economics, UrFU. Telephone: +7(343)362–3194, e-mail: e.pikalova@list.ru
Current research interests: ceria-based materials, fuel cells, electrophoretic deposition, composites, cathode materials of solid oxide fuel cells, electrode kinetics.

Received 27 March 2019
Translation: Z.P.Svitanko

© 2019 Uspekhi Khimii, Russian Academy of Sciences and Turpion Ltd.

LASO — lanthanum aluminate silicate, $La_{9.83}Si_{4.5}Al_{1.5}O_{26}$;

LBAYO — barium- and yttrium-doped lanthanum aluminate, $La_{0.9}Ba_{0.1}Al_{0.9}Y_{0.1}O_{3-\delta}$;

LCN — calcium-doped lanthanum niobate, $La_{0.995}Ca_{0.005}NbO_{4-\delta}$;

LN — layered lanthanum nickelate, $La_2NiO_{4+\delta}$;

LNF — lanthanum nickelate ferrite, $LaNi_{0.6}Fe_{0.4}O_{3-\delta}$;

LSCF — lanthanum strontium cobaltite ferrite, $La_{0.6}Sr_{0.4}Co_{0.8}Fe_{0.2}O_{2-\delta}$, $La_{0.8}Sr_{0.2}Co_{0.2}Fe_{0.8}O_{2-\delta}$;

LSGM — strontium- and magnesium-doped lanthanum gallate, $La_{0.8}Sr_{0.2}Ga_{0.8}Mg_{0.2}O_{3-\delta}$, $La_{0.83}Sr_{0.17}Ga_{0.83}Mg_{0.17}O_{3-\delta}$;

LSM — lanthanum strontium manganite, $La_{0.85}Sr_{0.15}MnO_{3-\delta}$, $La_{0.6}Sr_{0.4}MnO_{3-\delta}$ (LSM64), $La_{0.8}Sr_{0.2}MnO_{3-\delta}$ (LSM82);

LSNF — lanthanum strontium nickelate ferrite, $La_{0.8}Sr_{0.2}Ni_{0.6}Fe_{0.4}O_{3-\delta}$;

OCV — open circuit voltage;

PMMA — poly(methyl methacrylate);

PVB — polyvinylbutyral;

μ-SOFC — microtubular solid oxide fuel cell;

SOFC — solid oxide fuel cell;

SSZ — scandia-stabilized zirconia, $Zr_{0.9}Sc_{0.1}O_{2-\delta}$;

YSZ — yttria-stabilized zirconia (8YSZ), $Zr_{0.9}Y_{0.1}O_{2-\delta}$ (10YSZ), $Zr_{0.97}Y_{0.03}O_{2-\delta}$ (3YSZ).

Designations:

a — radius of a particle;

C_d — particle concentration in a deposit;

C_s — particle concentration in a suspension;

d — particle size;

D — particle diffusion coefficient;

Du — Dukhin number;

e — charge of electron;

E — external electric field strength;

f — deposition efficiency factor;

h — deposit thickness;

I — deposition current;

K — reciprocal of the Debye length;

K^{-1} — Debye length;

k_B — Boltzmann constant;

L — distance between the electrodes;

m — deposited mass;

Pe — Peclet number;

S — electrode surface area;

T — absolute temperature;

U — potential difference between the electrodes during deposition;

V_p — electrophoretic velocity of particles in a liquid medium;

ε_0 — dielectric constant of vacuum;

ε_d — dielectric constant of the deposit;

ε_p — dielectric constant of particles;

ε_r — dielectric constant of the liquid medium;

ε_s — dielectric constant of the suspension;

ζ — electrokinetic potential, or ζ-potential;

η — dynamic viscosity of the liquid medium;

μ — electrophoretic mobility;

ρ — density of the deposit;

r_d — specific resistance of the deposit;

r_s — specific resistance of the suspension;

σ_s — surface conductivity of the particles;

σ_V — volume conductivity of the liquid medium;

τ — characteristic time of deposition.

1. Introduction

Over several last decades, the energy consumption all over the word has rapidly increased due to growth of population and increase in the living standards and also due to development of new energy intensive technologies. Currently more than 80% of energy is produced using direct combustion of fossil hydrocarbons (coal, oil, gas), which have relatively low efficiency factors (~20%–40%). This brings about severe environmental problems and, in addition, direct combustion will soon be restricted by depletion of available resources of non-renewable fuels.[1] Therefore, much attention is currently given to the development of renewable energy production technologies, the share of which in the global energy consumption is expected to be 23% by 2030 (in Russia, it will be 2%).[2] Since energy supply from renewable sources such as wind, solar radiation or tides is mainly discrete, much attention is paid to the development of hybrid systems based on fuel cells (FCs), the operation efficiency of which exceeds 80%.[3,4] Moreover, the operation of FCs is accompanied by the minimum release of pollutants and is free of noise or vibrations.[5]

Among the whole diversity of FCs, particular attention is drawn by solid oxide fuel cells (SOFCs), which have the highest efficiency among all FCs. The advantages of SOFCs include small size, the absence of structural parts hazardous to human health (such as harsh acid and alkali solutions used as electrolytes in alkaline and phosphoric acid FCs) and a wider range of compounds (compared with low-temperature FCs) applicable as primary fuels, such as hydrogen, hydrocarbons, synthesis gas or biofuel, requiring no expensive catalysts.[6,7]

The modern trends in the development of SOFCs are related to a decrease in the operating temperature (intermediate- and low-temperature SOFCs). This expands the scope of applicability of FCs and suppresses the degradation of output characteristics due to ageing and mutual diffusion of oxide layers.[8–11]

There are two main strategies for maintenance of an acceptable power density of SOFCs at a reduced operating temperature:

— reducing the contribution of ohmic resistance of the electrolyte to the total resistance of the cell, which can be attained by switching from cells with a bulk electrolyte to cells with thin-layer or thin-film electrolytes;[12,13]

— design of new functional materials for SOFCs with enhanced characteristics in intermediate- and low-temperature ranges such as electrolytes[11,14] possessing high oxygen ion and/or proton conductivity, active cathode[8,15,16] and anode materials[13,17,18] and interconnects.[19]

For reducing the cost of thin-film SOFCs, accessible and inexpensive methods for the formation of gas-tight solid electrolyte layers[20] on a porous substrate are required. The modern methods can be subdivided into chemical, electrochemical, physical, plasma and laser, colloid, ceramic and so on.[21,22] However, many of these methods either cannot form films of necessary thickness and quality or require the use of sophisticated and expensive equipment.[23–29] There exists a separate group of cost-effective and technologically flexible colloid techniques for the production of coatings, *e.g.*, dipping into a slurry or centrifugation. A drawback of these methods is the complicated control over the thickness of the resulting film and the necessity to repeat the dipping–drying cycles many times (in some cases, more

than 30 times to form a 1 μm thick film). Among the colloid methods for the film preparation, electrophoretic deposition (EPD) is distinguished by a high rate of coating formation (up to 1 μm per minute) and easy control of the coating thickness and microstructure by varying the applied potential and deposition time.[30–32] In addition, the method can be easily and quickly adjusted for deposition of layers of different composition on both conductive and non-conductive substrates of virtually any shape by minor changes in the cell configuration or positions of electrodes. Therefore, this method is promising for the manufacture of SOFCs of any design (planar, tubular and irregular-shaped) to deposit separate layers or to form a single cell as a whole.

Quite a number of studies have been devoted to the application of EPD for manufacturing SOFCs. For example, series of works address deposition of yttrium-stabilized zirconia-based electrolyte traditionally used in SOFCs;[33–37] fabrication of micro-tubular SOFCs by EPD;[38–41] formation of protective coatings for the SOFC interconnects.[42–47] The EPD method is suitable not only for the production of dense thin-film coatings, but also for the formation of porous electrodes on a supporting electrolyte [48–52] and ceramic bodies (bulk ceramic specimens).[39,53] The key advantages of electrophoretically deposited coatings include good adhesive properties and higher density compared with those of coatings obtained by dip coating or sputtering onto conductive cathode and non-conductive anode substrates.[54,55]

Successful electrophoretic deposition depends on the preparation of the conductive substrate, choice of materials, preparation of their stable suspensions and selection of deposition conditions to produce films of the desired thickness and microstructure. Electrophoretic deposition can be adjusted to all materials used for the manufacture of SOFCs that are supplied as finely dispersed powders.

Despite numerous studies addressing EPD, the key regularities related to its mechanisms and kinetics, the structure and density of the resulting coatings and the influences of the substrate shape and deposition conditions are not entirely clear. Therefore, in our opinion, for successful implementation of this method in SOFC technology, it is necessary to critically analyze the state of the art of experimental and theoretical works in this field.

The fundamental publications addressing the theory and practice of EPD are the reviews of Besra and Liu [31] and Corni *et al.*[32] They cover the depositon mechanisms, quantitative models and factors affecting the EPD. The authors noted the most popular applications of EPD such as the production of nanostructured functional materials,[30] formation of thin-film graded and layered coatings [31,32] and SOFC technology. Aziz and co-workers [38] presented a brief discussion of the details of EPD application in SOFC technology.

This review focuses particularly on the use of EPD for the creation of functional layers of SOFCs and identifies key challenges and approaches covered in the literature in the period from 2003 to 2018, with the most important earlier papers being mentioned if necessary. Data on the major theoretical approaches and results of studies of EPD are analyzed, EPD modelling and key characteristics and parameters are discussed. A possibly most comprehensive account of modern experimental results is given, in particular, studies of the authors of this review on the use of EPD for the manufacture of ceramic bodies, dense electrolyte layers for SOFCs of different composition, including porous multilayer electrodes, microtubular SOFCs and protective coatings on interconnects.

2. Theoretical approaches to the description of electrophoretic deposition. State of the art of the research

2.1. Colloidal systems and electrokinetic potential

This Section is concerned with the key trends of behaviour and characteristics of colloid suspensions, which give rise to a set of electrokinetic effects, in particular, electrophoretic deposition, which includes the motion of particles in a suspension and the proper formation of the deposit on an electrode substrate.

The surface of solid particles dispersed in a polar liquid medium has excess electric charge caused either by surface dissociation or by adsorption of ions.[56] Van der Biest and Vandeperre [57] considered four mechanisms for generation of the charge on the surface of a solid particle in a liquid:

— selective adsorption of ions from the liquid on the particle surface;

— dissociation of ions from the solid phase to the liquid;

— adsorption or orientation of bipolar molecules on the particle surface;

— electron transfer between solid and liquid phases due to different electron work functions.

A layer enriched with oppositely charged ions (counter-ions) appears in the solution near the particle surface and an electrical double layer (EDL) is thus formed. Under the action of electrostatic attraction forces, counter-ions tend to be located as close as possible to ions determining the particle surface charge (potential-determining ions).

The most general model for describing the EDL structure is the Gouy–Chapman–Stern model according to which a double layer is composed of dense (immobile) and diffuse parts.[58] This spatial charge separation gives rise to a number of characteristic properties of disperse systems, in particular, electrokinetic phenomena such as the relative displacement of phases under the action of electric field, *i.e.*, electrophoresis (particle motion in a medium) and electroosmosis (transfer of dispersion medium through a porous diaphragm) and generation of currents and potential difference upon the relative displacement of phases (sedimentation and flow currents and potentials).

The modern views on the electrical double layer are based on the Stern model with some modification of the Grahame model that refer to the inner structure of the dense part of the EDL.[59] The Grahame model distinguishes between specifically adsorbed ions, which often lose their solvation shell (or the shell is distorted) and are located more closely to the surface, and ions of the dense part with undistorted solvation shells located farther from the surface and connected to the surface only by electrostatic forces. The EDL dense layer comprises the inner and outer Helmholtz planes; the inner plane is formed by the centres of specifically adsorbed ions, while the outer plane is composed of dense part ions that have preserved their solvation shells.

The interaction between the solvent and the surface can also affect the structure of EDL in which the adsorbed solvent molecules have a predominant orientation.[60] The solvated ions are located in the outer Helmholtz plane and

are unable to penetrate into the solvation layer on the surface.

It was noted [61] that the electric field of the dense part of EDL (or the field of a molecular capacitor with averaged charge density) differs from the true field determined by the discrete charge nature. Nevertheless, the finite size of ions and the discrete nature of surface charges affect the potential distribution only in a very thin near-surface layer.[62] Therefore, in the case of large EDL thickness, these effects with a short radius of action are not manifested in electrophoresis. The discrete nature of charge becomes significant if the number of elementary charges on the particle surface is low and the electrolyte concentration is high. Thus, the classical electrokinetic theory is valid for certain values of parameters such as an electrolyte concentration range and the geometry and roughness of the charged surface.

A significant contribution to the development of electrochemical methods for studying the properties of EDL and the fundamental theory of the electrode reaction kinetics was made by Academician A.N.Frumkin and his school.[63] It is noteworthy [64] that, despite a certain 'communion of interests' of electrochemists and colloid chemists in the investigation of EDL, their approaches are different, because of the difference between investigation objects: an electrode in an electrolyte for electrochemistry and dispersed particles in the liquid medium for colloidal chemistry. The subjects of investigation are also different: electrochemistry studies the kinetics of electrode reactions, while colloidal chemistry deals with stability issues and electrokinetic phenomena.

The Derjaguin – Landau – Verwey – Overbeek (DLVO) theory describes the behaviour of a colloidal system in terms of attraction and repulsion energies between particles.[65, 66] When two particles approach each other, the diffuse parts of EDL overlap; as a result, like-charged particles are affected by a repulsion force, which consists of two components, namely, electrostatic and osmotic components. The electrostatic component is associated with electrostatic repulsion of like-charged particles (in particular, mobile ions) and their attraction to the overlapping diffuse layers. The osmotic component is associated with an increased concentration of mobile complex ions formed between the particles and the concomitant osmotic flow of the solvent towards this area.

Apart from the repulsion force, the particles are always subject to van der Waals attraction forces, with the interaction energy varying depending on the distance between the particles. The interaction energy between two particles plotted *versus* the distance between them is shown in Fig. 1. At large distances between the particles, the van der Waals attraction predominates. When particles approach each other, repulsion appears between the diffuse parts of EDLs described by the repulsion energy. This gives rise to a minimum total interaction energy, determining the aggregation of particles in a suspension: the particles temporarily and reversibly stick together. On further decrease in the distance between the particles, the repulsion energy increases and particles have to overcome an energy barrier to come closer to each other. At short distances between the particles, the interaction has a global minimum, which corresponds to irreversible coagulation.

An important characteristic of a colloidal system is the electrokinetic, or ζ-potential, which determines both the stability of suspensions and the electrophoretic mobility of

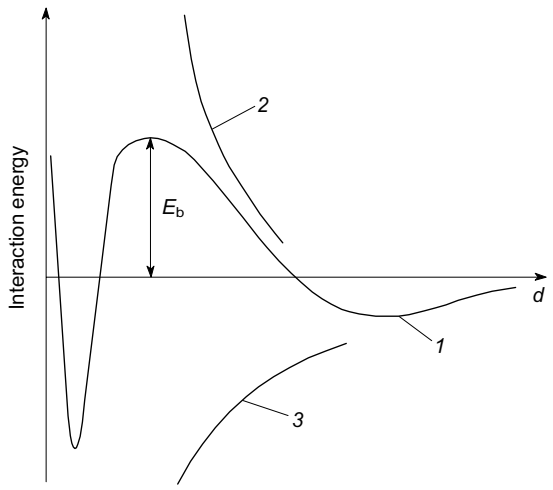


Figure 1. Interaction energy between two particles as a function of the distance between them according to the DLVO theory.[65, 66] E_b is the energy barrier; (*1*) total energy; (*2*) repulsion energy (V_r); (*3*) attraction energy (V_a); (*d*) distance between the particles.

particles, where the electrostatic repulsion of like-charged colloid particles dictates the height of the potential barrier separating the minima in the potential curve. This repulsion is caused by excess charge of the dense part of the EDL, which is equal to the surface charge minus the charge of all counter-ions located in the dense (immobile) EDL part. The higher this charge, the higher the ζ-potential.

The ζ-potential is defined as the potential in the diffuse part of the electrical double layer, in the slipping plane, where the liquid medium and the inner layer connected to the particle move relative to each other (Fig. 2).[58, 62]

The ζ-potential is affected by numerous external factors such as the temperature, concentration, pH and so on.[56, 67 – 79] The ζ-potential is usually found from the results of measurement of the steady-state velocity of the suspension particles under the action of applied electric field and particle electrophoretic mobility (μ) according to the formula

$$\mu = \frac{V_p}{E} \qquad (1)$$

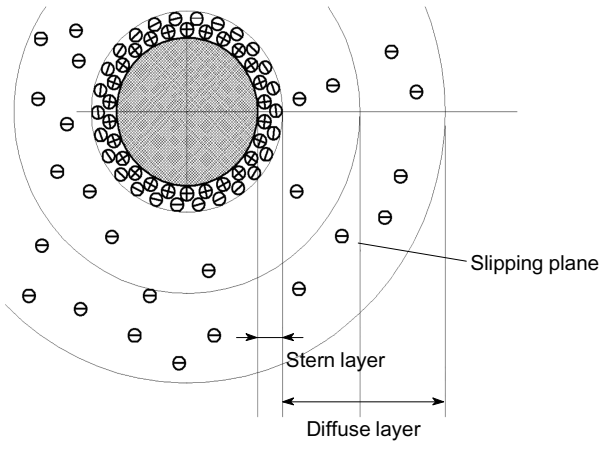


Figure 2. EDL structure.[58]

where V_p is the electrophoretic mobility of particles in the liquid medium, E is the external electric field strength.

The electrophoretic mobility can be found using the Henry equation [70]

$$\mu = \frac{2\,\varepsilon_r\varepsilon_0\zeta\,f(Ka)}{3\,\eta} \qquad (2)$$

Here ε_r is the dielectric constant of the liquid medium; ε_0 is the dielectric constant of vacuum; η is the dynamic viscosity of the liquid medium; $f(Ka)$ is the Henry coefficient determined by the particle radius (a) and the reciprocal of the Debye length (K)

$$K = \left[\left(e^2\sum_i n_i z_i^2\right)\left(\varepsilon_r\varepsilon_0 k_B T\right)^{-1}\right]^{1/2} \qquad (3)$$

where e is the electron charge; k_B is the Boltzmann constant; T is the absolute temperature; n_i is the concentration of z_i-charged ions.

In the general case at arbitrary Ka values, only numerical solution of Eqn (2) is possible.[71] In the case of thin EDL (Fig. 3 *a*) where $Ka \gg 1$, for large particles or a relatively high ionic strength of the solution, the electrophoretic mobility is defined by the Helmholtz – Smoluchowski equation

$$\mu = \frac{\varepsilon_r\varepsilon_0\zeta}{\eta} \qquad (4)$$

In the case of thick EDL (Fig. 3 *b*) where $Ka \to 0$, the electrophoretic mobility of small particles for low ionic strength of the solution is found from the Hückel equation

$$\mu = \frac{2\,\varepsilon_r\varepsilon_0\zeta}{3\,\eta} \qquad (5)$$

Currently, the ζ-potential is measured using electroacoustic analysis methods based on the action of an alternating electric field on the suspension. This action generates acoustic waves, the amplitude and phase of which are used to determine the ζ-potential.[72–74] Optical methods, *e.g.*, dynamic light scattering, are based on the change in the optical emission wavelength in a suspension on exposure to an external alternating electric field. The change in the emission wavelength is cased by electrophoretic motion of particles in the measuring cell owing to the Doppler effect; the measured electrophoretic mobility is proportional to the measured Doppler frequency shift $\mu \sim \Delta\omega$.[75,76] The characteristic ζ-potential that will ensure stability of the suspension, determined from the formula (6) is ~26 mV.

$$\zeta_c = \frac{k_B T}{e} \qquad (6)$$

This value is in good agreement with experiment data.[77,78] Note that the ζ-potential reflects the electrostatic repulsion forces between the particles; therefore, it cannot fully characterize the suspension stability, as apart from repulsion forces, long-range attraction forces also play a role.

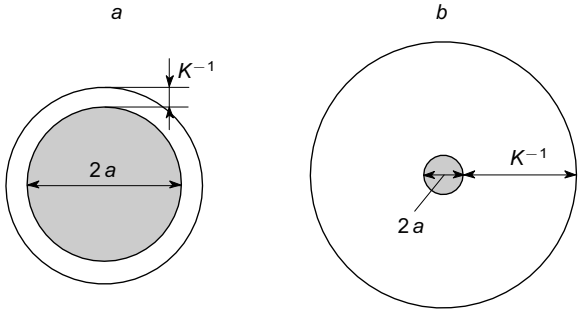


Figure 3. Thin (*a*) and thick (*b*) EDLs.[79]
2 *a* is the particle diameter; K^{-1} is the Debye length determining the EDL size.

2.2. Mechanisms of electrophoretic deposition

Electrophoresis of particles in a liquid medium near an electrode is transformed into deposition as a result of several physicochemical processes. The following deposition mechanisms have been established:[80] flocculation of particles, electrochemical coagulation, neutralization of the particle charge at the electrode and distortion of particle EDLs under the action of external electric field.

These mechanisms can be described in the following way:

— the flocculation takes place as particles are accumulated on the electrode and approach one another; as a result, they overcome the potential barrier for interparticle interaction generated by the external electric field.[81] This mechanism explains, in particular, deposition on a porous membrane placed between the electrodes and not connected to electrodes;

— the electrochemical coagulation of particles near the electrode occurs upon a change in the concentration of ions, which induces compression of EDLs, particle migration to one another, a decrease in the repulsion forces between the particles and subsequent coagulation. According to this mechanism,[82] it is assumed that particle accumulation and migration and diffusive redistribution of ions take place near the electrode for a certain period of time; as a result, the ionic strength of the electrolyte changes, which leads to decreasing height of the potential barrier for the interaction of particles in the suspension and, hence, causes formation of a deposited layer; probably, this mechanism is implemented in the presence of water, which induces electrode reactions and local pH changes;

— the mechanism of charge neutralization *via* direct charge transfer from particles to the electrode can account for the deposition of single particles or monolayers and for the initial stage of the EPD process, but it cannot be implemented if the thickness of the deposit further increases; on the basis of analysis of electron micrographs of electrophoretic coatings with noticeable porosity, it was assumed [83] that neutral aggregates are formed near the electrode and particles are mainly deposited on these aggregates;

— the motion of a particle affected by an external electric field is accompanied by a distortion of the EDL, namely, the EDL decreases under the action of the liquid medium, and the lyosphere around the particle becomes non-spherical, being extended towards the direction of motion; the motion of ions in the same direction as the motion of particles changes the concentrations of counterions near the electrode, which also decreases the EDL

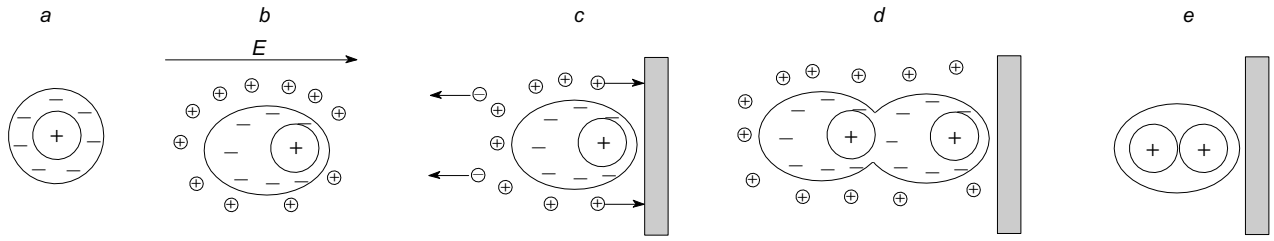


Figure 4. Diagram of the mechanism of cathode EPD associated with distortion of the EDL structure around the particles and their coagulation near the electrode.[80]
(*a*) Undistorted EDL; (*b*) EDL distortion along the external electric field during the particle motion; (*c*) change in the concentration of the counter-ions near the electrode; (*d*, *e*) particle coagulation; (*E*) external electric field strength.

thickness, reduces the height of the energy barrier of repulsion and causes coagulation of particles (Fig. 4).[80]

Currently, it is difficult to distinguish the predominant mechanism of electrophoretic deposition due to the absence of a universal theoretical description that would cover all processes arising during EPD in the suspension bulk and near the electrode with participation of particles, ions and flows of the liquid as well as interactions of particles and ions with the electrode and cell walls. However, development of studies along this line is necessary, because the existing array of experimental data does not always provide definite conclusions about the kinetics, transfer processes, deposition mechanism or the structure or density of the coatings formed under specified conditions. Therefore, a relevant task is further development of studies on the simulation of EPD using advanced numerical methods.

2.3. Kinetics and key parameters of electrophoretic deposition

The key parameters of EPD are the following: external electric field strength (E); electrophoretic mobility of particles in the suspension μ determined by the ζ-potential and viscosity of the suspension; concentration of the suspension (C_s); surface area of the electrodes (S); and dielectric constants of the suspension (ε_s) and the deposit (ε_d). Also, characteristics that vary with time (t), such as deposited mass (m), deposit density (ρ) and deposit thickness (h), are practically significant.

Currently, the kinetics of EPD process is commonly described in terms of generalization of the Hamaker equation reported by Sarkar and Nicholson[80] for the rate of growth of the deposited mass m per unit area s

$$\frac{dm}{dt} = f\mu sEC_s \tag{7}$$

where f is the deposition efficiency factor. For particles with a high ζ-potential, the efficiency factor f (fraction of particles deposited on the electrode out of the total number of particles that reach the electrode during deposition) is ~ 1.

In many studies dealing with EPD kinetics that are addressed in this Section, the deposition efficiency factor f is taken to be unity; furthermore this value is not considered to correlate with deposition conditions and properties of the suspension. However, one may assume a certain correlation between the factor f and both the suspension properties and electric field strength. This was indicated, in particular, by Hadraba *et al.*,[84] who presented dependences of the efficiency factor f and electrophoretic mobility of particles on the current during deposition. If the current is low (1 – 2 mA), the factor f is much less than unity. As the current increases, the factor f sharply grows to 0.9 – 1.0 and is then stabilized at $f \approx 1.0$ for currents of >10 mA. Meanwhile, with increasing current, the electrophoretic mobility smoothly decreases and reaches an asymptotic value when the current is >10 mA. These measurements were carried out for 18.7 cm^2 surface area of electrodes.

Ferrari and Moreno[85] considered the concentration of the suspension as the key parameter of EPD. If the concentration in the bulk of the suspension changes with increasing amount of the deposit, in the case of spatial uniformity of the suspension and other conditions being invariable (in particular, with invariable particle mobility and constant electric field strength E), the time dependence of the mass $m(t)$ deposited on an electrode with the surface area S is described by the following equation:

$$m(t) = m_0\left[1 - \exp\left(\frac{t}{\tau}\right)\right] \tag{8}$$

where m_0 is the initial mass of the particles in the suspension of volume V; τ is the characteristic deposition time

$$\tau = \frac{V}{f\mu SE} \tag{9}$$

Biesheuvel and Verweij[86] made an important addition to the equation of deposition kinetics based on the mass balance between the suspension and the deposit. The velocity of movement of the deposit/suspension interface is determined by the following expression:

$$\frac{dh}{dt} = -V_p\frac{C_s}{C_d - C_s} \tag{10}$$

where h is the thickness of the deposit layer; V_p is the electrophoretic velocity of particles in the suspension; C_s is the particle concentration in the suspension; C_d is the particle concentration in the deposit.

The rate of mass growth during deposition is given by

$$\frac{dm}{dt} \approx \frac{C_s}{C_d - C_s} \tag{11}$$

It can be seen that a sharp increase in the deposited mass will take place when the concentration of the suspension becomes equal to the particle concentration in the deposit.

The variation of the deposited mass with time is different for constant-current and constant-voltage EPD processes, as follows from the basic relation (7), because the deposition rate is related to the electric field strength. In the case of constant-voltage EPD, the field strength in the suspension may considerably decrease due to a decrease in the current caused by increasing resistance of the deposit, whereas in the constant-current deposition, the electric field strength depends only on the current and can vary only upon variation of the suspension resistance.[80]

The electric field strength in the suspension for constant-voltage deposition is given by

$$E = \frac{U}{L + R'm} \tag{12}$$

where U is the potential difference between electrodes of surface area S located at distance L; the parameter R' is defined by the expression

$$R' = \frac{(r_s/r_d) - 1}{\rho S} \tag{13}$$

where r_s is the specific resistance of the suspension; r_d is the specific resistance of the deposit; ρ is the deposit density.

During constant-voltage deposition, the rate of increase in the deposited mass considerably declines with time, as compared with the constant-current deposition.[80]

For the choice of dispersion medium, an important factor is stability of the deposition process.[85, 87] For the formation of a smooth homogeneous coating, it is necessary that the dielectric constant of the suspension be higher than the dielectric constant of the deposit. This conclusion follows from the expression for the field strength E in the suspension [85]

$$E = U\left[L + h\left(\frac{\varepsilon_s}{\varepsilon_d} - 1\right)\right]^{-1} \tag{14}$$

For $\varepsilon_s > \varepsilon_d$, an occasional local increase in the deposit thickness would lead to a decrease in the electric field strength in this area, which would reduce the local deposition rate and mitigate the irregularity. In the opposite case, the deposition would become unstable, since at $\varepsilon_s < \varepsilon_d$ the arising irregularity of the deposit would increase, as particles would mainly stick to the already formed bulges of the deposit. The effective dielectric constant of the suspension depends on the volumetric concentration of particles; for a dilute suspension and a relatively dense deposit, it can be assumed that $\varepsilon_d = \varepsilon_p$; $\varepsilon_s = \varepsilon_r$, where ε_p is the particle dielectric constant and ε_r is the dielectric constant of the liquid dispersion medium.

The theoretical models considered in some studies include the change in the cell resistivity and, hence, field strength in the liquid medium. Ferrari *et al.*[88] analyzed the change in the deposition kinetics following increase in the suspension resistivity with time caused by the decrease in the particle concentration. The key assumption used by the authors is the linear dependence of the suspension resistivity on the particle concentration during the constant-current deposition. In this case, the increase in the deposited mass deviates from the kinetics determined by the exponential law and reaches saturation according to formula (8).

This model predicts an S-shaped curve for the deposited mass with time. In the initial period, the rate of growth of the deposited mass increases and then decreases. The authors [88] showed that their model is consistent with the classical model for the initial period of deposition; however, in the case of a long-term process, substantial deviations arise. It was noted that this model neglects the variation of the electrophoretic mobility and some other parameters with time.

Van der Biest *et al.*[89] presented the functional dependences of the total resistance of the EPD cell, which included resistances of the suspension and the deposit, found using an equivalent electrical circuit. The authors suggested that the resistance of the suspension is due to migration of ions and charged particles and the conductivity of the deposit is due to the conductivity of particles and ionic charge transfer in the solvation shells around the particles. The conductivity generated by ions of the solvation shells in the deposit ($\sigma_{i\,dep}$) is related to the conductivity generated by ions in the suspension ($\sigma_{i\,sus}$) with a definite constant factor (λ) in the following way:

$$\sigma_{i\,dep} = \lambda\sigma_{i\,sus}, \quad \lambda \geqslant 1 \tag{15}$$

According to this model, the resistance of a deposit of area S and thickness h_1 caused by the intrinsic conductivity of particles $\sigma_{p\,dep}$, for the volume packing fraction p, can be written as follows:

$$R_{p\,dep} = \frac{h_1}{\sigma_{p\,dep}\,pS} \tag{16}$$

while resistance of the deposit related to the ionic current in the solvation shells around the particles is

$$R_{i\,dep} = \frac{h_1}{\sigma_{i\,dep}\,(1-p)S} \tag{17}$$

The resistance of the suspension is determined by the difference $L - h_1$ (here L is the distance between the electrodes). Thus, the resistance caused by suspension ions is equal to

$$R_{i\,sus} = \frac{L - h_1}{\sigma_{i\,sus}\,S} \tag{18}$$

The resistance caused by charge transfer of particles of mobility μ in a suspension with concentration C_s is

$$R_{p\,sus} = \frac{L - h_1}{\mu S C_s\,Q_{ef}} \tag{19}$$

where Q_{ef} is the efficient charge density on the particles.

The total direct current resistance of the deposition cell can be calculated as

$$R_{tot} = \frac{R_{p\,sus}R_{i\,sus}}{R_{p\,sus} + R_{p\,dep}} + \frac{R_{i\,dep}R_{i\,sus}}{R_{p,dep} + R_{i\,dep}} \tag{20}$$

Using these relation, it is possible to derive the functional relationship between the field strength in the suspension and the current thickness of the deposit h_1 and to obtain a modified expression for the mass growth rate. However, it is noteworthy that the model is phenomenological, and the suspension conductivity and particle mobi-

lity are assumed to be invariable and certain assumptions are made concerning the deposit resistance. For application of this model, these assumptions should be fulfilled and the conductivity values, which can change considerably under particular experimental conditions and during the EPD process, should be known.

Stappers *et al.*[90] reported experimental results that showed the necessity of further refinement of theoretical models for increase in the cell resistance during EPD. The authors studied the deposition of a suspension of α-Al_2O_3 particles in ethanol for average particle sizes of 270, 370, 770 and 1890 nm and concentration changing from 50 to 100 g litre^{-1}. The suspensions had high ζ-potentials (73 – 92 mV) as a result of addition of HNO_3 and deionized water. The deposition current, cell impedance, decrease in the potential in the suspension bulk and in the deposit were measured. It was shown that during deposition, the electric field strength in the suspension bulk decreases with time, with the rate of field strength decrease being dependent on the suspension conductivity: at high conductivity (67 μS cm^{-1}), the field strength sharply decreased in the beginning of deposition, while at low conductivity (3.2 μS cm^{-1}), the decrease in the field strength was linear and much less pronounced. The time dependences of the field strength were measured for suspensions with different particle sizes. The field strength changed much more rapidly in suspensions of larger particles than in smaller-particle suspensions. Direct measurement of the potential drop across the deposit showed a significant dependence of the potential on the applied voltage, conductivity and suspension concentration, which also influenced the full cell impedance.

The effects of the suspension concentration and the voltage on the increase in the cell resistance may probably be interpreted considering the following kinetic model of EPD: an increase in the cell voltage induces more intense deposition and depletion of the suspension in the particles, which causes a faster increase in the resistances of the deposit and the suspension. The effect of the suspension concentration can also be explained at a qualitative level: an increase in the concentration also intensifies the deposition according to Eqn (10). An interesting result was obtained in a study of the effect of particle size on the cell resistance: since in the classical theory of electrophoresis, the mobility μ does not depend on the particle size, there is no direct effect of the particle size on the quantities appearing in Eqn (7).

Stappers *et al.*[90] established the effect of the particle size on the increase in the cell resistance during deposition at a constant applied voltage of 200 V. It was also found that after the EPD voltage is switched off, the resistance decreased, which may indicate that the cell resistance is associated with not only growth of the deposit, but also processes taking place directly during the EPD. The authors reapplied the voltage to the cell containing the already formed deposit, with the suspension being replaced by the liquid obtained after centrifugation (supernatant). They found that immediately after the voltage application, the cell resistance rapidly returned to the value that was established before the voltage was switched off and then increased, while no increase in deposit thickness or depletion of the suspension in the particles took place. The results attest to a significant role of ion migration and ion interaction with the deposit layer, *i.e.*, electrochemical reactions accompanied by pH change occur near the electrode during the EPD; the reactions are terminated when the external voltage applied to the cell is switched off. These results suggest that the current through the cell is mainly caused by the ionic composition of the liquid medium, which is, in turn, determined by the properties of dispersed particles. Moreover, a certain 'memory effect' is possible where the properties of a colloidal system depend not only on its current state, but also on the prehistory.

Subsequently, the same authors[91] reported the results of cell impedance measurements for the EPD process during and after the deposition. The measurements confirmed the increase in the impedance after completion of EPD with the use of supernatant obtained by centrifugation of the initial suspension. In our opinion, the results concerning the increase in the cell resistance and effect of the particle size on the process kinetics are of interest as regards the necessity of refinement and further development of the theoretical models describing the EPD under various conditions. The models should include the contribution of non-stationary transport processes, change in the resistance of suspension and deposit layers during the deposition, ion migration, system prehistory and nonlinear effects of electrophoresis.

It should be noted that, despite the relative simplicity of phenomenological models, their practical application is hampered by the absence of correlations and models for macroscopic quantities such as resistances of the deposit and the suspension, which determine the deposition regime. As a matter of fact, these models can be applied only using experimental results obtained under definite conditions. Upon replacement of the colloidal system, it will be impossible to predict parameters of the coating and deposition regimes. This attests to necessity of further development of modelling approaches both at the macro level for a continuous medium with description of the transport processes and at the micro level with explicit description of particle movement and interactions.

The simulation of spatially discontinuous and non-stationary transport processes was reported by Pascall *et al.*[92] The authors considered the effect of spatially discontinuous field strength distribution near the electrode edge on the thickness of the obtained coating. The problem of simulating the deposition process and determining the deposit shape as a function of time is solved in a 2D space by formulation of transfer equations in the computational domain provided that the suspension is electrically neutral. A number of assumptions was introduced: first, it was assumed that the particles move through a unperturbed liquid medium; the electric field distribution in the medium is not affected by the particles or the deposit; no ion flux, charge accumulation on the electrodes or their polarization are involved. The particles move under the action of external electric field in the presence of diffusion, and the interparticle interactions are neglected (except for the constraint on the limiting particle packing density in the deposit and influence of the particle concentration on the suspension viscosity). The particles are considered to be identical; gravitational sedimentation is not considered either. The electrical potential of the suspension (φ) satisfies the Laplace equation:

$$\nabla^2\varphi = 0 \qquad (21)$$

The electric field with the strength $E = -\nabla\varphi$ is related to the total particle flux (J) in the suspension, which results from the concentration gradient (C_s) and electric field strength (E)

$$J = -D\nabla C_s + \mu E C_s \quad (22)$$

where D is the particle diffusion coefficient.

Due to the conservation law, the volume fraction of particles in the medium, related to the concentration, satisfies the equation of continuity, which has a quantity determined (in the case of thick EDL) by Hückel relation (5) containing the ζ-potential and viscosity. The authors took into account the increase in the viscosity and decrease in the mobility of particles with increasing concentration of the suspension and the maximum possible packing density of particles on the electrode, that is, the limiting concentration. The obtained numerical solution demonstrated the presence of a sharp peak of the electric field strength near the electrode edge, which causes a local increase in the particle flux and thickening of the coating at the electrode edges. In the initial period, deposition mainly takes place at the electrode edges; as the deposited amount increases, the deposit becomes thicker at the electrode centre, that is, the irregular height of the deposit is smoothed down. The authors intend to complicate the model in the future by including the voltage drop across the deposit and to extend the applicability of the model for various experimental conditions.

2.4. Direct numerical simulation of the particle movement and mesoscopic models

A recent trend in the simulation of electrophoresis and deposition of particles involves direct calculation of particle dynamics, with allowance for interparticle interactions and particle interactions with the electrode, which provides conclusions about the deposit structure and its dependence on the deposition conditions. This is done using both direct numerical simulation of the particle motion and mesoscopic modelling of the electrophoretic motion and deposition, which switch from a continuum model description of EPD to a description based on discrete models using high-performance computing clusters.

Park and Saintillan [93] simulated the evolution of a system of N identical suspended particles with sizes $Lx \times Ly \times Lz$ located in a constant electric field acting along the Z direction. Pairwise interactions of the particles in the suspension were taken into account. The particle migration under the action of an external electric field was described by the Langevin equation, which contains a contribution of Brownian random forces to the particle displacement.[94] The type of interaction between a particle and the electrode onto which the deposition takes place is specified as dipole, van der Waals or steric interaction. The direct numerical simulation of the movement of 4000 non-conducting charged particles was performed in a rectangular computational domain at an external electric field strengths of 20, 40 and 60 V cm^{-1}. The initial configuration was specified randomly. A series of calculations afforded the spatial size distribution of the particles deposited on the electrode. It was found that with increasing electric field strength, the arrangement of particles in the deposit becomes less ordered. A regular arrangement of crystalline particles was obtained for low field strengths. As the field strength increases, the particle arrangement becomes less regular, and the coating acquires a polycrystalline structure with numerous defects. The authors attributed this trend to the fact that with increasing field strength, the role of diffusion diminishes and the particle redistribution time near the electrode is reduced, which prevents the formation of a regular arrangement of particles.

Some recent studies have developed EPD simulation at the mesoscopic level, which is intermediate between the Eulerian representation of the distribution fields of macroscopic values (such as electric potential, concentration, flow density) and the Lagrangian representation of the movement of single particles using, *e.g.*, molecular dynamics methods.

Giera *et al.*[95] presented a mesoscopic model of electrophoresis, which involves modelling of motion for a definite number of particles suspended in the computational domain of the liquid medium. The particle motion was described by Newtonian equations of motion where the total force acting on each particle includes the following components:

— resistance from the liquid medium and stochastic Brownian forces;

— the interparticle interaction force determined by the DLVO theory with attraction and repulsion potentials depending on the characteristic particle radius a, the interparticle interaction constant and the Debye length;

— the force acting from the external electric field, which is proportional to the field strength and effective charge on the particle.

The motion of 1000 particles was modelled in the absence of an external electric field with only the Brownian motion and in the presence of uniform external fields of different strength. The model was tested by calculating the diffusion coefficients of particles. The simulation results were used to determine the average particle velocity V_p along the field, which was proportional to the field strength

$$V_p \sim \frac{E}{\eta} \quad (23)$$

which corresponds to Henry equation (2). The results confirmed good performance of the numerical model in view of its compliance with known relations of the theory of electrophoresis in the suspension bulk on explosure to a uniform external electric field without non-stationary deposition or deposit growth. The authors assumed that the scope of applicability of the model could be expanded by taking into account the interaction between the suspension and the electrode, the effect of deposit morphology, gradient and time variation of macroscopic characteristics.

Giera *et al.*[96] reported further development of the mesoscopic model by considering the electrophoretic motion of particles in the suspension bulk, interparticle interactions and particle interactions with the electrode during deposition, which allowed them to apply this model to description of the deposit structure. The model is based on calculation of the dynamics of equal-sized particles in a uniform field being deposited on a planar electrode, which was modelled by a grid of uncharged particles. The pairwise interaction between particles is described by a DLVO theory potential, with the pairwise interaction potential being defined in terms of the Debye length K^{-1}, particle radius a and the ζ-potential. The authors presented the results of a series of calculations of the particle packing density in the deposit depending on the Debye length and

the electric field strength, which corresponds to variation of the Peclet dimensionless number

$$\mathrm{Pe} = \frac{V_p a}{D} \quad (24)$$

The deposition at a constant strength of external electric field was considered without taking account of the decrease in the concentration of the suspension upon deposition. According to the obtained results,[96] the deposit thickness linearly increases with time, which demonstrates the agreement of the model in describing the deposited mass kinetics with Hamaker equation (7) for the early period of deposition. The deposition from a suspension with a smaller K^{-1} results in a higher deposit density owing to a lower interparticle repulsion force. The authors present important results concerning the influence of the external electric field strength on the deposit structure that could not be obtained using the above phenomenological models. At high Peclet numbers, *i.e.*, high external electric field strength, the influence of the Debye length on the deposit density is less pronounced. Therefore, it was concluded that the structure of the primary monolayer formed on the electrode surface influences the growth and structure of the deposit. There is a transition between the initial, highly ordered deposited layer and disordered layers, which accounts for the density gradient across the deposit. The deposition conditions significantly affect the deposit structure. The authors intend to supplement the model by taking into account the change in the deposit resistance with time and the stepwise change of the electric field potential, which would enable considering the change in the deposition kinetics. It is also possible to consider polydisperse systems, polarizability of EDL, modelling of non-uniform particles (Janus particles) and particles coated by adsorbed polymer layer.

An attempt to considerably expand the range of physicochemical processes that accompany electrophoresis in the suspension bulk by considering the concerted motion of particles and change in the EDL, ion distribution and liquid flow was undertaken by Bartuschata and Rude.[97] The publication presents the results of direct numerical simulation of the electrophoretic motion of particles in the liquid medium using parallel algorithms to take into account various physical properties:

— the motion of solid charged particles in the liquid medium was described by Newtonian equations of motion, which include the forces acting on particles, in particular, from the external electric field;

— the motion of the liquid medium was described by the Navier – Stokes equation for an incompressible liquid;

— the motion of ions in the liquid medium under the action of electric field and the diffusion redistribution of ions were described by the Poisson – Boltzmann equation.

The authors used the fixed Eulerian grid to describe the velocity distribution of ions; for particle motion, the Lagrangian representation was used with calculation of coordinate and velocity changes for each particle. The lattice Boltzmann method (LBM) was applied to simulate the interaction between the particles and the liquid medium.

The following problems were solved:

— the problem of electrophoretic motion of a single particle in a microchannel taking into account the interaction with ions distributed in the liquid;

— the problem of potential distribution in the EDL around a spherical particle with uniform surface charge distribution; the results are compared with the results of analytical solution of the problem;

— the problem was scaled to pass to simulation of motion of more than 4×10^6 spherical particles using a multicore computing system.

The authors intend to simulate the motion of non-spherical particles, supplement the existing model with a pairwise interparticle interactions and consider non-stationary processes. This task requires high computational resources; therefore, further complication of the numerical model and transition to simulation of the effects near the electrode with allowance for the non-stationary processes would require a considerable increase in the computational power.

2.5. Deposition within porous structures

It is of interest to consider the effects related to the EPD within porous structures. This process takes place, for example, in the surface layer of a porous electrode being coated by a thin-film electrolyte layer and during the fabrication of multilayer electrolyte and functionally graded porous electrodes as polymeric porous templates to be impregnated with ceramic particles.[98] The latter experiments stimulated the development of a new model[99] for describing the effects taking place inside the narrow channels of the polymeric template upon the insertion of suspended particles induced by an external electric field.

Mayén-Mondragón *et al.*[99] considered two models. The first one describes the distortion of long-range electric repulsion forces between two particles in a narrow cylindrical channel (capillary). The authors used the finite element method and the commercial FlexPDE software.[100] The repulsion forces between the particles were calculated by solution of the problem of electric potential distribution with overlapped EDLs of particles; the distribution is described by the Poisson – Boltzmann equation in the given computational domain at specified boundary conditions and symmetry conditions. It is assumed that the field is symmetric relative to the capillary axis and does not extend beyond the capillary. The characteristic parameter of the problem is the reciprocal of the Debye length.

The second model describes the electroosmotic flow in the channels of the polymeric template. The authors consider a rectangular channel filled with an electrolyte solution; a potential difference is applied to the edges of the channel and gives rise to the electroosmotic flow of electrolyte in the solution. A stationary process can be described by simultaneous solution of the Poisson, Nernst – Planck and Navier – Stokes equations. The equations contain the concentrations of cations and anions in the electrolyte solution, the electric potential and the velocity of the liquid in the channel.

The results of calculations according to the first model showed that the interaction (repulsion) force significantly decreases when the particle EDLs and the capillary walls overlap if the potentials have the same sign. This effect is significant when the capillary width is of the same order as the particle diameter: in this case, suspension instability, clogging of the channels and termination of the particle insertion are possible. The calculation according to the second model gave the velocity distribution for the electroosmotic flow for various channel wall potentials. The electroosmotic flow can promote the insertion of particles

if the directions of the flow and electrophoretic motion of particles coincide. The particle penetration depth can be controlled by changing the particle size and concentration and also parameters of the liquid, electric field strength and time.

2.6. Particle polarization upon deposition

The EPD of conducting particles gives rise to a number of nonlinear electrokinetic effects caused by polarization of these particles.[62, 101, 102] When the EPD technology is used for the formation of the functional layers for SOFCs, these effects play a secondary role, in our opinion, because this is normally done with nano- and microparticles of ~ 1 μm size in relatively weak fields. Nevertheless, these effects can be manifested in the region of a significant electric field gradient at the substrate edge and also in the case of EPD of micro-sized powders or significant electrochemical coagulation of nanoparticles during EPD.

The classical theory of electrophoresis implies a constant surface charge of the particles, which are assumed to be non-conductive, and the electrophoretic mobility does not depend on the external field strength

$$\mu = \frac{V_p}{E} \sim \frac{\zeta}{\eta} \tag{25}$$

The settled particle velocity V_p depends linearly on the electric field strength. When particles are polarizable, the surface charge and ζ-potential are no longer constant, but start to depend on the external electric field strength. This gives rise to a number of nonlinear electrokinetic phenomena such as dielectrophoresis or nonlinear electrophoresis. Dielectrophoresis is the movement of particles in a non-uniform electric field caused by the interaction between the induced dipole moment of particles and the external electric field. The force acting on a particle depends on the particle size, the electric field gradient and the vector of the induced dipole moment determined by the surface conductivity and polarization of the particle and dispersion medium. The particle velocity during dielectrophoresis is given by

$$V_p \sim \frac{a^2 \nabla E^2}{\eta} \tag{26}$$

where a is the particle radius and η is the dynamic viscosity of the dispersion medium. Dielectrophoresis results in separation of a polydisperse suspension due to the dependence of electrophoretic mobility on the particle size.

The electrophoretic mobility depends on E, which is due to charge redistribution in the diffuse part of the particle EDL induced by the external electric field. This changes the surface potential of the particle. The electrophoretic mobility is expressed, in this case, as a power series in terms of the field strength

$$\mu = \frac{V_p}{E} \sim \frac{\varepsilon_r}{\eta}\left(\zeta + \alpha \frac{E^2 a^2}{\eta} + \ldots\right) \tag{27}$$

where α is a constant coefficient.

Nonlinear effects arise in the case of large surface charge of particles. As a result of these effects, the concentration of counter-ions in the liquid medium near the surface changes in such a way that surface conductivity appears in the EDL region; in this case, the relations of the classical linear electrophoresis are inapplicable. The particles acquire a dipole moment, giving rise to electroosmotic flow near them. The nonlinear electrokinetic phenomena and the surface conductivity are significant when the ζ-potential is relatively high (> 50 mV).[103] The effect of surface conductivity is determined by the dimensionless Dukhin number

$$\mathrm{Du} = \frac{\sigma_s}{\sigma_v a} \tag{28}$$

where σ_s is the surface conductivity of the particle, σ_v is the volume conductivity of the liquid medium. Schnitzer and Yariv[104] analyzed the results of earlier studies carried out for strong fields. An expression for electrophoresis rate for the case of small Dukhin numbers was derived.

This Section summarizes the theoretical approaches to the description of EPD and highlights the key factors based on models of different spatial scales, particularly, phenomenological kinetic models; descriptions of transport processes in a continuum medium using systems of partial differential equations; and discrete models with direct calculation of particle dynamics. Specific features of the EPD within porous structures, polarization effects involved in the EPD of conductive particles and nonlinear effects of EPD, which are significant in the case of high ζ-potentials and strong fields, were identified. It seems relevant to continue the development of integrated physicochemical modelling of processes involved in EPD. This will expand the scope of applicability of theoretical models in real experiments where an important role is played by non-stationary effects and spatial variation of both the macroscopic parameters (resistances of the suspension layer and deposited layer; suspension concentration; field strength, concentration of ions; ζ-potential) and the micro-level processes (EDL changes, particle interactions with one another and with the deposit).

3. Preparatory stages for the conduction of electrophoretic deposition

3.1. Electrophoretic deposition

The schematic diagram of an EPD setup consists of a battery, a suspension vessel, a conductive substrate, which often acts as the working electrode, and a counter electrode (Fig. 5).[35, 105] Electrophoresis is carried out for suspensions of ceramic particles, which acquire a certain effective charge in suspensions. This is the key difference between the EPD and the electrolytic deposition, or electrodeposition, in which solutions of salts are used, *i.e.*, the movement of ions is considered.[106] The electrophoretic and electrolytic deposition techniques give $1-10^4$ and $10^{-3}-1$ mμ-thick coatings, respectively. The electrolytic deposition is also used in the SOFC technology, *e.g.*, to form the protective coatings for interconnect application.[107, 108]

In the EPD setups, the electrodes are usually mounted vertically and are parallel to each other; the charged ceramic particles of the suspension move horizontally under the action of the applied external field. The electrode to which the particles move is determined by the sign of the ζ-potential of the suspension: in the case of anodic EPD, negatively charged particles form a layer on the positively charged electrode, while in the case of cathodic EPD, positively charged particles are deposited from the suspension onto the negatively charged electrode. Due to the limited choice

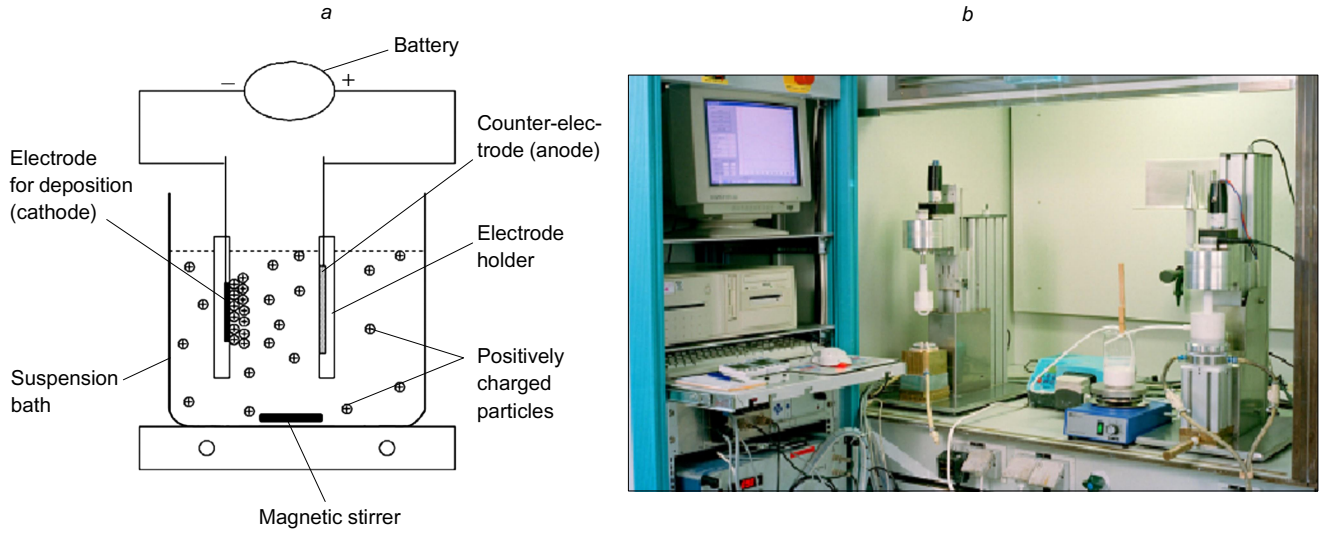


Figure 5. Diagram of the setup for cathodic EPD with vertical electrodes (*a*)[35] and photograph of the laboratory setup for this process (*b*).[105]

of materials and substrates for anodic deposition, the cathodic EPD is used most widely in SOFC technology.[109, 110]

Depending on the specified task, the electrodes can also be located horizontally. For the deposition from a non-aqueous suspension of commercial ceria powder with a very broad particle size distribution

d_n †	d_{10}	d_{50}	d_{90}	d_{100}
Particle size /μm	0.8	6.3	17.1	30

it was demonstrated that a horizontal setup in which the charged particles move upwards (oppositely to gravity, Fig. 6) resulted in more uniform coatings than the deposition in a vertical setup.[111] However for a deposition time of 600 s and suspension concentration of 10 mass %, the mass of the coatings deposited in the vertical setup (0.20 g cm^{-2}) was more than twice greater than that obtained in the horizontal setup (0.07 g cm^{-2}).

The horizontal arrangement of the electrodes is more advantageous for automation of the deposition process for multilayer coatings. The process in an automated horizontal EPD setup gave[112] coatings of tetragonal 3YSZ (5.22 mass % Y_2O_3) and cubic 8YSZ ($Zr_{0.92}Y_{0.08}O_{2-\delta}$) zircona composed of 5, 31 and 75 alternating layers with uniform thickness of 125, 55 and 20 μm, respectively. In a vertical unit, it was impossible to achieve equally thick layers, with the layer thickness obtained with the same deposition time (30 min) varying from 1216 to 142 μm (for 3YSZ) and from 383 to 139 μm (for 8YSZ).[113, 114] A number of publications describe the electrophoretic deposition of functional layers for tubular SOFCs, including microtubular SOFCs (μ-SOFCs) and other complex structures.[53, 115 – 118] An example of the setup for manufacturing microtubular SOFCs by EPD is shown in Fig. 7.

† The boundary particle sizes (diameters) below which are 10%, 50%, 90% and 100% of particles are designated by d_{10}, d_{50}, d_{90} and d_{100}.

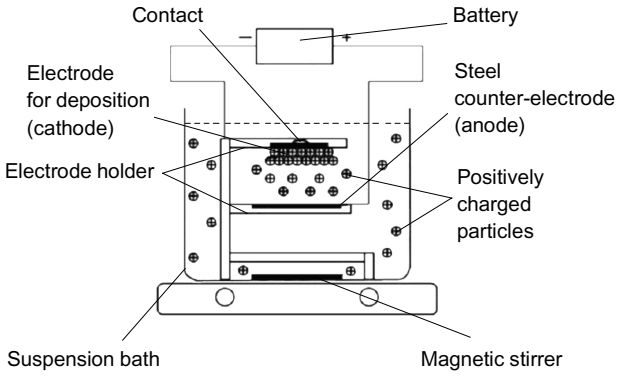


Figure 6. Diagram of the setup for cathodic EPD with horizontal electrodes.[111]

The electric field that initiates the migration of charged particles in the suspension and their deposition onto a conductive substrate can be direct current (classical EPD), pulsed direct current and symmetrical and asymmetrical alternating current fields. The specific features of these processes have been discussed in reviews.[120 – 123] The use of pulsed direct and alternating current fields is beneficial for EPD from aqueous solutions, since this suppresses the electrolysis of water.[123, 124] Recently, the pulsed method was also applied to deposition of the YSZ films from non-aqueous suspensions.[125]

Among the factors that have a key influence on the EPD yield, mention should be made of those associated with the preparation of suspensions (aggregate and sedimentation stability) and those related to the deposition process (choice of the substrate, electrical process parameters, deposition time). Another important factor is the introduction of modifying additives to suppress cracking of the coatings during drying. All of the mentioned factors and their influence on the preparation of suspensions based on SOFC materials and on the deposition of functional layers are considered below.

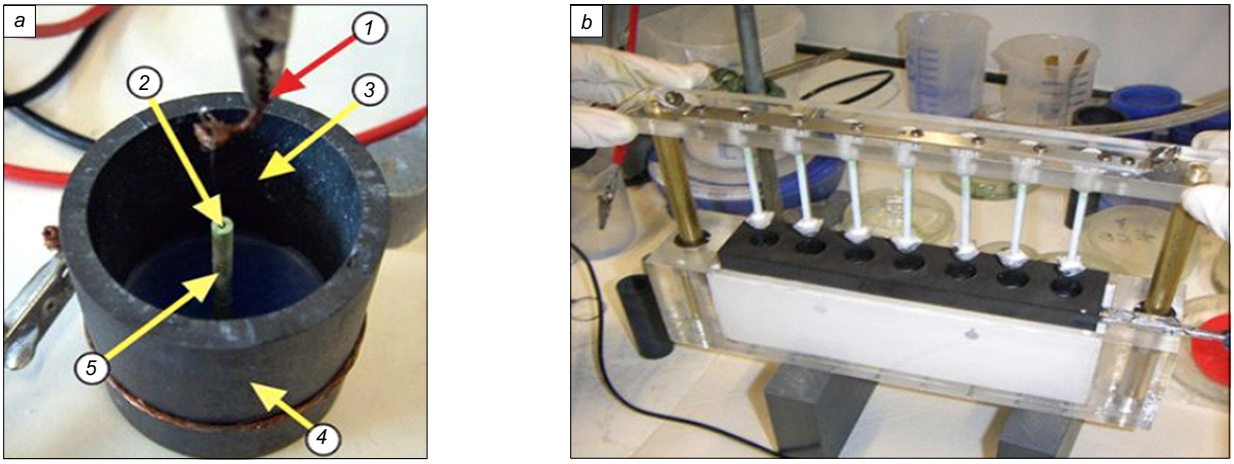


Figure 7. Photograph of a single cell (*a*) and the setup for the EPD of a thin film of zirconia-based solid electrolyte on a porous NiO – YSZ anode for microtubular SOFCs (*b*).[119]
(*a*) (*1*) Wire anode, (*2*) inner cavity of the microtube, (*3*) space occupied by the suspension, (*4*) cylindrical cathode, (*5*) porous NiO – YSZ microtube; (*b*) a set of cells for group EPD technology.

3.2. Preparation of stable suspensions based on SOFC functional layer materials for EPD

Preparation of suspensions is the key process determining the success of EPD and reproducibility of developed technology. The major difference of the EPD from other colloid techniques is the fact that with suspension concentrations of 1 vol.% – 2 vol.%, the green densities ‡ of deposited coatings reach 40% – 60%.[57] The formation of a dense and uniform coating with good adhesion to the substrate is possible only when suspensions used for EPD are stable against sedimentation and/or aggregation.[31, 32, 126, 127] The kinetic (sedimentation) stability, that is, the ability of a system to retain the uniform distribution of particles throughout the bulk of the dispersion phase, is largely determined by the particle size. When the size is < 1 μm, the particles can occur in the suspended state for long time owing to the Brownian motion, whereas suspensions of micro-sized ($\geqslant 1$ μm) powders need to be continuously stirred. However, it is noteworthy that suspensions of nano-sized powders may have low aggregate stability, that is, stability against coalescence of particles in a suspension. According to the DLVO theory, the aggregate stability is due to electrostatic repulsion forces between particles that exceed the van der Waals attraction forces. A key quantitative parameter of the suspension characterizing the repulsion forces is the ζ-potential. To ensure the suspension stability, it is necessary to maintain the ζ-potential in the 20 – 30 mV range.[31, 32, 38] At higher ζ-potentials, the repulsion forces between particles prevent aggregation.

3.2.1. Choice of the dispersion medium

The stability of suspensions considerably depends on the dispersion medium and on the ratio of initial components (amounts of the powder, solvent, pH-control agents, dispersing additives, deflocculants, polymer binders and so on). During dispersion, it is necessary to break bonds between the particles of the dry powder material. To this end, it is necessary to choose a medium that readily solvates the particle surface. Water is most preferable for EPD, since lower voltage is required in this case, which is beneficial for both economical and environmental reasons. However, the use of aqueous suspensions brings about a number of problems. The first one is occurrence of electrochemical reactions on electrodes, which considerably affect the efficiency of EPD. Even provided that the current density and suspension concentration are controlled during EPD, the process markedly deviates from linearity.[128] Electrolysis of water produces gases, which interfere with the formation of dense ceramic coatings.[57, 105] According to published data,[38, 129 – 132] EPD of ceramic materials, including materials for SOFCs, are usually carried out in non-aqueous organic media, most often, alcohols, ketones or their mixtures.

Nevertheless, there are fairly successful examples of using water as a dispersion medium, for example, for the formation of dense coatings based on zirconia and alumina using palladium cathodes, which absorb hydrogen formed upon water electrolysis,[133] or platinum electrodes.[134] It was noted above that EPD from aqueous solutions can be successfully implemented using pulsed direct and alternating current fields.[123, 124] To attain the required electrical conductivity of the medium, some researchers added water to non-aqueous suspensions.[55, 135, 136] Talebi *et al.*[135] demonstrated that addition of 4 vol.% of water to a suspension of YSZ in a mixture of acetone and ethanol considerably increases the quality of electrophoretically deposited films.

For preparing suspensions of SOFC materials, water is mainly replaced by alcohols, which can form (like water molecules) hydrogen bonds with the surface of solvated oxides. Isopropyl alcohol is most convenient for industrial use as it is less hygroscopic than ethanol and, as a consequence, it ensures stability of the physicochemical properties of the dispersion medium during the preparation and use of the suspension. Apart from alcohols, ketones are also utilized; their carbonyl group is capable of donor-acceptor interaction with the oxide surface. Among various ketones, acetylacetone proved itself to be a good medium for EPD.[136 – 138] It is used as a single dispersion medium or as

‡ Here and below, the density is indicated in percent of the theoretical value.

mixtures with alcohols taken in different volume ratios.[35, 54, 130, 132, 139] In many practically important cases, it is necessary that the dielectric constant of the suspension be $\leqslant 12$. Meanwhile, when the dielectric constant is above 25, the electrophoretic mobility of particles will be restricted due to a high concentration of ions, which become the main charge carriers in the suspension.[140]

3.2.2. pH-Control agents. Methods for deaggregation of suspensions

The aggregation of single particles, especially nano-sized ones, can occur even in stable suspensions; as a result, the average particle size in the suspension differs from the size of single particles.[132, 141] The acidity of suspension can affect the surface charge of the particle and the ζ-potential.[142] For example, the ζ-potential of an aqueous YSZ suspension is positive at low pH and is negative when the pH is higher than the isoelectric point (IEP), which is 4 – 6.[105, 140, 143, 144] In the case of YSZ suspension in acetylacetone, IEP was observed at pH 7.4 and the pH dependence of the ζ-potential was U-shaped.[145] During titration of a suspension of the electrolyte nanomaterial $Ce_{0.8}(Sm_{0.75}Sr_{0.2}Ba_{0.05})_{0.2}O_{2-\delta}$ (CSSBO) in a liquid mixture (isopropyl alcohol + acetylacetone), the ζ-potential decreased as pH increased from 4 to 9, but the IEP was not reached.[130] Nevertheless, for non-aqueous suspensions of various materials, the stable state was normally observed at pH 4 – 5.8.[38, 146] Depending on the initial pH value, suspensions were stabilized using carboxylic acids,[147, 148] hydrochloric acid [145] and various bases: triethanolamine, monoethanolamine and 6-aminohexan-1-ol.[149] By varying pH, it was possible to increase the density of the deposited YSZ layer from 38% at pH 7.4 to 53% at pH 8.4.[149]

For the successful EPD process, suspensions with a narrow particle size distribution should be prefered. This is attained by means of ultrasonic treatment of suspensions [130, 150] and mechanical dispersion methods such as long-term grinding in a ball mill,[151, 152] magnetic stirring [153] or dissolver treatment.[154] It is shown in several studies that a combination of ultrasonic treatment and subsequent centrifugation can significantly increase the proportion of single particles and produce a narrow particle size distribution.[132]

The concentration of the solid phase in suspensions for EPD is one more important parameter for the formation of dense and uniform coatings. With increasing concentration of solid particles in the suspension, the mass and density of the coating increase.[48] However, too high concentration of particles in the suspension increases the viscosity, which has an adverse effect on the EPD,[155] because in suspensions with high particle concentrations, van der Waals attraction forces, which promote particle aggregation, start to predominate. The use of various dispersants [156, 157] and additives forming the particle charge (*e.g.*, molecular iodine) [139, 158, 159] is needed when the EPD is carried out from highly concentrated suspensions (20 – 100 g litre^{-1}). Chen and Liu [159] reported that free protons that are released upon the reaction of iodine with acetylacetone

$$MeC(O)CH_2C(O)Me + 2I_2 \rightleftharpoons$$
$$\rightleftharpoons ICH_2C(O)CH_2C(O)CH_2I + 2I^- + 2H^+$$

are adsorbed on the particles, giving rise to a positive charge and high positive ζ-potentials of the suspension.

The concentration of molecular iodine used for this purpose is usually relatively low (0.1 – 0.5 g litre^{-1}) because too high surface charge may hamper the EPD.[159]

3.2.3. Dispersants and polymer binders. Self-stabilization effect

The key difference between EPD and other colloidal methods is the absence or a very low content of organic components in suspensions, which makes it possible to obtain high-density coatings, with the density comparable with that of pressed samples.[160] However, polymer binders and dispersants, which play a variety of roles, are added to suspensions meant for EPD. The sedimentation stability of suspensions is increased by phosphoric acid esters,[157, 161] polyethyleneimine,[151, 162] ammonium polyacrylate,[39] benzoic acid [131] and so on. The concentrations of these components are usually 0.01 – 2.5 g litre^{-1}. The powders obtained by chemical methods (pyrolysis, citrate nitrate method, *etc.*) are highly aggregated. In order to enhance the sedimentation stability of suspensions of these powders and, hence, to increase the quality of coatings, the suspensions meant for EPD are doped with iodine, stabilizers, dispersants, water, inorganic and organic acids and bases. The suspensions based on commercial YSZ powders, samarium- (CSO) or gadolinium-doped ceria (CGO) manufactured by Tosoh and Daiichi Kigenso (Japan), Sigma-Adrich (UK), Fuel Cells Materials (US), in which the average particle size varies from 0.1 to 0.5 μm, are also stabilized by addition of molecular iodine and various dispersants.[33, 35, 39, 140]

The use of nano-sized materials in SOFC technology gives an advantage in obtaining high-conductivity dense thin electrolyte films at a reduced sintering temperature; thus, it is possible to preserve the structure of the supporting electrodes and, hence, significantly increase the cell productivity. The nano-sized SOFC materials can be obtained using various methods: sol – gel process, hydrothermal process, spray pyrolysis, *etc.*[163] However, the preparation of EPD suspensions from nanopowders was noted to be sophisticated, due to the tendency for aggregation caused by a high level of interfacial interaction.[164] Thus, it is not always possible to avoid the addition of dispersants to nano-sized suspensions. For example, stable suspensions of nano-sized 8YSZ (22 nm) obtained by the sol – gel method were doped with a phosphoric acid ester.[37] It is known that burning-out of this dopant gives impurities remaining in the films that may have an adverse effect on the functional properties of the films.[157] In this respect, a good alternative is the use in EPD technology of slightly aggregated nanopowders composed of 10 – 20 nm spherical particles obtained by laser evaporation followed by condensation (LEC),[165, 166, 167] because this makes it possible to completely avoid the application of dispersants and molecular iodine.

A series of studies of Kalinina and co-workers [110, 130, 168] deals with stable suspensions of materials obtained by LEC for the use in EPD technology and with the effect of deaggregation of 8YSZ nanoparticles in suspensions on the electrophoretic deposition process.[132, 169] For example, a study of non-aqueous suspensions of the $Ce_{0.8}Sm_{0.2}O_{1.9}$ (CSO20), $Ce_{0.8}Gd_{0.2}O_{1.9}$ (CGO20) and $Ce_{0.8}(Sm_{0.75}Sr_{0.2}Ba_{0.05})_{0.2}O_{2-\delta}$ (CSSBO) nanopowders obtained by LEC was reported.[130] The electron micrographs of the powders, particle size distribution curves and pH dependences of the ζ-potential for these non-aqueous suspensions are depicted in Fig. 8.

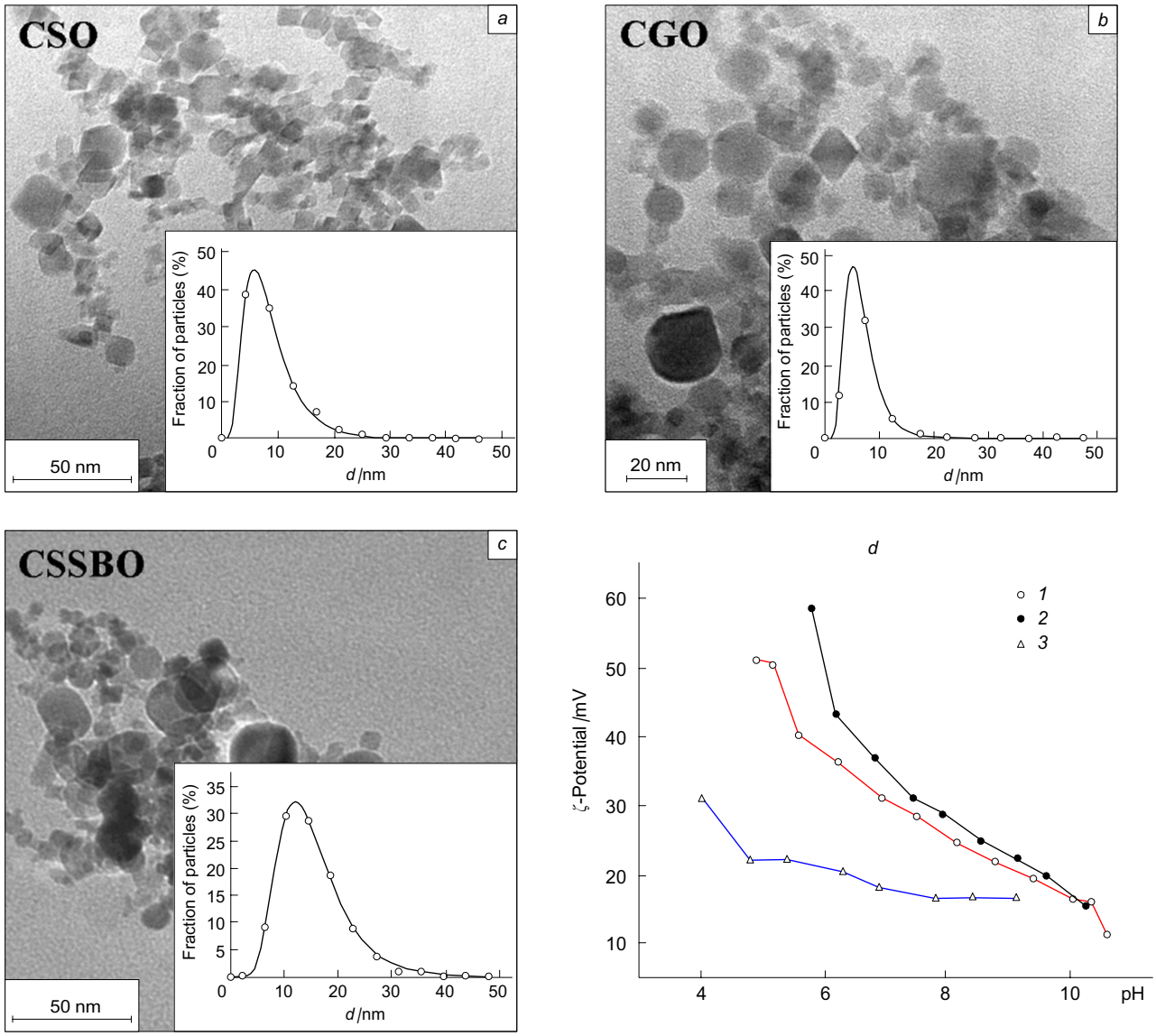


Figure 8. Electron micrographs and particle size distribution curves (*a*–*c*) and pH dependences of the ζ-potential for 2% suspensions of CSO20 (*1*), CGO20 (*2*) and CSSBO (*3*) nanoparticles in isopropyl alcohol : acetylacetone = 50 : 50 (vol.%) (*d*) according to the data of acoustic measurements on a DT-300 unit.[130]

It was shown that the initial nanopowder suspensions are weakly acidic and have relatively high initial ζ-potentials. Despite the presence of aggregates, the LEC-produced suspensions of nanopowders are stable without addition of special stabilizers because of spontaneous formation of EDL on the surface.[168]

One of the purposes of polymer binders (polymer modifiers) added to suspensions is to prevent cracking of coatings during drying (cracking is typical of coatings based on nanomaterials).[157] The addition of a polymer modifier to a nanoparticle suspension brings about a competition of pairwise interactions of molecules of the medium and polymer macromolecules with the surface: the polymer modifier should destroy the solvation layer and be adsorbed on the nanoparticle surface. It was found that introduction of BMC-5 (butyl methacrylate copolymer with 5 mol.% methacrylic acid) in a 2.5 – 3 g litre^{-1} amount into a suspension of nano-sized LEC powders based on doped CeO_2 completely prevented film cracking during drying.[110] The density of films obtained in the presence of BMC-5 was 48% – 60% and complete burning-out of the additive took place in the temperature range of 250 – 400 °C. Other compounds used by various authors as additives to non-aqueous suspensions of nano- and micro-powders to prevent cracking of the coatings include polyvinylbutyral (PVB), poly(acrylic acid), poly(vinyl acetate), polyethyleneimine, acrylic acid and acrylate copolymers, acrylate and acrylamide copolymers, *p*-hydroxybenzoic acid and other compounds.[151, 157, 161, 162, 170] In some studies, it was noted that certain dispersants can also act as polymer binders. For example, polyethyleneimine and polyallyldimethylammonium chloride (cationic polyelectrolyte, a linear-cyclic macromolecular compound), which act as dispersants, can also prevent cracking of the coatings.[106, 171, 172] For aqueous suspensions, water-soluble poly(vinyl alcohol) is the most popular binder.[106, 173]

Table 1. Compositions of suspensions based on SOFC materials.

SOFC material			Dispersion medium	Additives	Ref.
designation (composition)	manufacturer	other characteristics [a]			
Oxygen-ion conducting solid electrolytes					
8YSZ ($Zr_{0.92}Y_{0.08}O_{2-\delta}$)	Tosoh	–	Ethanol	Poly(ethylene glycol)	34
8YSZ ($Zr_{0.92}Y_{0.08}O_{2-\delta}$)	Tosoh	–	Acetylacetone	Darvan 821-A dispersant, ammonium polyacrylate	35
8YSZ ($Zr_{0.92}Y_{0.08}O_{2-\delta}$)	Tosoh	d = 100 – 200 nm	Acetone + ethanol	Molecular iodine	36
8YSZ ($Zr_{0.92}Y_{0.08}O_{2-\delta}$)	–	Sol – gel method, d = 22 nm	Isopropyl alcohol	Phosphate ester	37
8YSZ ($Zr_{0.92}Y_{0.08}O_{2-\delta}$)	Daiicghi Kigenso, Japan	d = 0.5 μm	Distilled water	Ammonium polyacrylate	39, 134
8YSZ ($Zr_{0.92}Y_{0.08}O_{2-\delta}$)	Tosoh	d = 0.3 μm	Ethanol, methanol, n-propanol, isopropyl alcohol, n-butanol, ethylene glycol, acetone, acetylacetone	Molecular iodine	129
8YSZ ($Zr_{0.92}Y_{0.08}O_{2-\delta}$)	Tosoh	–	Isopropyl alcohol	Electrostatic dispersants	131
8YSZ ($Zr_{0.92}Y_{0.08}O_{2-\delta}$)	–	LEC, d = 11 nm	Isopropyl alcohol + acetylacetone	BMC-5	132
8YSZ ($Zr_{0.92}Y_{0.08}O_{2-\delta}$)	Tosoh	–	Acetylacetone, acetone	Molecular iodine	136
8YSZ ($Zr_{0.92}Y_{0.08}O_{2-\delta}$)	Tosoh	–	Ethanol	Polyethyleneimine	151
8YSZ ($Zr_{0.92}Y_{0.08}O_{2-\delta}$)	–	–	Ethanol	Phosphate ester, poly(vinyl butyral – vinyl alcohol – vinyl acetate)	157
8YSZ ($Zr_{0.92}Y_{0.08}O_{2-\delta}$)	Tosoh	–	Acetylacetone, acetone, ethanol, acetone + ethanol	Molecular iodine	159
8YSZ ($Zr_{0.92}Y_{0.08}O_{2-\delta}$)	Tosoh	–	Isopropyl alcohol	Molecular iodine	174
10SSZ ($Zr_{0.9}Sc_{0.1}O_{1.95}$)	Daiichi Kigenso Kogyo Kagaku	–	Acetylacetone	Molecular iodine	175
1 mol.% CeO_2 – 89 mol.% ZrO_2 – 10 mol.% Sc_2O_3	Daiichi Kigenso Kogyo Kagaku	–	n-Propanol	Polyvinylbutyral	176
CSSBO ($Ce_{0.8}(Sm_{0.75}Sr_{0.2}Ba_{0.05})_{0.2}O_{2-\delta}$)	–	LEC, d = 15 nm	Isopropyl alcohol + acetylacetone	BMC-5	54, 110
CSO20 ($Ce_{0.8}Sm_{0.2}O_{1.9}$)	–	LEC, d = 9 nm	Isopropyl alcohol + acetylacetone	BMC-5	130
CGO20 ($Ce_{0.8}Gd_{0.2}O_{2-\delta}$)	–	LEC, d = 7 nm	Isopropyl alcohol + acetylacetone	BMC-5	130
CSO20 ($Ce_{0.8}Sm_{0.2}O_{1.9}$)	–	Spray pyrolysis, d = 290 nm	Ethanol	Molecular iodine	150

Table 1 (continued).

SOFC material			Dispersion medium	Additives	Ref.
designation (composition)	manufacturer	other characteristics [a]			
		Oxygen-ion conducting solid electrolytes			
CGO20 ($Ce_{0.8}Gd_{0.2}O_{2-\delta}$)	–	–	Ethanol	Phosphate ester, poly(vinylbutyral – vinyl alcohol – vinyl acetate)	157
CSO20 ($Ce_{0.8}Sm_{0.2}O_{1.9}$)	Hosokawa Micron	d = 49 nm	Acetylacetone	Molecular iodine	177, 178
CSO20 ($Ce_{0.8}Sm_{0.2}O_{1.9}$)	–	–	Acetone + ethanol	Molecular iodine	179
LSGM ($La_{0.83}Sr_{0.17}Ga_{0.83}Mg_{0.17}O_{3-\delta}$)	–	d = 10 μm	Ethanol + acetone	Molecular iodine	152
LSGM ($La_{0.8}Sr_{0.2}Ga_{0.8}Mg_{0.2}O_{3-\delta}$)	–	–	Acetone	Water, molecular iodine	180
LASO ($La_{9.83}Si_{4.5}Al_{1.5}O_{26}$)	–	Sol – gel method	Ethanol, methyl ethyl ketone, n-butylamine, polyvinylbutyral	HCl, HNO_3, acetic acid	156
LSO ($La_{9.33+2x}(SiO_4)_6O_{2+3x}$) $0 < x < 0.33$	–	d = 0.9 μm	Ethanol	Polyethyleneimide	162
LBAYO ($La_{0.9}Ba_{0.1}Al_{0.9}Y_{0.1}O_3$)	–	–	Acetone + ethanol	Molecular iodine	181
		Proton conducting solid electrolytes			
BCS20 ($BaCe_{0.8}Sm_{0.2}O_{3-\delta}$)	–	LEC, d = 32 nm	Isopropyl alcohol + acetylacetone	BMC-5	126
BCGCu ($BaCe_{0.89}Gd_{0.1}Cu_{0.01}O_{3-\delta}$)	–	Pyrolysis, d = 1 – 10 μm	Isopropyl alcohol + acetylacetone	BMC-5	127
BCY20 ($BaCe_{0.8}Y_{0.2}O_{3-\delta}$)	–	Citrate nitrate synthesis S_{BET} = 7.88 $m^2 g^{-1}$	Acetylacetone	Molecular iodine	170
BCY10 ($BaCe_{0.9}Y_{0.1}O_{3-\delta}$)	–	d = 100 nm	Acetylacetone	Molecular iodine	182, 183
BCY10 ($BaCe_{0.9}Y_{0.1}O_{3-\delta}$)	–	Pechini method, glycine nitrate method	Methyl ethyl ketone, ethanol, acetylacetone, isopropyl alcohol, isobutyl alcohol	Polyacrylic acid	184
BZCY ($BaZr_{0.4}Ce_{0.4}Y_{0.2}O_{3-\delta}$)	–	Glycine nitrate method	Ethanol	–	185
LCN ($La_{0.995}Ca_{0.005}NbO_4$)	Cerpotech	–	Acetylacetone and deionized water	Molecular iodine	186
		Cathode materials			
LMO ($LaMnO_3$)	–	Pechini method, d = 213 nm	Isopropyl alcohol	Poly(vinyl alcohol)	153
LSM64 ($La_{0.6}Sr_{0.4}MnO_{3-\delta}$)	–	Solid phase synthesis, micro-sized powder	Isopropyl alcohol + acetylacetone	–	154

Table 1 (continued).

SOFC material			Dispersion medium	Additives	Ref.
designation (composition)	manufacturer	other characteristics [a]			
		Cathode materials			
LNC ($La_2Ni_{0.8}Cu_{0.2}O_{4+\delta}$), LSNF ($La_{0.8}Sr_{0.2}Ni_{0.6}Fe_{0.4}O_{3-\delta}$)	–	Pechini method	Methyl ethyl ketone	Molecular iodine	158
LN ($La_2NiO_{4+\delta}$)	–	Pyrolysis, S_{BET} = 1.2 $m^2 g^{-1}$; LEC, S_{BET} = 53 $m^2 g^{-1}$	Isopropyl alcohol, acetone, acetylacetone, isopropyl alcohol + acetylacetone	BMC-5	187
$La_{0.7}Sr_{0.3}MO_{3-\delta}$ (M = Mn, Fe, Co)	–	Solid phase synthesis, d = 0.4 – 0.8 μm	Acetylacetone	Molecular iodine	188
LSM82 ($La_{0.8}Sr_{0.2}MnO_{3-\delta}$)	–	Glycothermal synthesis, S_{BET} = 2.65 $m^2 g^{-1}$	Acetylacetone	Molecular iodine	189
NiO – YSZ (NiO – $Zr_{0.92}Y_{0.08}O_{2-\delta}$)	Toho Titanium, Tosoh	S_{BET} = 8.74 $m^2 g^{-1}$	Acetylacetone	Molecular iodine	189
LSM82 – 8YSZ ($La_{0.8}Sr_{0.2}MnO_{3-\delta}$ – $Zr_{0.92}Y_{0.08}O_{2-\delta}$)	–	Pechini method, S_{BET} = 15 $m^2 g^{-1}$	Acetylacetone	Molecular iodine	190
LSCF ($La_{0.6}Sr_{0.4}Co_{0.8}Fe_{0.2}O_{3-\delta}$)	–	Sol – gel method	Acetylacetone	Molecular iodine	191
LSCF, CSO20 – Li_2CO_3 – Na_2CO_3	Sigma Aldrich, Malaysia	–	Ethanol, water	Polydiallyldimethylammonium chloride	50
		Anode materials			
8YSZ ($Zr_{0.92}Y_{0.08}O_{2-\delta}$)	Tosoh Co.	d = 200 nm	Ethanol, acetone, methanol, isopropyl alcohol, acetylacetone, n-butanol	Molecular iodine	48
NiO	Sigma Aldrich	d = 5 μm	Ethanol, acetone, methanol, isopropyl alcohol, acetylacetone, n-butanol	Molecular iodine	48
$La_{0.995}Ca_{0.005}NbO_4$/Ni	Ceprotech	S_{BET} = 5.93 $m^2 g^{-1}$	Acetylacetone	Molecular iodine, water	186
Ni – 8YSZ	–	–	Acetylacetone	Molecular iodine	192, 193
NiO (99.9%)	Canadian INCO Metals.	–	Acetone	Molecular iodine	194
8YSC	Tosoh	–	Acetone	Molecular iodine	194
Sr_2FeMoO_6	–	Citrate – gel method	Ethanol, isopropyl alcohol + acetone	Phosphate ester, molecular iodine	195
		Composite materials for protective coatings			
$(Mn,Co)_3O_4$	Pixar Co.	d = 0.9 μm	Ethanol	–	42
LNF ($LaNi_{0.6}Fe_{0.4}O_{3-\delta}$)		Pechini method	Ethanol		44

Table 1 (continued).

SOFC material			Dispersion medium	Additives	Ref.
designation (composition)	manufacturer	other characteristics [a]			
		Composite materials for protective coatings			
$MnCo_2O_4$, $MnCo_{1.7}Fe_{0.3}O_4$, $MnCo_{1.7}Cu_{0.3}O_4$	–	Pyrolysis, d = 0.7, 0.63 and 1.2 μm	Isopropyl alcohol + ethanol	–	45, 196
$Mn_{1.5}Co_{1.5}O_4$ + sintering additive (0, 5 or 10 mass % CuO)	American Elements	S_{BET} = 12.0 $m^2 g^{-1}$	Ethanol + deionized water	–	46, 197
$Mn_{1.02}Co_{1.94}Fe_{0.11}O_4$	H.C.Starck, Goslar	$d \leqslant 500$ nm	Acetone	HCl	198
$CuMn_{1.8}O_4$	–	Glycine nitrate synthesis	Ethanol + acetone	Molecular iodine	47, 199, 200
$NiFe_2O_4$	–	Solid phase synthesis, $d < 10$ μm	Acetone	Polyethyleneimine	201

Note. Here and in other Tables, dash means the absence of appropriate data in the literature sources.
[a] Method of synthesis, particle size (d) and Brunauer – Emmett – Teller specific surface area (S_{BET}).

The dispersion media and additives used most often to prepare suspensions based on various SOFC materials are summarized in Table 1.

3.3. Requirements to substrates for EPD

A specific feature of SOFC electrodes is high porosity (30% – 35%) needed to ensure the supply of a gaseous oxidant (usually air oxygen) or a reducing agent (usually hydrogen) to the electrochemical reaction zone. For successful electrophoretic deposition of a dense electrolyte layer on the electrode surface the following conditions should be met: high conductivity of the substrate and uniform electrical properties of the substrate surface; the absence of non-conductive inclusions (pores, non-conductive organic bonds), minimum surface roughness ($\leqslant$0.20 μm). The desirable pore size on the deposition surface is not more than 1 μm. Furthermore, the thermomechanical properties of the substrate electrode and the electrolyte layer should be similar, and the stability of the substrate structure upon electrolyte sintering is required.

Cathodic substrates possessing high conductivity were the first to be chosen for the EPD in SOFC technology. In some studies, deposition of 8YSZ was carried out with substrates based on lanthanum strontium manganites traditional for high-temperature SOFCs.[32, 159, 202 – 206] Ishihara *et al.*[202] carried out the deposition of 8YSZ on the porous $La_{0.8}Sr_{0.2}MnO_3$ cathode by repeated EPD. After the first deposition cycle, the film had numerous defects; however, after six and ten cycles, defect-free films with a thickness of 10 and 15 μm, respectively, were obtained. The films were sintered at a reduced temperature (1275 °C) to avoid reactions between materials. Peng and Liu[204] reduced the temperature of substrate formation for $La_{0.85}Sr_{0.15}MnO_3$ (LSM) obtained by the sol – gel process to 1250 °C. It was noted that the substrate shrinkage promotes sintering of the film deposited on this substrate. Chen and Liu[159] employed the Pechini method to prepare submicrometre LSM. When green LSM or LSM – 8YSZ substrates were used for the EPD, the deposition rate was low and the resulting electrolyte films were non-uniform because of the low conductivity of the substrates. The preliminary annealing of the substrates at 700 °C increased their conductivity, which resulted in the formation of 10 μm-thick uniform dense films. As in the study cited above,[204] it was noted that shrinkage of the substrate intensifies the sintering of the electrolyte film, gas tightness of which is already achieved at 1250 °C. For increasing the efficiency of deposition of the 8YSZ film, Lee *et al.*[205] attached the LSM substrate with 40% porosity to a conductive copper foil. Deposition at constant voltages of 10, 30 and 50 V over 10 min gave 1.5, 2.8 and 3.8 μm-thick films, respectively. Kalinina *et al.*[154] studied the EPD of LEC nano-sized 8YSZ powder on an LSM substrate with different average pore sizes — LSM1 (up to 1 μm) and LSM2 (3 – 20 μm). Analysis of the particle size distribution of the suspensions prior to the EPD demonstrated that the fraction of single 8YSZ particles (14 nm) substantially (on average, ten times) exceeded the fraction of aggregates (155 nm). It was found that for up to 1 μm sized pores, due to the overlap of the particle and electrode EDLs, the aggregates are deposited in the pores near the surface to form a dense coating (LSM1 substrate). When the pore size increases (LSM2 substrate), the deposition occurs inside the cathode, and the 8YSZ layer is not formed on the electrode surface.

Few studies address the EPD on cathode substrates. This is due to the fact that sintering of electrolyte films requires high temperatures. Meanwhile, sintering of electrolyte films at high temperature is accompanied by degradation of the cathode structure. One way to solve this problem is to find cathode materials that would exhibit low sinterability combined with high electrochemical activity. Indeed, Kalinina *et al.*[54, 207] carried out the EPD using a porous multilayer cathode substrate with an LNF current collector of optimized porosity (35% – 40%; collector thickness of 1 mm) and electrical properties (200 S cm^{-1}) and a thin LN functional layer (30 μm, up to 1 μm pores). During sintering of an electrolyte film (8 μm) at 1400 °C, no structural changes of the porous substrate were detected.

The problems faced by researchers while conducting EPD on cathode substrates initiated studies dealing with deposition on anode substrates. In some works, deposition was carried out on reduced nickel cermet substrates.[151, 175] A number of processes were developed for EPD on non-conductive NiO – 8YSZ substrates.[31, 208, 209] The surface of dense non-conductive substrates was activated by applying various conductive sublayers such as platinum,[136] polymers[210, 211] and graphite.[212] The conductive layer was applied either on the deposition surface or on the back side of the substrate; alternatively, a conductive material was introduced directly into the substrate and subsequently burned out. For activating EPD, a conductive plate was applied on a porous non-conductive substrate, most often, on the back side. In some publications (see, *e.g.* Refs 35, 55, 209 and 213), it was noted that the substrate porosity becomes the key factor in this case, because the solvent-saturated continuous pores in the substrates promote the formation of a 'conductive path' between the conductive plate and the suspension particles. The minimum threshold porosity of the substrate for the EPD to proceed was more than 50%.[55]

Talebi *et al.*[135] reported a comparison of two methods: (i) a thin graphite layer was deposited on the NiO – 8YSZ substrate surface and then a 8YSZ film was deposited onto the graphite layer; (ii) a 8YSZ film was formed on the surface of the NiO – 8YSZ substrate, with a steel electrode located on the substrate back side. It was noted that the mass of the coatings formed on the graphite layer was markedly greater than that in the case of coatings deposited directly on the non-conductive substrate. The current strength and layer microhardness and adhesion were also greater on the substrate with the graphite sublayer.

Das and Basu[213] investigated the effect of thickness (0.5 – 2 mm) of a NiO – 8YSZ porous non-conductive substrate, comprising the supporting and functional layers and pre-annealed at 1100 °C, on the rate of deposition of an electrolyte film. A steel plate was attached to the back side of the substrate, and a similar larger plate was used as the counter-electrode. It was found that uniform dense 8YSZ films can be formed on substrates with a thickness of up to 1 mm. As the substrate thickness increased fourfold (from 0.5 to 2 mm), the thickness of the deposited electrolyte film increased insignificantly (from 7 to 12 μm). Probably, the formation of dense 8YSZ films on the substrates in the early period of deposition suppressed further film growth. The highest open-circuit voltages (OCV) (1.18 V) and power density (1.41 W cm^{-2} at 800 °C) were obtained for the cells with a thinner substrate (0.5 mm) and with the 8YSZ film (7 μm). While summarizing the experience in conduct-

ing EPD on non-conductive substrates, the authors noted that the use of conductive plates to activate the EPD is more economic, since the plates can be reused.

3.4. Effect of deposition parameters

The EPD regime is determined by the following parameters: external electric field strength; deposition time; composition of the suspension; temperature; and the presence and velocity of stirring. According to published data,[31, 32, 38] the electrophoretic transfer of particles is successfully accomplished over a broad range of electric field strengths. According to the classical electrophoresis equation (7), mass transfer is proportional to the field strength, concentration of the suspension, electrophoretic mobility and time. By varying these values, one can control the amount of deposited material. The real situation is markedly complicated for concentrated suspensions [86] and for depletion of the suspension with increasing deposited mass.[85] The mass growth rates are considerably different for constant-current and constant-voltage depositions,[80] with considerable roles of the deposited layer resistance and change in the suspension resistance.[74, 75] The time dependences of the deposited mass for various EPD conditions are depicted in Fig. 9. Theoretically, these dependences could be used to initially specify the EPD conditions that would result in a particular deposited mass on the electrode; however, in practice, EPD parameters are usually selected empirically for each suspension and each substrate. The details of deposition conditions and parameters of the resulting coatings are reflected in Table 2.

Above, it was noted that the ionic composition of the dispersion medium,[137] which can change during deposition,[90] plays a significant role. In this respect, it is preferable to choose the deposition time of 1 – 5 min and adjust appropriately the field strength. A necessary parameter of an electrolyte coating is gas tightness, which can be achieved by successive deposition – sintering cycles (this method was first used by Ishihara *et al.*[136]) or by changing the particle size distribution of the suspension *via* sedimentation [170] or centrifugation [37] to remove large aggregates. Conduction of repeated cycles of EPD was also reported.[54, 215]

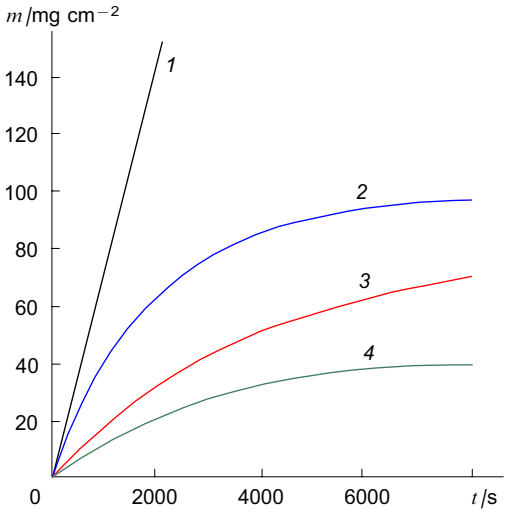


Figure 9. Theoretical time dependences of the deposited mass for various EPD regimes.[80]
Deposition: (*1*) constant current and constant concentration of the suspension; (*2*) constant current and decreasing concentration; (*3*) constant voltage and constant concentration; (*4*) constant voltage and decreasing concentration.

The formation of relatively thick coatings (up to 150 – 200 μm) is achieved using highly concentrated suspensions (100 g litre^{-1}) with the addition of a dispersant (*e.g.*, phosphate ester) to maintain the stability and electrophoretic mobility and a polymeric binder to prevent crack formation in the thick coating.[157]

Other important factors are smoothness and uniformity of the coating surface, which are often achieved by selecting an optimal deposition voltage. When the voltage is too low or too high, either partial substrate coating or non-uniform film surface may be observed.[129] The kinetics of the increase in the deposited mass may have either linear or non-linear time dependence (see Table 2), which can be attributed to different shielding effects of the deposited layer, a change in the suspension resistance or different patterns of variation of the particle concentration.

4. Application of electrophoretic deposition in the solid oxide fuel cell technology. Achievements and prospects

4.1. Formation of supporting ceramic parts

Early publications on the application of EPD in the SOFC technology were devoted to the formation of ceramic parts from an electrolyte based on yttria-stabilized zirconia. An advantage of this process consisted in the possibility to fabricate both flat and tubular parts. The density of the deposited items reached 58.5%; this made it possible to decrease the sintering temperature required to attain gas tightness (99.5%) to 1500 °C in air.[217] Zirconia tubes (with a length of 110 mm, outer diameter of 34 mm and wall thickness of 0.5 – 1.5 mm) had characteristic strength σ_c = 420 MPa. Negishi *et al.*[218] proposed a process for the EPD fabrication of tubular items based on lanthanum strontium cobaltite ferrite (LSCF).

To our knowledge, no examples of application of EPD in the formation of 3D parts of SOFCs can be found in the publications that appeared after 2006; however, there are examples of using this method for compaction of other ceramic materials. For example, EPD was employed to obtain optically transparent ceramic bodies of alumina, yttria, yttrium aluminium garnet and lutetium aluminium garnet from aqueous suspensions of nanopowders.[219] For the conduction of EPD, plastic moulds (35 × 35 × 4 mm) cut from Plexiglas with 6 mm holes were attached to working electrodes; this allowed fabrication of cylindrical samples in one EPD cycle at a voltage of up to 180 V and deposition time from 3 to 15 min. The deposits were dried on the electrode or in a mould in the case of cylindrical bodies. Drying was carried out for several days at room temperature to avoid cracks. In order to slow down the drying process, a small amount of water was added to the desiccator (vapour phase drying). The resulting cylinders were sintered for 4 h at 1700 °C at a heating rate of 5 °C min^{-1}. The EPD process gave high-density green bodies (61% – 62%); therefore, after sintering, uniform optically transparent ceramic bodies were obtained.

This method was further developed in a patent,[220] which proposed a process for fabrication of high-density optically transparent ceramics by EPD of slightly aggregated oxide

Table 2. Key parameters of the EPD process and properties of the resulting SOFC coatings.

Substrate type	Deposited material	Suspension characteristics	EPD regime [a]	Coating characteristics [b]	Notes	Ref.
			Oxygen-ion conducting solid electrolytes			
Stainless steel or porous LSM cathode	8YSZ, d = 20–30 and 51–65 nm	Acetylacetone, ethanol, their mixture (1 : 1), C_s = 4 and 10 g litre	I = 0.1, 0.25, 0.40 mA cm^{-2}; U = 300 V, L = 15 mm	$m \leqslant 7$ mg cm^{-2}, $h < 10$ μm	Linear increase in the deposited mass with time; minor increase in the deposit mass with concentration increase from 10 to 40 g litre^{-1}; defectiveness of the coatings after sintering depends on the particle size	33
Porous NiO–YSZ anode	8 YSZ (Tosoh)	Ethanol, poly(ethylene glycol) as the binder (5 mass %), C_s = 20 g litre^{-1}	U = 20–30 V, τ = 1.5–2.0 min	T_s = 1250 °C, h = 2.12 and 2.93 μm	Non-linear increase in the mass with time; deposition is due to the open porosity of the anode substrate	34
Porous Ni–YSZ anode	8YSZ (sol–gel method), $d \sim 22$ nm	Isopropyl alcohol, phosphate ester (0.1 g litre^{-1})	U = 10–70 V, τ = 1–10 min, L = 40 mm	T_s = 1200 °C during 2 h h = 3 μm	Non-linear increase in the deposited mass; optimal voltage range of 40–50 V; deposition for 10 min with preliminary centrifugation	37
Porous LNF/LN cathode	CSSBO (LEC), d = 15 nm	Isopropyl alcohol–acetylacetone (50 : 50 vol.%), C_s = 10 and 20 g litre^{-1}	U = 80 V, τ = 1 min (in a cycle), L = 10 mm	T_s = 1400 °C during 4 h, after 6 deposition cycles m = 5.6 mg cm^{-2}, h = 5 μm	Deposition–sintering cycles; compaction of the deposit in the centrifuge; ultrasonic treatment of the suspension	54
NiO–stainless steel anode	8YSZ (Tosoh), $d \sim 0.3$ μm	Ethanol, methanol, n-propanol, n-butanol, ethylene glycol, isopropyl alcohol, acetone, acetylacetone, C_s = 2.5 g litre^{-1}	U = 25, 50, 100 V, τ = 10–20 min, L = 12.5 mm	m = 7.5 mg cm^{-2} at 50 V	Non-linear increase in the deposited mass with time; smooth coating surface at low voltages (25 and 50 V), non-uniform surface with voltage increase up to 100 V	129
Porous LSM cathode and porous Ni–8YSZ anode	8YSZ (Tosoh)	Acetylacetone, acetone, C_s = 10 g litre^{-1}, I_2 additive	U = 5 and 10 V, τ = 3 min	m = 14.6 mg cm^{-2}, $h \approx 5$ μm after sintering, cyclic EPD	Linear increase in the deposited mass with time; application of five deposition–sintering cycles eliminates through pores in the coating	136
Al foil, Ni–CSO20 anode	CSO20 (spray pyrolysis) d = 290 nm	Ethanol, I_2 additive (0.6 g dm^{-3}), C_s = 10 g litre^{-1}	U = 100 V, τ = 1–10 min, L = 20 mm	T_s = 1600 °C, m = 4.6 mg cm^{-2}, h = 20 μm	Cracks and pores in the coating; relatively low specific gravity of the coating with a large thickness	150
Ni foil, Ni–8YSZ anode	$La_{0.8}Sr_{0.2}Ga_{0.875}Mg_{0.125}O_{3-\delta}$, $La_{0.8}Sr_{0.2}Co_{0.2}Fe_{0.8}O_{3-\delta}$, 8YSZ, CGO20	Ethanol; PVB (3 g litre^{-1}), phosphate ester (3.5 g litre^{-1}), C_s = 100 g litre^{-1}	I = 0.05–1 mA cm^{-2}, τ = 8 min, L = 1.5 cm	m = 50 mg cm^{-2}, h (without PVB) = 50–100 μm (cracks in the coating), h (with PVB) = 150–200 μm (no cracks)	Linear increase in the deposited mass with time; large thickness of the coating; highly concentrated suspension was used	157
NiO–8YSZ (green)	8YSZ (Tosoh), $d \sim 2$ μm	Methanol	U = 100 V, τ = 8 min, L = 10 mm	T_s = 1350 °C, h = 6–8 μm	Ultrasonic treatment of the suspension; co-sintering of the electrolyte layer and the anode	214

Table 2 (continued).

Substrate type	Deposited material	Suspension characteristics	EPD regime [a]	Coating characteristics [b]	Notes	Ref.
			Proton conducting solid electrolytes			
NiO – BCY10 anode	BCY20 (citrate nitrate method), d = 172, 766 nm	Acetylacetone, I_2 (0.33 g litre^{-1}), C_s = 8 g litre^{-1}	U = 30 V, τ = 3 min, L = 10 mm	T_s = 1450 °C for 4 h, h = 9.2 μm	Defect-free coating is provided by preliminary sedimentation of the suspension	170
NiO – BCY10 anode	BCY10	Acetylacetone, I_2 (0.37 g litre^{-1}), C_s = 8 g litre^{-1}	U = 30 – 60 V, τ = 1 – 5 min	T_s = 1550 °C for 2 h, h = 5.2 – 9.5 μm	Co-sintering of the electrolyte layer and the anode non-uniform coating with pores at 30 – 40 V voltage; optimal voltage of 50 – 60 V	182
Ni plate and porous Ni – YSZ and Ni – BCY10 anodes	BCY10 (Pechini and glycine nitrate methods), d = 0.3 – 1.0 μm	Methyl ethyl ketone, polyacrylic acid as the binder	U = 500 V cm^{-1}, τ = up to 10 min	m = 3.5 mg cm^{-2} in 5 min, h (green coating) = 20 μm	Low deposition rate at high voltage	184
Stainless steel and porous NiO – BZCY anode (1100 °C, 2 h)	BZCY (glycine nitrate method)	Ethanol, C_s = 10 g litre^{-1}	U = 30 – 100 V, τ = 1 – 5 min	h = 13 μm, electrolyte sintering at a 2 °C min^{-1} rate; 30 min at 1400°C, final sintering at 1500 °C for 2 h	Linear increase in the deposited mass with time; cracks in the coating at voltages of > 70 V; optimal voltages of 30, 50 and 70 V; higher coating density at 70 V; anode porosity decreased from 42.47% to 19.31% as the temperature increased from 1100 to 1500 °C	185
Dense LN cathode	BCS20, d = 0.3 μm and more; BCGCu, d = 1 – 10 μm	Isopropyl alcohol – acetylacetone (70 : 30 vol.%), C_s = 1 and 10 g litre^{-1}	U = 80 V, τ = 1 – 3 min (in a cycle), L = 10 mm	m = 3.2 mg cm^{-2}, h = 5 μm after six deposition – sintering cycles	Ultrasonic treatment and centrifugation of the suspension; deposition – sintering cycles; loose structure of green coating: the deposit was compacted in a centrifuge	215
Porous NiO – 8YSZ anode with a graphite sublayer	Bilayer electrolyte 8YSZ (d = 0.3 μm)/ CSO d = 1 μm	Ethanol, phosphate ester as the dispersant	U = 600 V, L = 10 mm	T_s = 1400 °C for 2 h; bilayer coating thickness: 8YSZ (4 μm)/CSO(1 μm)	Successive deposition of electrolyte layers on a porous substrate; co-sintering of the layers; linear time dependence of thickness (from 5 to 20 μm in 60 s)	216

[a] The values are: potential difference between the electrodes (U), characteristic deposition time (τ), distance between the electrodes (L) and current density (I).
[b] The values are: deposit mass (m), sintering temperature (T_s) and coating thickness (h).

nanoparticles from a non-aqueous suspension with a particle concentration from 0.1 mass % to 10 mass %. Large aggregates were removed by ultrasonic treatment and centrifugation of suspensions. The electric field strength during deposition was 50 to 300 V cm^{-1} and the process duration was 1 to 200 min, depending on the required thickness of the deposit. No organic dispersants or binders were required in this case for the formation of ceramic bodies. Deaggregation of the suspension by ultrasonic treatment and the subsequent particle separation according to sizes by centrifugation improved the uniformity of the body and decreased the defect generation during sintering.

4.2. Electrode-supported solid oxide fuel cells with thin-film electrolytes

The design of electrode-supported or porous metal substrate-supported SOFCs with thin-film electrolyte is most promising for the cells with reduced operating temperature.[12, 13] The first studies on the use of EPD in SOFC technology were mainly devoted to deposition of a traditional zirconia-based electrolyte on a lanthanum strontium manganite substrate.[32, 159, 202 – 206, 221] The LSM cathode-supported cell with a 10 μm-thick 8YSZ film electrolyte operating at 1000 °C using oxygen as the oxidant showed high OCV (1.0 V) and power density (1.5 W cm^{-2}).[136] The attention was focused on preservation of the porous structure of the cathode substrate upon sintering with the electrolyte. Ivanov *et al.*[222] studied the dependence of porosity of the $La_{0.7}Sr_{0.3}MnO_{3-\delta}$-based cathode substrate on the addition of pore-forming agents (graphite, cellulose, starch, hard coal), the mass ratio between the micro- and nano-sized powders, and formation temperature. It was found that porous substrates containing micro- and nano-sized LSM in a 50 : 50 ratio are less affected by high temperature (1250 °C) during the co-sintering with the 10YSZ electrolyte film than the other studied types of substrates. The authors were able to decrease the temperature of electrolyte sintering by using nano-sized 10YSZ synthesized by the LEC method (see Section 3.2.3). The resulting SOFC with the optimized cathode (50% porosity) and thin-film electrolyte (5 μm) had high OCV (~1.1 V) and power density (0.55 W cm^{-2}) at 860 °C. However, the authors noted that at a current density of >0.7 A cm^{-2}, clear-cut limiting currents appear in the current – voltage curves, which may be indicative of diffusion limitations hampering the oxidant supply through the porous cathode layer. Fung and Chen[181] proposed a new solid electrolyte, LBAYO, with the perovskite structure and improved electrical properties; they studied the possibility to form thin films of this electrolyte on lanthanum strontium manganite cathode substrates. Despite the reduced OCV value due to gas leakage in the cell (0.93 V at 800 °C) and rather large electrolyte thickness (63 μm), the power density of the cell was 0.306 W cm^{-2} (800 °C), which is comparable with characteristics of SOFCs with the traditional 8YSZ electrolyte.

Most of studies addressing the use of EPD for the formation of SOFCs consider anode-supported cells with thin-film electrolytes. It was noted above that in the case of non-conductive substrates (*e.g.*, nickel cermet), high porosity is the key parameter for the EPD (see Section 3.3). High shrinkage of the substrate can also intensify sintering of the electrolyte film. Therefore, in the formation of anode-supported SOFCs, additional procedures were used such as pre-annealing of the anode substrate at a moderate temperature (up to 1000 °C)[179, 209, 216] and introduction of pore-forming agents and conductive materials (*e.g.*, graphite) into the electrodes.[176, 182, 183]

Besra *et al.*[209] showed that, irrespective of the applied voltage, the deposited mass of the electrolyte film increases with increasing porosity of the substrate (which was adjusted by varying the amount of the pore-forming agent) (Fig. 10). The authors discussed the mechanism of formation of conductive paths from the substrate surface, where the deposition occurs, to the conductive backing attached to the substrate.

Horri *et al.*[221] increased the power of a single SOFC with the 8YSZ electrolyte (~10 μm) more than twofold by introducing 2.5 mass % and 5 mass % of carbon microspheres, obtained by hydrothermal treatment of table sugar, as pore-forming agents into the electrodes (Table 3). The electrolyte film thickness increased from 9 to 12 μm as the porosity of the anode substrate increased due to the change in the content of the pore-forming agent. The increase in the anode porosity also increased the fuel consumption efficiency during functioning of the cell

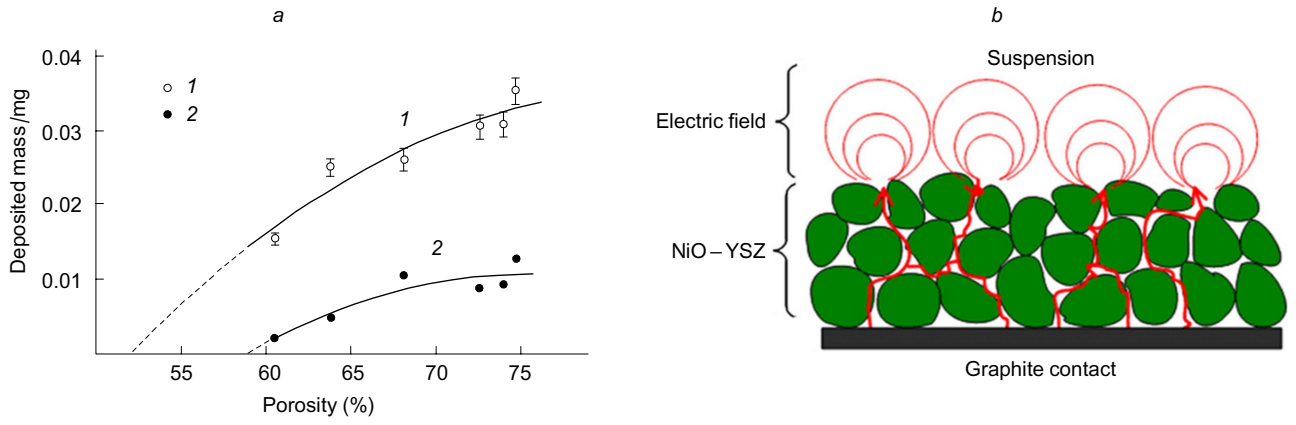


Figure 10. Deposited mass *vs.* porosity of the NiO – 8YSZ substrate (60 : 40) during the EPD from a suspension of 8YSZ particles in acetylacetone and (*a*) electric field distribution on the surface of a non-conductive substrate with open porosity (*b*).[209]
(*a*) (*1*) U = 100 V, τ = 3 min; (*2*) U = 25 V, τ = 3 min.

Table 3. Materials, regimes of formation of functional layers of SOFCs by EPD (unless another method is indicated) and characteristics of single SOFCs.

Characteristics of functional layers (composition, thickness and conditions of deposition and sintering in air)			OCV (see [a]) fuel/oxidant	Power / W cm^{-2} (see [b])	Ref.
electrolyte	cathode	anode			
8YSZ, h = 5 μm, U = 5 V, τ = 3 min (cyclic deposition, five stages), T_s = 1400 °C	$La_{0.6}Sr_{0.4}MnO_{3-\delta}$, painting, T_s = 900 °C	*NiO – Zr(Ca)O_2 (40 : 60), pressing, T_s = 1450 °C	1.03 (1000 °C); (H_2 + 3% H_2O)/O_2	1.84 (1000 °C)	136
10SSZ (10 μm) (700 °C), U = 5 – 10 V, τ = 5 – 50 min, T_s = 1300 °C	Pt – 10SSZ, tape casting, T_s = 1000 °C	*NiO – 10SSZ (40 vol.% Ni) + PMMA, pressing T_s = 900 °C (air) + 600 °C (H_2 + Ar)	1.0 – 1.1 V (900 °C); H_2/air	1.80 (900 °C), 1.20 (800 °C), 0.4 (700 °C), 0.1 (600 °C)	175
ScSZ ($Zr_{0.89}Sc_{0.10}Ce_{0.01}O_{2-\delta}$), h = 5 – 8 μm, U = 200 V, τ = 5 – 15 min, T_s = 1200 – 1275 °C	$(La_{0.85}Sr_{0.15})_{0.95}MnO_{3-\delta}$, painting, T_s = 1200 °C	*NiO – ScSZ (50 : 50) + graphite + soluble starch, pressing	~1.1 V (800 °C); (H_2 + 1.2% H_2O)/air	0.525 (800 °C), 0.440 (750 °C), 0.270 (700 °C)	176
CSO20, h = 18 μm, U = 60 V, τ = 1 min, T_s = 1350 °C	$Sm_{0.5}Sr_{0.5}CoO_{3-\delta}$ (SSC), screen printing, T_s = 1100 °C	*NiO – CSO20 (50 : 50), pressing, T_s = 750 °C	0.92 V; methane/air	0.155 (500 °C)	179
LBAYO, h = 63 μm, U = 30 V, τ = 10 min, T_s = 1450 °C	*LSM82, pressing, T_s = 1400 °C	BL: $Ce_{0.8}Sm_{0.2}O_{1.9}$ (CSO20), h = 10 μm; FL: NiO – 8YSZ (70 : 30), h = 40 μm, screen printing, T_s = 1500 °C	0.93 V (800 °C); (H_2 + 2% H_2O)/air	0.306 (800 °C)	181
BCY10, h = 9.5 μm, U = 60 V, τ = 5 min, T_s = 1000 °C + 1550 °C	$La_{0.8}Sr_{0.2}Co_{0.8}Fe_{0.2}O_{3-\delta}$ – $BaCe_{0.9}Yb_{0.1}O_{3-\delta}$ (50 : 50), h = 80 μm	*NiO – BCY10 (50 : 50) + graphite, pressing	1.05 V (700 °C); H_2/air	0.296 (700 °C), 0.275 (650 °C), 0.242 (600 °C), 0.203 (550 °C)	182, 183
8YSZ, h = 10 μm, U = 20 V, τ = 1 min, (cycling), T_s = 1275 °C	*$La_{0.8}Sr_{0.2}MnO_{3-\delta}$ (LSM) + pore-forming agent, pressing, T_s = 1350 °C	NiO, painting, T_s = 900 °C (air) + 1000 °C (H_2)	1.0 V (1000 °C); (H_2 + 3% H_2O)/O_2	1.5 (1000 °C)	202
8YSZ, h = 40 μm, U = 100 V, τ = 3 min, T_s = 1400 °C	LSM82 – 8YSZ (50 : 50), painting, T_s = 1150 °C	*NiO – 8YSZ (60 : 40) + starch (up to 40 mass %), pressing, T_s = 1000 °C	0.86 V (850 °C), 0.97 V (650 °C); H_2/air	0.264 (850 °C), 0.200 (800 °C), 0.153 (750 °C), 0.140 (700 °C), 0.060 (650 °C)	209
8YSZ (4 μm)/CSO20 (1 μm), U = 600 V, τ = 3 min, T_s = 1400 °C	$La_{0.6}Sr_{0.4}Co_{0.2}Fe_{0.8}O_{3-\delta}$ (LSCF), h = 30 μm, screen printing, T_s = 850 °C	*NiO – 8YSZ, tape casting, T_s = 900 °C	(H_2 + 3% H_2O)/air	0.71 (700 °C)	216
8YSZ (see [c]), h = 9 μm (c = 2.5) and 12 μm (c = 5), U = 100 V, τ = 3 min, T_s = 1400 °C	LSM82 – 8YSZ (55 : 45), painting, T_s = 1150 °C	*NiO – 8YSZ (60 : 40) + carbon microspheres (c = 2.5 or 5), pressing, T_s = 1000 °C	0.96 V (c = 0), 850 °C, 1.074 V (c = 2.5), 1.078 V (c = 5)	0.208 (c = 0), 850 °C, 0.431 (c = 2.5), 0.572 (c = 5)	221

Table 3 (continued).

Characteristics of functional layers (composition, thickness and conditions of deposition and sintering in air)			OCV (see [a]) fuel/oxidant	Power / W cm^{-2} (see [b])	Ref.
electrolyte	cathode	anode			
$Zr_{0.9}Y_{0.1}O_{2-\delta}$ (10YSZ), h = 5 μm, U = 20 – 200 V, T_s = 1250 °C	*$La_{0.7}Sr_{0.3}MnO_{3-\delta}$ (nano- and microparticles, 50 : 50), magnetic pulse pressing, T_s = 900 – 1200 °C	Pt	~1.1 V (860 °C); $(H_2 + Ar)/O_2$ 0.40 (760 °C),	0.55 (860 °C), 0.48 (815 °C), 0.25 (710°C), 0.15 (660°C)	222
8YSZ, h = 5 μm, U = 600 V, τ = 3 min, T_s = 1400 °C	LSCF, h = 30 μm, screen printing, T_s = 850 °C	*Ni – 8YSZ, tape casting, T_s = 900 °C	$(H_2 + 3\% H_2O)$/air	1.02 (800 °C), 0.61 (700 °C), 0.19 (600 °C)	223
LSGM, h = 30 μm, U = 80 V, τ = 2 min, T_s = 1490 °C	LSCF, painting, T_s = 850 °C	*Ni-impregnated composition $La_{0.4}Ce_{0.6}O_{2-\delta}$ + graphite, T_s = 900 °C	1.07 – 1.10 V (700 °C); H_2/air	0.780 (700 °C), 0.450 (650 °C), 0.275 (550 °C), 0.175 (500 °C)	224, 225

Notes. The supporting electrode in SOFCs with thin-film electrolyte is marked by asterisk.

[a] The value in parentheses is the temperature of OCV measurement.

[b] The value in parentheses is the temperature of power measurements.

[c] The value in parentheses is the content of the pore-forming agent for carbon microspheres [c /mass %]

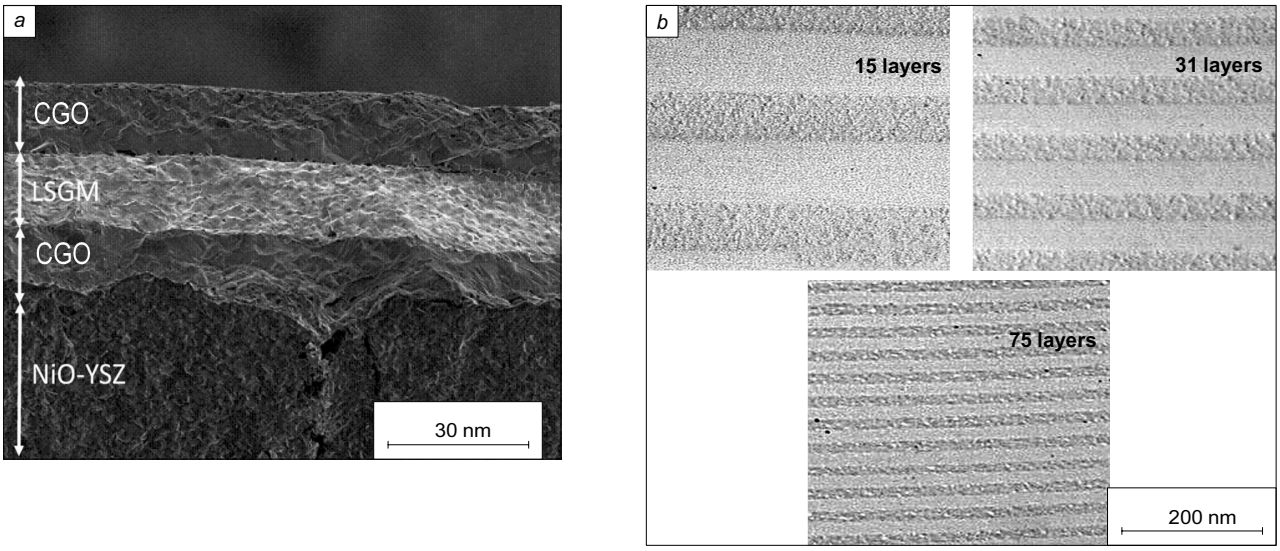


Figure 11. Examples of multilayer coatings obtained by EPD.
(*a*) SEM image of the CGO/LSGM/CGO electrolyte on the NiO – 8YSZ substrate;[211] (*b*) SEM mages of coatings with alternating 3YSZ (shown in dark grey) and 8YSZ (shown in light grey) layers.[114]

from 26.5% to 47.0% and 59.6% for the 0 mass %, 2.5 mass % and 5 mass % contents of the pore-forming agent, respectively.

A known way to decrease the interaction of the 8YSZ electrolyte with cathode materials based on La- and Sr-containing perovskites (manganites, cobaltites, *etc.*) is to employ barrier layers, most often, composed of doped CeO_2. The doped CeO_2 layers can also serve as protective layers on the anode side (protection from reduction) when combined with electrolytes based on lanthanum gallate, silicate or aluminate or based on bismuth oxide. As the natural development of this area, multilayer electrolyte structures were formed, in particular, by EPD.[211, 216, 226 – 228] In this case, EPD provides the following benefits: fast deposition, simplified control over the film thickness by tuning the deposition parameters and enhanced film adhesion. The combination of the individual properties of materials in a multilayer coating improves the performance of SOFCs as a whole.[226] For example, for single-layer 8YSZ (4 μm) and bilayer 8YSZ (4 μm)/CSO20 (1 μm) electrolytes formed by EPD on a supporting anode from ethanol-based suspensions, the power densities of 0.61 and 0.71 W cm^{-2}, respectively, at 700 °C were found. The EPD process can also be employed to form films comprising more layers. For instance, Suzuki *et al.*[211] prepared a trilayer CGO10/LSGM/CGO10 electrolyte with equal layer thickness (~15 μm) on a porous NiO – 8YSZ substrate with a polypyrrole conductive film. Fleckenstein *et al.*[112] fabricated multilayer coatings composed of 5, 31 and 75 alternating tetragonal 3YSZ and cubic 8YSZ layers with equal layer thickness of 125, 55 and 20 μm (Fig. 11). The multilayer structures obtained by EPD have high adhesion between the layers and high strength.[112 – 114]

The possibility of producing thin-film proton-conducting electrolytes by EPD is of considerable interest. These materials are promising for the use in intermediate- and low-temperature SOFCs and other electrochemical devices owing to their high proton conductivity, which arises in these materials at temperatures of < 600°C in a humid atmosphere.[14, 229 – 232] Currently, there are only few publications dealing with the EPD of proton conductors, However, Zunic and co-workers[182, 183] successfully developed a process for the manufacture of nickel cermet anode-supported barium cerate films, the conductivity of which was increased by addition of graphite, and attained high power characteristics for SOFCs (0.203 W cm^{-2} at 550 °C) comparable with those for SOFCs with the thin-film LSGM electrolyte[224] (0.275 W cm^{-2} at 550 °C).

Along with high conductivity and low activation energy, the advantages of materials based on doped barium cerate include their compatibility with a wide range of cathode materials with perovskite and layered structures.[233, 234] However, it is known that these materials are unstable in atmospheres containing H_2O, CO_2 or H_2S.[235] Currently, attention is given to the development of the EPD of electrolytes based on more stable barium cerate zirconates.[185] Intensive research of high-temperature proton conductors (based on calcium zirconate and also lanthanum scandate, yttrate and niobate)[14] possessing good electrical properties and acceptable stability is pursued in Russia and abroad; therefore, the development of the EPD technology for the formation of films of these materials is also in demand.

A new promising line of research is the design of single-chamber SOFCs. The EPD method was applied to form such a cell with the CSO20 electrolyte operating on a mixture of methane and air.[179] The use of thin-film electrolytes based on doped CeO_2 is more beneficial in single-chamber fuel cells than in SOFC designs with divided gas chamber, because with electrolyte thickness of < 5 μm short circuit may take place due to high electron conductivity arising in such electrolytes in a reductive atmosphere.[175] For a single-chamber cell with a 18 μm-thick CSO20 film, an acceptable power density was obtained, equal to 0.155 W cm^{-2} at 500 °C.

4.3. EPD for the formation of electrode structures

The development of studies dealing with the formation of electrode structures using the EPD method seems promising, since this method allows for unique electrode design (to form layers with controlled thickness and porosity, graded

Table 4. Characteristics of the EPD of electrode materials of SOFCs.

Substrate type	Deposited SOFC material	Regime of EPD and sintering in air	Coating parameters	Ref.
CGO10 electrolyte	LN, solid-phase synthesis	U = 20, 50 V, τ = 30 min, 12 T magnetic field, pore-forming agent 11 mass % – 33 mass %, T_s = 1100 °C	Reduced polarization loss for $a-b$ oriented electrode	47
Stainless steel	8YSZ (Tosoh Co.), h = 200 nm; NiO (Sigma Aldrich), h = 5 μm	U = 50 – 300 V, τ = 30 – 420 s	Trilayer functionally graded coatings Thickness: 10, 44, 68 μm, porosity: 29% – 14%	48
Stainless steel plate, molybdenum carbide tube	$LaMnO_3$, Pechini method, h = 213 nm	U = 500 V, τ = 15 min, T_s = 1200 °C (plate); U = 700 V, τ = 5 min T_s = 1300 °C (tube)	The cathode layer porosity (40%), was retained after deposition and sintering of the 8YSZ layer (T_s = 1200 °C)	153
Porous $La_{0.6}Sr_{0.4}MnO_{3-\delta}$ cathode	$La_{0.6}Sr_{0.4}MnO_{3-\delta}$ (LSM64), solid-phase synthesis	U = 100 V, τ = 1 min, T_s = 1050 °C	25 μm-thick fine-pored LSM sublayer	154
Lanthanum silicate-based electrolyte with the apatite structure	$La_2Ni_{0.8}Cu_{0.2}O_{4+\delta}$ (LNC) and $La_{0.8}Sr_{0.2}Ni_{0.6}Fe_{0.4}O_{3-\delta}$ (LSNF), Pechini method	U = 100 – 600 V, τ = 7 – 780 s, T_s = 1350 °C	2 – 140 μm-thick porous cathode layers	158
CGO10 electrolyte	$La_{0.6}Sr_{0.4}Co_{0.8}Fe_{0.2}O_{3-\delta}$ (LSCF), citrate method	U = 20 V, τ = 60 – 220 s, T_s = 950 – 1100 °C	Cathode layer thickness: 10 – 20 μm	161
Dense $La_2NiO_{4+\delta}$ cathode	$La_2NiO_{4+\delta}$ (LN), pyrolysis, S_{BET} = 1.2 $m^2\ g^{-1}$, LEC, 53 $m^2\ g^{-1}$	U = 100 V, τ = 1 min, T_s = 1400 °C	Mass of the coating: 4.4 mg cm^{-2}	187
$SrCe_{0.95}Yb_{0.05}O_3$ electrolyte	$La_{0.7}Sr_{0.3}MO_{3-\delta}$ (M = Mn, Fe, Co), solid-phase synthesis, h = 0.4 – 0.8 μm	U = 10 – 70 V, τ = 1 min, T_s = 750 °C	Optimal LSF cathode (0.8 μm), 13 μm thickness	188
Pt and Ni metal grids (cathode and anode current collectors)	$La_{0.8}Sr_{0.2}MnO_{3-\delta}$ (LSM82), glycothermal synthesis, S_{BET} = 2.65 $m^2\ g^{-1}$; NiO – 8YSZ (Tosoh), S_{BET} = 8.74 $m^2\ g^{-1}$	U = 15 V, τ = 1 min	Resistance of electrodes at 800 °C /Ω cm^{-2}, uncoated 4.14, coated 2.36	189
8YSZ electrolyte	LSM82, LSM82 – 8YSZ, Pechini method, S_{BET} = 15 $m^2\ g^{-1}$	U = 15 V, τ = 1 h, T_s = 1000 °C	LSM cathodes (6 – 15 μm), LSM/LSM – YSZ cathodes (9 – 21 μm in a bilayer cathode: LSM – YSZ layer, 1 – 8 μm; LSM layer 6 – 13 μm)	190
CGO10 electrolyte	LSCF, sol – gel method	U = 5 – 30 V, τ = 1 – 6 min, T_s = 800 °C	CNT [a]/LSCF (1 : 10) composite, 20 μm thickness at 25 V, 4 min	191
8YSZ electrolyte	Ni impregnation from a nitrate solution in 8YSZ (Daiichi Kigenso), h = 0.4 μm	U = 22 V, τ = 140 s, T_s = 1300 °C (air) + 600 °C (H_2)	50Ni – 8YSZ (30 μm) and 70Ni – 8YSZ (30 μm), bilayer: 50Ni – 8YSZ (3 – 6.9 μm)/70Ni – 8YSZ (8.7 – 14 μm)	192
Ni – 8YSZ (60 : 40) anode	NiO (Canadian INCO Metals), 8YSZ (Tosoh)	U = 40 V, τ = 1, 2, 5, 10, 20 min, T_s = 400 °C (together with 8YSZ film)	Functional layer thickness 2.5, 4.5, 6.8, 9.8 and 13.3 μm	19

[a] CNT is carbon nanotubes.

structures and oriented films of layered electrode materials). However, the number of publications dealing with EPD of electrolyte-supported electrode materials is moderate (Table 4). This is due to the difficulty of deposition of electrode materials onto an electrolyte support, which is a dense non-conductive substrate hampering the EPD. For creating a conductive substrate, the electrolyte or non-conductive substrate is coated by an additional graphite

sublayer,[190] a thin silver or gold layer[161] or polypyrrole layer.[49]

The deposition of LNC and LSNF cathode materials on a dense electrolyte —lanthanum silicate with the apatite structure coated with a carbon film — was considered by Szepanski *et al.*[158] Preliminary experiments on the deposition of LNC on steel substrates demonstrated that at a constant voltage of 395 V and deposition time of 7 to 780 s, the coating thickness varied from 50 to 200 μm. The dependences of the coating thickness and deposited mass with increase in the voltage up to 595 V were measured. Under these conditions, a rather thick (~250 μm) LSNF layer was formed in 180 s at a relatively low concentration of the suspension (3 mass %). The kinetics of current variation with time was substantially non-linear: in the beginning of the deposition, the current sharply decreased and the subsequent current decrease was minor. The time dependences of the deposit thickness and mass are also non-linear.

The optimal deposition conditions including the time and applied voltage established by conducting EPD for a model (steel) substrate were used to deposit the LNC and LSNF cathode materials onto a dense electrolyte, lanthanum silicate. After sintering at 1350 °C, the 2 to 140 μm cathode layers had a good adhesion to the electrolyte and high porosity.

Santillán *et al.*[161] reported the results of formation of the porous LSCF cathode layer on the surface of the dense CGO10 electrolyte substrate. The conductivity of this substrate was increased by spraying gold or silver onto its surface. The EPD process was elaborated by conducting a series of experiments on the deposition of LSCF layers on stainless steel plates. After elaboration and optimization of the conditions, further deposition was conducted onto a metallized surface of the CGO10 substrates. The porosity of the cathode layer was adjusted by adding 0.1 mass % – 0.52 mass % of starch or up to 0.2 mass % of graphite (pore-forming agent), which burned out during the subsequent oxidative annealing and sintering. The authors demonstrated that a higher deposition rate was attained at a voltage of 30 V; however, the quality of the coating was deteriorated at low (10 V) or high (30 V) voltages. It was also noted that with increasing deposition time, the coatings became thicker and their porosity increased; the latter finding was attributed to hydrogen evolution during EPD. In the first 100 s of deposition, the growth rate of the coating thickness reached saturation and, after that, the growth rate decreased. The increase in the voltage to 30 V led to higher non-uniformity of the coatings; therefore, the authors found that the optimal deposition voltage is 20 V and the optimal deposition time is 120 s.

Asamoto *et al.*[188] analyzed the influence of the microstructure of $La_{0.7}Sr_{0.3}MO_{3-\delta}$-based cathodes (M = Mn, Fe, Co) produced by painting and EPD on the electrochemical characteristics of SOFCs with the proton-conducting $SrCe_{0.95}Yb_{0.05}O_3$ electrolyte. On the basis of studies of the cathodic overpotentials, the authors identified the optimal cathode material in terms of composition ($La_{0.7}Sr_{0.3}FeO_{3-\delta}$), degree of dispersion (average particle diameter 0.8 μm) and the deposition technique (EPD). The cathode layers of this material of different thicknesses (4.5 – 31 μm) were tested in SOFC operation. The highest power density of the cell at 500 °C (0.5 W cm^{-2}) was obtained for cathode layer thickness of 13 μm.

Krkljuš *et al.*[153] fabricated porous LMO electrode for planar and tubular SOFCs on stainless-steel plates and molybdenum carbide tubes coated by a conductive graphite layer. Itagaki *et al.*[189] deposited anode (Ni – YSZ) and cathode (LSM) materials on metal wire grids, which were used as current collectors for the manufacture of SOFCs.

Itagaki *et al.*[190] performed electrophoretic deposition of single-layer (LSM) and bilayer (LSM/LSM – 8YSZ) cathodes onto a dense 8YSZ electrolyte substrate. The characteristics of the electrodes were tested in a three-electrode cell. It was shown that at 600 °C, an increase in the thickness of single-layer electrodes from 6 to 15 μm resulted in decreasing both ohmic (from 3.96 to 1.47 Ω cm^{-2}) and polarization resistances (from 25.5 to 13.3 Ω cm^{-2}). A similar trend was observed for bilayer cathodes. The minimum polarization resistance (1.13 Ω cm^{-2}) was obtained for the bilayer cathode with a thickness of 21 μm, with the LSM layer thickness being 8 μm. The ratio of layer thicknesses for the bilayer cathode was optimized. As the thickness of the first layer increased to 10 μm and the thickness of the second layer decreased to 4 μm, the polarization resistance of the LSM/LSM – 8YSZ cathode at 600 °C decreased to 0.55 Ω cm^{-2}.

Santillan *et al.*[191] demonstrated the applicability of EPD for co-deposition of carbon nanotubes with a length of 200 μm and a diameter of 15 nm and particles of the LSCF cathode material to obtain a porous cathode layer on the dense CGO10 electrolyte. According to the results, there exists a narrow voltage range (20 – 25 V) in which a continuous coating is formed. The non-uniformity of the coating formed at > 25 V was attributed to high H^+ concentration near the electrode, while that at < 20 V was attributed to the possible influence of low mobility of the deposited particles, which are represented by aggregates of carbon nanotubes bearing adsorbed LSCF particles.

A number of studies address the EPD of cathode materials with the Ruddlesden – Popper structure.[49, 187] These materials are known to have a layered structure and be characterized by anisotropy of properties such as oxygen diffusion and conductivity.[236] Matsuda *et al.*[49] investigated the possibility to prepare oriented films of layered lanthanum nickelate (LN) by EPD in a magnetic field on the CGO10 substrate coated by a conductive polypyrrole layer. For improving the adhesion and adjusting the porosity, 11 mass % – 33 mass % of starch was added to the electrode paste. The electrode structure was ordered by applying a 12 T magnetic field. The tests carried out for two single CGO10 electrolyte-supported SOFCs with LN cathodes oriented in different ways (predominantly oriented in the *ab* plane and randomly oriented) and a Pt anode showed that the cell power density is higher in the case of oriented cathode (9 and 7 mW cm^{-2} at 500 °C, respectively). In addition, it was shown by current interruption technique that the electrode polarization losses are lower for the cell with the oriented cathode (100 and 300 mV for a current density of 15 mA cm^{-2}, respectively).

Several publications consider the formation of SOFC anodes. A study of Zarabian *et al.*[48] is devoted to the EPD production of functionally graded NiO – 8YSZ anodes. The suspensions were prepared using a mixture of YSZ (d = 200 nm) and NiO (d = 1.0 μm) powders. The conditions of deposition were selected in the following range: U = 50 – 300 V, τ = 30 – 420 s. According to experimental data, the thickness of coatings increased in proportion to

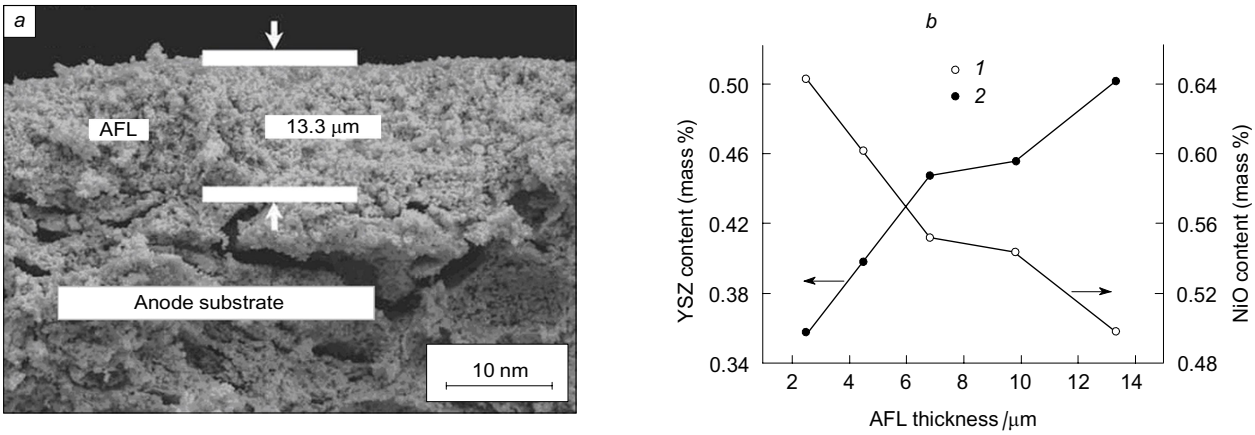


Figure 12. SEM image of the microstructure of the NiO – 8YSZ anode functional layer (AFL) electrophoretically deposited on the conductive Ni – 8YSZ substrate (U = 40 V, τ = 20 min) (*a*) and contents of NiO (*1*) and 8YSZ (*2*) in the deposit *vs.* AFL thickness (*b*).[194]

$\tau^{1/2}$. For the fabrication of a functionally graded coating, the deposition voltage was varied: in the initial period, U = 300 V was used and then this value was decreased down to 150 V over three steps, each lasting for 20 s. In the authors' opinion, larger particles (NiO) are deposited in the first stage (when the voltage is high). Finally, the coating consisted of three layers with different NiO concentrations:

Layer No.	1	2	3
C_{NiO} (mass %)	46	42	32

Itagaki *et al.*[192] investigated the EPD process to form single-layer and bilayer anodes on the graphite-modified 8YSZ electrolyte substrate. The best anodic overpotential characteristics were obtained for bilayer electrodes 50 mass % Ni – 50 mass % 8YSZ/70 mass % Ni – 30 mass % 8YSZ with 3 : 14 ratio of layer thicknesses. For the SOFCs with single-layer anodes 50 mass % Ni – 50 mass % 8YSZ and 70 mass % Ni – 30 mass % 8YSZ and the bilayer anode 50 mass % Ni – 50 mass % 8YSZ/70 mass % Ni – 30 mass % 8YSZ, the power densities at 700 °C were 30, 40 and 120 mW cm^{-2}, respectively. Wang *et al.*[194] reported high power densities for a single SOFC with a traditional 8YSZ electrolyte (up to 1.2 W cm^{-2} at 800 °C) by fabricating a functionally graded anode layer by electrophoretic deposition from suspensions of NiO and 8YSZ particles on the Ni – 8YSZ collector layers. The obtained coating was characterized by different ratios of the NiO and YSZ contents, depending on the deposition time and, hence, on the deposit thickness; this result was explained by the effect of the particle size of the initial materials on the electrophoretic mobility (Fig. 12).

4.4. Microtubular SOFC

Lately, researchers' attention has been drawn to microtubular solid oxide fuel cells, as they show better thermal cycling stability and durability in comparison with traditional SOFCs, in particular, the start of μ-SOFCs is faster (heating rate $\geqslant$ 200 °C h^{-1}) [237] and their power density is higher.[238] In order to reduce the operating temperature, like for full-size SOFCs, the attention has recently been focused on the designs of μ-SOFCs with a thin-film electrolyte formed on the anode or cathode.[239 – 244] The EPD process is widely used to fabricate μ-SOFCs, including the complete formation of the whole cell with co-sintering of the successively deposited functional layers (Table 5).

Actually, manufacturing of the support is the most important stage, since this largely determines the performance of μ-SOFC. The most popular widely used methods for the formation of the supporting substrate include extrusion, gel moulding, isostatic pressing and phase inversion.[249] Suzuki *et al.*[250] showed that using only microstructural modification of the NiO – CGO supporting anode prepared by extrusion of the anode paste with or without a pore-forming agent (polymethyl methacrylate), it is possible to increase the power density of a cell with a thin-film CGO electrolyte from 0.875 to 1.017 W cm^{-2} at 550 °C. A power density of 0.300 W cm^{-2} at 800 °C was found for μ-SOFC supported by the LSM cathode fabricated by extrusion followed by formation of CGO10 and SSZ10 electrolyte layers by dip coating.[251]

Electrophoresis can be used to form separate μ-SOFC layers and the cell as a whole. Droushiotis *et al.*[245] studied the possibility to use an EPD of ethyl alcohol-based suspension to manufacture a 8YSZ electrolyte film on a hollow-fibre NiO – 8YSZ anode with asymmetric porosity formed by phase inversion. The power density of μ-SOFCs with the thin-film 8YSZ electrolyte on a novel design anode at 800 °C was somewhat lower (0.20 W cm^{-2}) than the power density of the cell formed by EPD alone (0.364 cm^{-2}).[208] The authors attributed this result to leakage through the electrolyte film, which could not be sintered to a gas-tight state even at 1500 °C.

In some studies, the fabrication of μ-SOFC by EPD was performed using a graphite rod as a conductive substrate, on which either half-cell or the whole cell was formed layer-by-layer. Yu and Lee [117, 118, 246] reported a series of works on the fabrication of bilayer anode-supported μ-SOFCs with different thin-film electrolytes [8YSZ, $La_{0.8}Sr_{0.2}Ga_{0.8}Mg_{0.2}O_{3-\delta}$ (LSGM) and CGO10] by constant-current EPD from suspensions in ethyl alcohol. During deposition of different cell layers, the voltage was varied from 10 to 50 V and the deposition time varied from 5 to 50 s. The authors showed that using EPD, the half-cell structure (without cathode) can be completely formed in a few minutes; the porosity of the layers can be controlled by adding various components and a pore-forming agent to a suspension; all layers can be sintered together (Fig. 13). The

Table 5. Materials and conditions of formation of functional layers of μ-SOFC by EPD (other methods are inducated) and cell characteristics.

Functional layers (composition, thickness, deposition and sintering conditions)			OCV (see [a]); fuel/oxidant	Power /W cm^{-2} (see [b])	Ref.
electrolyte	cathode	anode			
8YSZ, h = 10 μm, I = 100 mA cm^{-2}, T_s = 1250 °C	LSM, h = 80 μm, I = 50 mA cm^{-2} LSM – 8YSZ 70 : 30, 50 : 50	*NiO – 8YSZ, h = 240 μm, I = 100 mA cm^{-2}	~1.0 V; (N_2 + 20% H_2)/air	0.516 (800 °C), 0.604 (800 °C), 0.635 (800 °C)	39
LSGM ($La_{0.8}Sr_{0.2}Ga_{0.8}Mg_{0.2}O_{3-\delta}$), h = 17.5 μm, I = 20 mA, U = 20 V, τ = 20 s, T_s = 1300 °C	BL: SFM ($Sr_2Fe_{1.5}Mo_{0.5}O_{6-\delta}$), h = 5.8 μm, U = 20 V, τ = 5 s FL: SFM – CGO10 + PMMA, h = 16.3 μm, U = 20 V, τ = 20 s	BL: SFM, h = 5.8 μm, U = 20 V, τ = 5 s *SFM – CGO10 + PMMA, h = 127 μm, U = 40 V, τ = 60 s	~0.95 V; (H_2 + 3% H_2O)/air	0.116 (600 °C)	40
LSGM, h = 17.5 μm, I = 20 mA, U = 20 V, τ = 20 s, T_s = 1300 °C	SFM – LSGM + PMMA, h = 47.5 μm, U = 20 V, τ = 20 s	*SFM – LSGM + PMMA, h = 126 μm, U = 20 V, τ = 60 s	~0.58 V; (H_2 + 3% H_2O)/air	0.080 (600 °C)	40
LSGM, h = 15.3 μm, I = 20 mA, U = 20 V, τ = 20 s, T_s = 1400 °C	$La_{0.6}Ca_{0.3}Cr_{0.8}Mn_{0.2}O_{3-\delta}$ (LCCM), LCCM – 8YSZ, h = 22.2 μm, U = 20 V, τ = 20 s	*LCCM – 8YSZ + PMMA, h = 132 μm, U = 20 V, τ = 60 s	~1.1 V; (H_2 + 3% H_2O)/air	0.141 (600 °C)	41
8YSZ, h = 6.7 μm, I = 20 mA, U = 30 V, τ = 45 s, T_s = 1400 °C	BL: $Ce_{0.6}La_{0.4}O_{2-\delta}$, h = 6 μm, FL: LSCF – CGO10 (50 : 50), h = 22 μm, painting, T_s = 1100 °C	*CC: NiO – 8YSZ (60 : 40) + PMMA, h = 85 μm, U = 20 V, τ = 50 s FL: NiO – 8YSZ (60 : 40), h = 7.5 μm, U = 50 V, τ = 30 s	1.1 V (750 °C), 1.12 V (700 °C); (H_2 + 3% H_2O)/air	0.30 (750 °C), 0.20 (750 °C)	117
CGO10, h = 10 μm, I = 20 mA, U = 30 V, τ = 45 s, T_s = 1500 °C	LSCF – CGO10 (50 : 50), h = 37 μm, painting, T_s = 1100 °C	*CC: NiO – CGO10 (60 : 40) + PMMA, h = 110 μm, U = 50 V, τ = 40 s FL: NiO – CGO10 (60 : 40), h = 9 μm, U = 40 V, τ = 30 s	0.60 V (700 °C), 0.67 V (650 °C), 0.70 V (600 °C); H_2 + 3% H_2O/air	0.26 (700 °C), 0.37 (650 °C), 0.42 (600 °C)	118
8YSZ, h = 35 μm, I = 10 mA cm^{-2}, T_s = 1250 °C	LSM82, I = 5 mA cm^{-2}	*NiO – 8YSZ (70 : 30), h = 240 μm, I = 2 mA cm^{-2}	~1.0 V; (N_2 + 20% H_2)/air	0.364 (800 °C), 0.275 (700 °C), 0.160 (600 °C)	208
8YSZ, h = 40 μm, U = 110 V, τ = 2.5 min, T_s = 1500 °C (under hydrogen)	FL: LSM – 8YSZ (50 : 50) CC: LSM, painting, T_s = 1200 °C	*NiO – 8YSZ (60 : 40), h = 240 μm, supporting, hollow fibre, phase inversion	~0.90 V (800 °C); (H_2 + 3% H_2O)/air	0.20 (800 °C), 0.18 (750 °C), 0.14 (700 °C)	245
LSGM, h = 18 μm, I = 20 À U = 20 V, τ = 60 s, T_s = 1450 °C/air	LSCF – CGO10 (50 : 50), h = 36 μm, painting, T_s = 1100 °C	*CC: NiO – CGO10 (60 : 40) + PMMA, h = 100 μm, U = 60 V, τ = 50 s FL: NiO – CGO10 (60 : 40), h = 9 μm, U = 20 V, τ = 20 s BL: $Ce_{0.6}La_{0.4}O_{2-\delta}$, h = 5 μm, U = 20 V, τ = 20 s	0.92 V (800 °C), 1.05 V (500 °C); (H_2 + 3% H_2O)/air	0.51 (800 °C), 0.27 (500 °C)	246

Table 5 (continued).

Functional layers (composition, thickness, deposition and sintering conditions)			OCV (see [a]); fuel/oxidant	Power /W cm^{-2} (see [b])	Ref.
electrolyte	cathode	anode			
8YSZ, h = 10.4 μm, I = 20 mA, U = 10 V, τ = 10 s, T_s = 1400 °C	8YSZ, U = 8 V, τ = 8 s, T_s = 1400 °C + impregnation of La, Sr, Co nitrates, T_s = 950 °C	8YSZ, U = 20 V, τ = 60 s, T_s = 1400 °C + impregnation of Ni nitrate, T_s = 800 °C	0.90 V (800 °C), 0.93 V (700 °C), 0.95 V (600 °C); H_2 + 3% H_2O/air	0.071 (800 °C), 0.067 (700 °C), 0.059 (600 °C)	247
8YSZ, h = 6 μm, (deposition conditions are not reported), T_s = 1380 °C, 8YSZ	LSM82, h = 15 – 20 μm, painting, T_s = 1150 °C FL: LSM – 8YSZ (50 : 50), h = 10 μm, CC: LSM, h = 15 – 20 μm, T_s = 1150 °C $Sm_{0.6}Sr_{0.4}CoO_{3-\delta}$, T_s = 1150 °C	*CC: NiO (h = 0.65 μm) – 8YSZ (55 : 45) (h = 250 μm) FL: NiO (h = 0.3 μm) – 8YSZ (55 : 45) (h = 10 μm)	~1.05 V; He + 30% H_2/air ~1.1 V; H_2 + 3% H_2O/air	0.190 (800 °C), 0.160 (750 °C), 0.136 (700 °C) 0.530 (800 °C), 0.742 (650 °C)	248

Notes. The supporting electrode of μ-SOFC with thin-film electrolyte is marked by *; BL is buffer layer, FL is functional layer, CC is current collector.

[a] The value in parentheses is the temperature of OCV measurements.

[b] The value in parentheses is the temperature of power measurements.

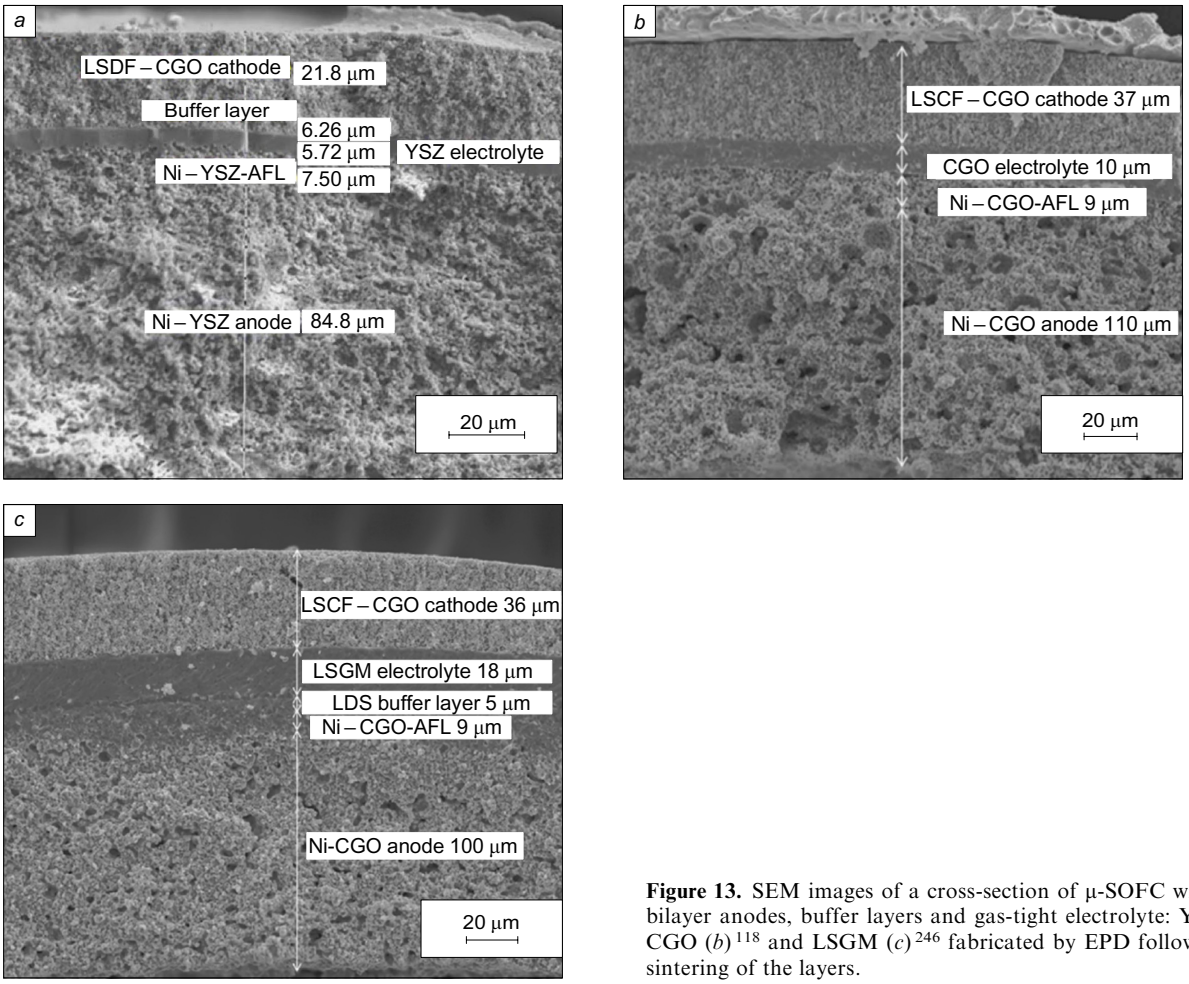


Figure 13. SEM images of a cross-section of μ-SOFC with porous bilayer anodes, buffer layers and gas-tight electrolyte: YSZ (*a*),[117] CGO (*b*)[118] and LSGM (*c*)[246] fabricated by EPD followed by co-sintering of the layers.

best power density (0.270 W cm^{-2} at 600 °C) was obtained for the cell with the LGSM electrolyte (h = 18 μm). For the cell with the 8YSZ electrolyte of a smaller thickness (h = 6.7 μm), the same power density was attained only at 750 °C. According to a study of symmetric μ-SOFC with an LGSM electrolyte,[40,41] by using bilayer electrodes consisting of the thin SFM buffer layer and the SFM – CGO10 composite layers, one can reach the highest OCV and power density values of the cell. Although the power densities of μ-SOFCs with the LGSM electrolyte and oxide anodes (0.080 – 0.141 W cm^{-2} at 600 °C)[40,41] were lower than those for SOFCs with traditional nickel cermet (0.270 W cm^{-2} at 500 °C),[246] this line of research holds good prospects, because the use of oxide anodes considerably increases the thermal cycling stability of the cell.[252,253]

Lee and Lee[247] elucidated the possibility of formation of symmetric μ-SOFCs with electrodes fabricated by impregnation of Ni and LSC into ceramic 8YSZ templates, which were formed by EPD. The highest power density values found for this cell were moderate (59, 67 and 71 mW cm^{-2} at 600, 700 and 800 °C, respectively); however, no significant degradation of characteristics took place even after 50 thermal cycles.

In some studies, the effect of cathode composition on the performance of μ-SOFC with the 8YSZ electrolyte were demonstrated. For example, the replacement of LSM cathode by LSM-based composite cathodes markedly increases the power density of the cell (from 0.19 to 0.53 W cm^{-2} at 800 °C);[39,248] however, a more pronounced effect is achieved when electrochemically active cathodes with mixed conductivity, *e.g.*, based on cobaltites, are used (0.742 W cm^{-2} at 650 °C).[248]

Cherng *et al.*[53,208] presented a series of works on anode-supported μ-SOFCs, with the anode being formed by EPD from aqueous suspensions. The deposition was carried out on a thin copper wire of 100 – 150 μm diameter. The authors investigated the effect of concentration of the ammonium polyacrylate additive (PAA – NH_4) in aqueous suspensions based on LSM, 8YSZ, NiO, NiO – 8YSZ and NiO – 3YSZ on a number of parameters such as the ζ-potential, the deposition rate and the porosity of the layers sintered at 1250 °C.

While adjusting the content of the additive and the deposition parameters in preliminary experiments, the authors carried out co-sintering of all μ-SOFC layers and obtained a dense 8YSZ layer (35 μm) and porous anode (32% porosity) and cathode (42% porosity); this resulted in a relatively high power density for the cell: 0.364 W cm^{-2} at 800 °C.

4.5. Protective coatings for current collectors

The internal electrical connections of SOFCs (interconnects and current collectors) — so-called BOP (balance-of-plant) elements — are key components ensuring long-term stable battery performance. Today the main BOP materials are ferrite stainless steels (Crofer 22 APU, AISI 441, AISI 430

and so on) owing to their high thermal stability, compatibility with other SOFC components in the coefficient of linear thermal expansion (CTE), ready availability and low cost. The problem associated with the use of chromium steels is evaporation of chromium oxides during SOFC operation, resulting in the formation of low-conductive oxides on the surface, which poison perovskite cathodes and thus reduce the efficiency of SOFC operation.[254] This problem can be mitigated by creating coatings that would protect the BOP components in a humid oxidative atmosphere in the temperature range of 700–900 °C: these coatings eliminate or suppress the growth of Cr_2O_3 on the surface of steel interconnects, eliminate evaporation of CrO_3 and $CrO_2(OH)_2$ and provide the minimum value for the area specific resistance (ASR), the commonly accepted upper limit of which is 0.1 Ω cm^2 throughout the whole time of operation of SOFCs.[255]

Among the most widely used protective coatings, mention should be made of conducting spinels,[256–261] materials with the perovskite structure[262–266] and composites based on them,[267] and oxides of chemically reactive elements (yttrium, lanthanum, cerium, neodymium, hafnium and so on).[268–270] The high sintering temperature of protective coatings based on these materials complicates the production of dense films by usual ceramic technologies such as screen printing or slurry dip coating. Therefore, these coatings are mainly applied by physical and chemical methods: vapour phase deposition, magnetron and plasma sputtering, pulsed laser deposition, the sol–gel method and electrodeposition.[255] In this case, the benefits of EPD include the formation of dense coatings with good adhesion to the base material, rapid deposition, low cost and the possibility to form coatings with controlled thickness and microstructure on surfaces of various shapes.

The greatest number of publications dealing with protective coatings formed by EPD are devoted to spinels co-deposited on Crofer 22 APU. Iron-containing spinels have CTE of $\sim 11 \times 10^{-6}$ K^{-1} in the temperature range of 25–800 °C, which is close to the CTE for steels they are coated on (Crofer 22 APU: CTE $\sim 11 \times 10^{-6}$ K^{-1} in the same temperature range). The CTE values for Cr-containing spinels are $7.2-7.6 \times 10^{-6}$ K^{-1}. The $(Cu,Mn)_3O_4$ and $(Mn,Co)_3O_4$ spinels showed abnormal thermal expansion, but also the highest conductivity (for $MnCo_2O_4$, 60 S cm^{-1} at 800 °C; and for $Cu_{1.3}Mn_{1.7}O_4$, 225 S cm^{-1} at 750 °C); in addition, copper can intensify sintering of the coating.[271] The conditions for the formation of protective coatings by EPD and the electrical properties and degradation characteristics of the coatings are presented in Table 6.

Zhang *et al.*[42] carried out a systematic study of the influence of EPD regimes and heat treatment conditions on the microstructure, electrical properties and long-term stability of the $(Mn,Co)_3O_4$ coatings. It was shown that the chemical composition of the spinel (cobalt to manganese ratio) depends on the conditions of both the deposition and the heat treatment of the resulting coating (Fig. 14 *a*) and considerably influences the polarization characteristics of the coatings. The lowest polarization resistance (17 mΩ cm^2 at 800 °C) was found for the coating with 1 : 1 ratio of cations deposited at 400 V and then annealed in a humid hydrogen atmosphere (Fig. 14 *b*). Generally, coatings sintered in air had high polarization resistance; the rate of their degradation was > 500% over 500 h (due to the diffusion of chromium atoms through the coating).

It was shown[197] that after heat treatment under argon, the electrophoretically deposited $Mn_{1.5}Co_{1.5}O_4$ coatings were denser than those sintered in air; however, they contained spinel decomposition products (cobalt and manganese oxides). Polarization resistance and the rate of degradation for a coating sintered in air at 1000 °C were 20 and 0.56 mΩ cm^2, respectively, over 1000 h. The testing that lasted 5000 h demonstrated lower degradation of the EPD coatings compared with those obtained by thermal evaporation and sputtering.[275] Note that these coatings had higher chemical stability against high-temperature SiO_2-based glasses, while the coatings obtained by electrodeposition and slurry coating degraded within 500 h due to the interaction with glasses.[197] A study[46] on the co-deposition of $Mn_{1.5}Co_{1.5}O_4$ and CuO did not reveal a significant effect of copper on the polarization characteristics of the coatings. The polarization resistance of all of the tested coatings sharply decreased upon long-term heat treatment at 800 °C to reach ~10 mΩ cm^2 after 1000 h of testing.

Talic *et al.*[45] reported comparative studies of the $MnCo_2O_4$, $MnCo_{1.7}Cu_{0.3}O_4$ and $MnCo_{1.7}Fe_{0.3}O_4$ coatings obtained by EPD from suspensions in a mixture of isopropyl and ethyl alcohols (50 : 50). The deposition time was 40 to 100 s and the applied voltage was 35 V; the sintering of the coatings was carried out at 900 °C in an N_2 + 9% H_2 atmosphere with subsequent oxidative annealing in air at 800 °C. Ageing of the coatings was studied in air for 2000 h at 800 °C and then the samples were subjected to 30 thermal cycles (800–100 °C) and tested for the subsequent 2000 h. The polarization resistance at 800 °C for the reference samples — uncoated Crofer 22 APU steel (53 mΩ cm^2) and LSM (27 mΩ cm^2) — considerably exceeded the values obtained for the test samples (see Table 6). For Crofer 22 APU, the rate of deterioration of polarization characteristics (3.6 mΩ cm^2 in 1000 h) was also 3–6 times higher than that for the test samples. In this study, $MnCo_2O_4$ was recognized as the best composition in all characteristics (ASR: 15.2 mΩ cm^2; rate of ageing: +0.6 mΩ cm^2 in 1000 h).

The properties of EPD coatings based on the $(Cu,Mn)_3O_4$ spinels have been studied.[47,199,200] Despite its high conductivity (130 S cm^{-1} at 800 °C), the $Cu_{1.3}Mn_{1.7}O_4$ spinel is unstable and decomposes on heat treatment at 850 °C to give CuO and MnO on the coated surface, the authors manufactured protective EPD coatings on Crofer 22 H using the $CuMn_{1.8}O_4$ spinel with a reduced copper content (120 S cm^{-1} at 800 °C).[47] Testing of single SOFCs at a constant current density of 0.5 A cm^{-2} for 12 days at 800 °C in a contact with Crofer 22 H grids without a coating and with coatings made of commercial $CuMn_2O_4$ or $CuMn_{1.8}O_4$ spinel demonstrated the absence of cell potential degradation in the latter case due to the high absorption capacity of the deficient spinel (1 mole of $CuMn_{1.8}O_4$ is able to getter 1.83 moles of Cr_2O_3).[199]

Liu *et al.*[276] found that the electrical conductivity of the $Mn_{1.5}Co_{1.5}O_4$ spinel sharply decreases upon the reaction with Cr_2O_3 giving $Mn_{1.5-0.5x}Co_{1.5-0.5x}Cr_xO_4$ (from 60 S cm^{-1} at $x = 0$ to 0.007 S cm^{-1} at $x = 0.2$). In order to increase the conductivity of the protective coating, bilayer coatings $(Mn_{1.5}Co_{1.5})O_4/La_{0.8}Sr_{0.2}MnO_3$ (LSM) were manufactured by EPD.[277] The coatings were sintered at 1200 °C and then treated in argon. The polarization resistance of the bilayer coatings showed good stability when tested in air (62 mΩ cm^2 at 800 °C). In the tests

Table 6. Materials, conditions of formation and characteristics of protective layers of SOFC current collectors.

Protective layer	Conditions of formation [a]	Characteristics	Ref.
$(Mn,Co)_3O_4$ (see [b])	U = 200, 300, 400, 500 V, T_s = 800 °C (air) (1), T_s = 800 °C (H_2 + 3% H_2O) (2)	h = 0.56 (200), 0.59 (300), 0.68 (400), 0.81 (500) μm; ASR (1) = 24 (200), 32 (300), 40 (400), 83 (500); ASR(2) = 20 (200), 21 (300), 17 (400), 35 (500); ΔASR(1) > 500%, 500 h; ΔASR(2) > 300%, 500	42
LNF	U = 100 V, τ = 5 min, T_s = 1100 °C (air)	h = 7 μm, ASR = 4.2 ; ΔASR = + 1.2 (in 1000 h)	44
$MnCo_2O_4$ (MC), $MnCo_{1.7}Cu_{0.3}O_4$ (MCCu), $MnCo_{1.7}Fe_{0.3}O_4$ (MCFe)	U = 35 V, τ = 40 – 100 s, T_s = 900 °C (N_2 – 9% H_2) + 800 °C (air)	h = 9 – 13 μm (0.6 μm interfacial Cr_2O_3 film); ASR = 15.2 (MC), 16.7 (MCCu), 17.2 (MCFe); ΔASR = + 0.6 (MC), + 1.0 (MCCu), + 0.9 (MCFe) (in 1000 h)	45
$Mn_{1.5}Co_{1.5}O_4$	U = 50 V, τ = 5 s – 2 min, T_s = 800 – 1150 °C (air, Ar)	$h \approx$ 10 – 40 μm, ASR (1000 °C, air) = 20; ΔASR = + 0.51 (in 1000 h)	46
$CuMn_{1.8}O_4$	U = 20 V, τ = 10 min, T_s = 1000 °C (Ar – 2% H_2) + 850 °C (air)	h = 26 μm (1.2 μm interfacial Cr_2O_3 film); ASR = 8.9, ΔASR = + 12.9 (in 400 h)	47, 199, 200
$Mn_{1.5}Co_{1.5}O_4$ + 0, 5 mass % CuO	U = 50 V, τ = 20 s, T_s = 900 °C (Ar – 4% H_2) + 900 °C (air)	h = 10 – 13 μm; ASR = 48 (with copper) 50 ($Mn_{1.5}Co_{1.5}O_4$); ΔASR = − 36 ($Mn_{1.5}Co_{1.5}O_4$), − 38 (with copper)	197
$(Mn_{1.5}Co_{1.5})O_4$/LSM82	U = to 300 B, τ = 1 – 5 min, T_s = 1200 °C (Ar)	h = 5 μm/5 μm; ASR = 62; ΔASR = − 19 (in 110 h)	272
$(Mn,Co)_3O_4$	U = 50 V, τ = 60 – 240 s		273
Mn_3O_4	U = 0.75 – 2 mA cm^{-2}, τ = 5 – 30 s, T_s = 800 °C (air)	h = 3 – 5 μm (10 – 20 s), after heat treatment for 100 h (800 °C), no Cr on the surface	274
$Mn_{1.5}Co_{1.5}O_4$ (American Elements, USA)	U = 50 V s^{-1}, τ = 20 s, T_s = 1000 °C air)	h = 15 μm Mn – Co layer after heat treatment h = 1.5 μm Cr_2O_3 layer; ASR = + 22 (after 5000 h of testing); ΔASR = + 1.2 (in 1000 h)	275

[a] The atmosphere in which EPD was conducted is given in parentheses.
[b] For a given protective layer, the Table presents the ASR values (mΩ cm^2) at various voltages (numbers in parentheses); the ΔASR value (the change in the total polarization resistance throughout the operation of SOFC relative to the initial value) is given in %; the ΔASR for other protective layers is given in mΩ cm^2 over the indicated time period.

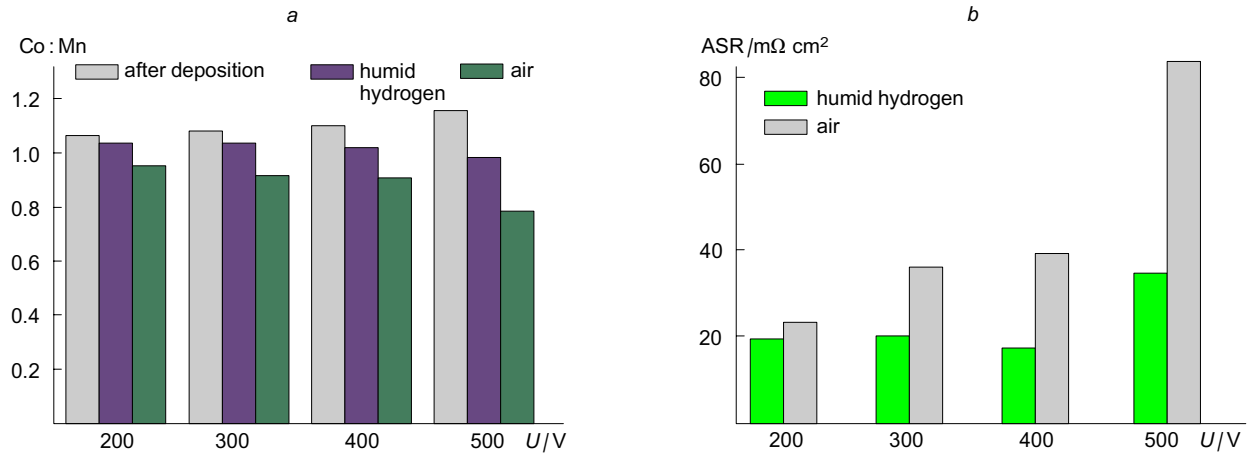


Figure 14. Diagrams reflecting the variation of the ratio of cobalt to manganese cations in the coatings based on the $(Mn,Co)_3O_4$ spinel depending on the EPD (U = 200 – 500 V) and heat treatment (*a*) conditions and the area specific resistance at 800 °C in air (*b*).[42]

under argon, the polarization resistance decreased to 42 $m\Omega\ cm^2$ in the first 110 h of testing and then remained virtually constant. The coating demonstrated a semiconductor type of conduction determined by the LSM perovskite layer.

In general, the use of perovskites with high p type conductivity for protective coatings is rather popular. Apart from the lanthanum strontium manganites, chromites, cobaltites and ferrites are also used.[255, 262 – 266, 278 – 281] Magnetron sputtering is employed most often to deposit the perovskite coatings.[255] In our opinion, EPD could also be fairly promising. Waluyo *et al.*[44] performed the EPD of protective coatings based on the LNF perovskite; they obtained a lower ASR compared to those of spinel coatings (4.2 $m\Omega\ cm^2$ at 800 °C) and an acceptable degradation rate (+1.2 $m\Omega\ cm^2$ in 1000 h).

One more promising area is surface modification of steels by deposition of thin films of nano-sized lanthanide oxides, which actively react with chromium within interconnects. This modification enhances the corrosion stability and improves the electrical properties of surfaces. For example, the deposition of La_2O_3 or Y_2O_3 decreased the ASR values for Crofer 22 APU to 0.180 or 0.160 $\Omega\ cm^2$, respectively.[282] This method is implemented, most often, by vapour phase epitaxy using organometallic compounds. It was noted[255, 278] that the coatings are usually very thin (< 0.2 μm) and porous and do not ensure full protection from the diffusion of chromium from steel to the surface of lanthanide oxides and, hence, they do not prevent evaporation of volatile chromium oxides from the surface and the subsequent cathode poisoning. The use of EPD could not only provide a simpler and cheaper deposition of protective coatings of this type but also increase the density and adhesive properties of the coatings. This area of EPD application has not yet been developed, but it may become useful in the near future.

5. Conclusion

This review presents the results of experimental and theoretical studies related to application of the EPD method for the formation of functional parts of SOFCs. The trends of development of theoretical models are considered on different spatial scales, ranging from phenomenological models describing macroscopic transfer of continuous media to models describing processes at the microscopic level, explicitly taking into account the concerted motion and interactions of particles with one another and with electrodes and changes in the EDL, ion distribution and the effect of the liquid flow. The advanced models adequately describe some aspects of the effects involved. For example, Sarkar's phenomenological model allows one to follow the effect of the change in the suspension concentration on the deposition kinetics, while numerical models of particle dynamics elucidate the effect of deposition conditions on the deposit. Theoretical analysis of published studies revealed the specific features of EPD within porous structures. Integrated simulation of the processes involved in the EPD is required. This will expand the scope of application of theoretical models under real experimental conditions where significant contributions are made by non-stationary effects and spatial changes in both macroscopic parameters and processes at the micro level (changes in the EDL, particle interactions with one another and with the deposit). The development of studies along this line would make it possible to integrate the existing array of experimental data, including the data on kinetics, transfer processes, mechanism of deposition, the structure and density of the resulting coatings under given experimental conditions. Therefore, further development of experimental studies and EPD simulation methods appears relevant.

Considering the experimental studies dealing with the application of EPD in SOFC technology, the following key problems faced by researchers may be indicated:

— for ensuring the stability of suspensions and adhesion of the coatings, the use of organic dispersants, charge agents and binders is often required, which affects the quality of coatings;

— the production of crack-free sintered films with 5 – 10 μm thickness in one cycle is difficult; it is necessary to use multiple EPD cycles to heal pores and defects;

— development and adaptation of the EPD technique for the formation of the supporting parts of SOFCs, for example, electrodes with controlled porosity and formation of electrode bodies;

— for the EPD onto non-conductive anode substrates, it is necessary to ensure open porosity of the sintered material or carry out deposition on a green material with a graphite filler to generate the conductivity of the substrate; the deposition onto graphite or another conductive sublayer does not always ensure the required adhesion of the coatings; therefore, a relevant task is the search for new technological solutions related to deposition onto non-conductive anode substrates;

— it is necessary to elaborate the materials science aspect of the design of SOFCs: development of new cathode materials with low sinterability in combination with good electrochemical properties;

— an interesting issue is deposition of conductive materials, *e.g.*, electrode materials, on the substrate surface and taking account of nonlinear effects;

— a promising method is the EPD fabrication of the full structure of microtubular cells over a short period of time with co-sintering of the deposits;

— development of the EPD method for the design of protective coatings for SOFC interconnects based on highly conductive spinels, perovskite materials and films of the oxides of reactive elements, production of composite and multilayer protective coatings.

The review was written within the state assignment of the Institute of Electrophysics, Ural Branch of the Russian Academy of Sciences, and the Development of SOFC Technology research subject of the Institute of High Temperature Electrochemistry, Ural Branch of the Russian Academy of Sciences. The authors are grateful to the Russian Federation Government for the support of the study (Contract No. 02.A03.21.0006, Act 211).

Figures 1 – 4 were drawn by the authors and are based on publications that are indicated in the Figure captions. Figure 5 *b* was taken from the publicly available web page https://www.mtm.kuleuven.be/Onderzoek/Ceramics/old-info/EPD, reference is given. Figure 7 was taken from the open access online journal (INTECH Open Science), reference is given. The data for Fig. 11 *a*, 13 (*a* – *c*) were taken from open access journals; references are given. Figures 5 *a*, 6, 10, 11 *b*, 12 and 14 are courtesy of Elsevier, Figure 8 is courtesy of Wiley, Figure 9 *a* – *d* is courtesy of Springer Nature.

References

1. A.F.Ghoniem. *Prog. Energy Combust. Sci.*, **37**, 15 (2011)
2. L.Proskuryakova, S.Filippov. *Energy Proc.*, **75**, 2798 (2015)
3. J.Kartite, M.Cherkaoui. *Energy Proc.*, **157**, 232 (2019)
4. C.Haynes. *J. Power Sources*, **92**, 199 (2001)
5. L.Giorgi, F.Leccese. *Open Fuel Cells J.*, **6**, 1 (2013)
6. P.Connor. *Solid Oxide Fuels Cells: Facts and Figures*. (Ed. P.Connor). (London: Springer, 2013). P. 229
7. A.Choudhury, H.Chandra, A.Arora. *Renew. Sust. Energy Rev.*, **20**, 430 (2013)
8. Z.Gao, L.V.Mogni, E.C.Miller, J.G.Railsback, S.A.Barnett. *Energy Environ. Sci.*, **9**, 1602 (2016)
9. S.J.Cooper, N.P.Brandon. In *Solid Oxide Fuel Cell Lifetime and Reliability. Critical Challenges in Fuel Cells*. (Eds N.P.Brandon, E.Ruiz-Trejo, P.Boldrin). (London: Academic Press, Elsevier, 2017). P. 234
10. F.Ramadhani, M.A.Hussain, H.Mokhlis, S.Hajimolana. *Renew. Sust. Energy Rev.*, **76**, 460 (2017)
11. B.Singh, S.Ghosh, S.Aich, B.Roy. *J. Power Sources*, **339**, 103 (2017)
12. L.S.Mahmud, A.Muchtar, M.R.Somalu. *Renew. Sust. Energy Rev.*, **72**, 105 (2017)
13. B.Timurkutluk, C.Timurkutluk, M.D.Mat, Y.Kaplan. *Renew. Sust. Energy Rev.*, **56**, 1101 (2016)
14. N.Kochetova, I.Animitsa, D.Medvedev, A.Demin, P.Tsiakaras. *RSC Adv.*, **6**, 73222 (2016)
15. R.Pelosato, G.Cordano, D.Stucchi, C.Cristiani, G.Dotelli. *J. Power Sources*, **298**, 46 (2015)
16. S.Ya.Istomin, E.V.Antipov. *Russ. Chem. Rev.*, **82**, 686 (2013)
17. P.S.S.Shaikh, A.Muchtar, M.R.Somalu. *Renew. Sust. Energy Rev.*, **51**, 1 (2015)
18. A.Sinha, D.N.Miller, J.T.S.Irvine. *J. Mater. Chem. A*, **4**, 1111 (2016)
19. J.Wu, X.Liu. *J. Mater. Sci. Technol.*, **26**, 293 (2010)
20. M.E.Chelmehsara, J.Mahmoudimehr. *Int. J. Hydrogen Energy*, **43**, 15521 (2018)
21. J.Will, A.Mitterdorfer, C.Kleinlogel, D.Perednis, L.J.Gauckler. *Solid State Ionics*, **131**, 79 (2000)
22. L.A.Dunyushkina. in *Vvedenie v Metody Polucheniya Plenochnykh Elektrolitov dlya Tverdooksidnykh Toplivnykh Elementov*. (Introduction to Methods for Producing Film Electrolytes for Solid Oxide Fuel Cells). (Ekaterinburg: Ural Branch of RSA, 2015). P. 126
23. J.W.Kim, D.Y.Jang, M.Kim, H.J.Choi, J.H.Shim. *J. Power Sources*, **301**, 72 (2016)
24. J.Quan, Z.Zhu, G.Jiang, W.Liu. *J. Power Sources*, **246**, 556 (2014)
25. D.Chen, C.Chen, Y.Gao, Z.Chang, Z.Shao, F.Ciucci. *J. Power Sources*, **295**, 117 (2015)
26. D.Virbukas, M.Sriubas, G.Laukaitis. *Solid State Ionics*, **302**, 107 (2017)
27. P.Arunkumar, U.Aarthi, M.Sribalaji, B.Mukherjee, A.K.Keshri, W.H.Tanveer, S.W.Cha, K.S.Babu. *J. Alloys Compd.*, **765**, 418 (2018)
28. Y.X.Liu, S.F.Wang, Y.F.Hsu, C.H.Wang. *J. Power Sources*, **381**, 101 (2018)
29. J.Fondard, A.Billard, G.Bertrand, P.Briois. *Vacuum*, **152**, 97 (2018)
30. S.H.Lee, S.P.Woo, N.Kakati, D.-J. Kim, Y.S.Yoon. *Energies*, **11**, 3122 (2018)
31. L.Besra, M.Liu. *Prog. Mater. Sci.*, **52**, 1 (2007)
32. I.Corni, M.P.Ryan, A.R.Boccaccini. *J. Eur. Ceram. Soc.*, **28**, 1353 (2008)
33. Z.Xu, G.Rajaram, J.Sankar, D.Pai. *Fuel Cells Bull.*, 12 (2007)
34. S.Chauoon, M.Meepho, N.Chuankrerkkul, S.Chaianansutcharit, R.Pornprasertsuk. *Thin Solid Films*, **660**, 741 (2018)
35. S.M.Majhi, S.K.Behura, S.Bhattacharjee, B.P.Singh, T.K.Chogdar, N.M.Gokhale, L.Besra. *Int. J. Hydrogen Energy*, **36**, 14930 (2011)
36. S.T.Aruna, K.S.Rajam. *Mater. Chem. Phys.*, **111**, 131 (2008)
37. D.Das, B.Bagchi, R.N.Basu. *J. Alloys Compd.*, **693**, 1220 (2017)
38. I.Aznam, J.C.W.Mah, A.Muchtar, M.R.Samalu, M.J.Ghazali. *Zhejiang Univ.-Sci. A: Appl. Phys. Eng.*, **19**, 811 (2018)
39. F.A.Yu, C.C.Wu, T.H.Yeh, J.S.Cherng. *Int. J. Hydrogen Energy*, **40**, 14072 (2015)
40. S.H.Lee, K.T.Lee. *J. Ceram. Proc. Res.*, **18**, 580 (2017)
41. S.H.Lee, K.T.Lee. *J. Ceram. Proc. Res.*, **18**, 854 (2017)
42. H.Zhang, Z.Zhan, X.Liu. *J. Power Sources*, **196**, 8041 (2011)
43. M.Mirzaei, A.Simchi, M.A.Faghihi Sani, A.Yazdanyar. *Ceram. Int.*, **42**, 6648 (2016)
44. N.S.Waluyo, R.H.Song, S.B.Lee, T.H.Lim, S.J.Park, J.W.Lee. *J. Electrochem. Soc.*, **163**, F1245 (2016)
45. B.Talic, S.Molin, K.Wiik, P.V.Hendriksen, H.Lein. *J. Power Sources*, **372**, 145 (2017)
46. F.Smeacetto, A.D.Miranda, S.C.Polo, S.Molin, D.Boccaccini, M.Salvo, A.R.Boccaccini. *J. Power Sources*, **280**, 379 (2015)
47. Z.Sun, R.Wang, A.Y.Nikiforov, S.Gopalan, U.B.Pal, S.N.Basu. *J. Power Sources*, **378**, 125 (2018)
48. M.Zarabian, A.Y.Yar, S.Vafaeenezhad, M.A.Faghihi Sani, A.Simchi. *J. Eur. Ceram. Soc.*, **33**, 1815 (2013)
49. M.Matsuda, M.Hashimoto, C.Matsunaga, T.S.Suzuki, Y.Sakka, T.Uchikoshi. *J. Eur. Ceram. Soc.*, **36**, 4077 (2016)
50. N.A.Baharuddin, A.Muchtar, M.R.Somalu, A.Sam, A.H.Rahman. *Ceramics-Silikáty*, **60** (2), 115 (2016)
51. N.A.Baharuddin, A.Muchtar, M.R.Somalu, A.B.Sulong, H.Abdullah. *Sains Malaysia*, **45**(3), 459 (2016)
52. Y.Itagaki, J.Cui, N.Ito, H.Aono, H.Yahiro. *ECS Trans*, **85**, 779 (2018)
53. J.S.Cherng, M.Y.Ho, T.H.Yeh, W.H.Chen. *Ceram. Int.*, **38** (S1), S477 (2012)
54. E.G.Kalinina, E.Y.Pikalova, A.A.Kolchugin, S.M.Pikalov, A.S.Kaigorodov. *Solid State Ionics*, **302**, 126 (2017)
55. D.Das, R.Basu. *Mater. Res. Bull.*, **48**, 3254 (2013)
56. S.S.Dukhin, B.V.Derjaguin. In *Surface and Colloid Sciences*. Vol. 7. (Ed. E.Matijevich). (New York: Wiley-Interscience, 1974). P. 335
57. O.O.Van der Biest, L.J.Vandeperre. *Annu. Rev. Mater. Sci.*, **29**, 327 (1999)
58. O.Stern. *Z. Electrochem.*, **30**, 508 (1924)
59. D.C.Grahame. *Chem. Rev.*, **41**, 441 (1947)
60. O'M.Bockris, M.A.V.Devanathan, K.Mueller. *Proc. R. Soc. London, Ser. A*, **274**, 55 (1963)
61. V.S.Krylov. *Electrochim. Acta*, **9**, 1247 (1964)
62. S.S.Dukhin, B.V.Deryagin. *Elektroforez*. (Electrophoresis). (Moscow: Nauka, 1975). 248 p.
63. *Dvoinoi Sloi i Elektrodnaya Kinetika*. (Double Layer and Electrode Kinetics) (Moscow: Nauka, 1981)
64. S.S.Dukhin. *Elektroprovodnost' i Elektrokineticheskie Svoistva Dispersnykh Sistem*. (Electrical Conductivity and Electrokinetic Properties of Dispersed Systems). (Kiev: Naukova Dumka, 1975)
65. B.V.Deryaguin, L.D.Landau. *Acta Physicochim. USSR*, **14**, 633 (1941)
66. E.J.W.Verwey, J.Th.G.Overbeek. *Theory of the Stability of Lyophobic Colloids*. (Amsterdam: Elsevier, 1948). 205 p.
67. K.S.Birdi. In *Handbook of Surface and Colloid Chemistry*. (4th Edn). (Ed. K.S.Birdi). (Boca Raton, FL: CRC Press, 2015). P. 708
68. J.H.Dickerson, A.R.Boccaccini. *Electrophoretic Deposition of Nanomaterials*. (New York: Springer-Verlag, 2012). 376 p.

69. R.J.Hunter. In *Zeta Potential in Colloid Science: Principles and Applications. Colloid Science*. Vol. 2. (3rd Edn). (Eds R.H.Ottewill, R.L.Rowell). (London; Academic Press, 1981). 398p.
70. D.C.Henry. *Proc. R. Soc. London, Ser. A*, **133**, 106 (1931)
71. R.W.O'Brien, L.R.White. *J. Chem. Soc., Faraday Trans. 2*, **74**, 1607 (1978)
72. A.S.Dukhin, P.J.Goetz, T.H.Wines, P.Somasundaran. *Colloids Surf., A*, **173**, 127 (2000)
73. R.W.O'Brien. *J. Fluid. Mechan.*, **190**, 71 (1988)
74. R.W.O'Brien, B.R.Midmore, A.Lamb, R.J.Hunter. *Faraday Discuss. Chem. Soc.*, **90**, 301 (1990)
75. *Mezhgosudarstvennyi Standart GOST ISO 13099-2-2016. Gosudarstvennaya Sistema Obespecheniya Edinstva Izmerenii. Metody Opredeleniya Dzeta-Potentsiala. Chast' 2. Opticheskie Metody*. (Interstate Standard GOST ISO 13099-2-2016. State System for Ensuring the Uniformity of Measurements. Zeta Potential Determination Methods. Part 2. Optical Methods). (Moscow: Standartinform, 2016)
76. H.E.Albrecht, M.Borys, Damasche, C.Tropea. *Laser Doppler and Phase Doppler Measurement Techniques*. (Berlin, Heidelberg: Springer-Verlag, 2003)
77. S.Bhattacharjee. *J. Control. Release*, **235**, 337 (2016)
78. C.Felix, A.Yaroshchuk, S.Pasupathi, B.G.Pollet, M.P.Bondarenko, V.I.Kovalchuk, E.K.Zholkovskiy. *Adv. Colloid Interface Sci.*, **211**, 77 (2014)
79. *Mezhgosudarstvennyi Standart GOST 8.653.1-2016. Gosudarstvennaya Sistema Obespecheniya Edinstva Izmerenii. Metody Opredeleniya Dzeta-Potentsiala. Chast' 1. Electrokineticheskie Metody*. (Interstate Standard GOST 8.653.1-2016. State System for Ensuring the Uniformity of Measurements. Zeta Potential Determination Methods. Part 1. Electrokinetic Methods). (Moscow: Standartinform, 2016)
80. P.Sarkar, P.S.Nicholson. *J. Am. Ceram. Soc.*, **79**, 1987 (1996)
81. H.C.Hamaker, E.J.W.Verwey. *Trans. Faraday Soc.*, **36**, 180 (1940)
82. H.Koelmans. *Philips Res. Rep.*, **10**, 161 (1955)
83. F.Grillon, D.Fayeulle, M.Jeandin. *J. Mater. Sci. Lett.*, **11**, 272 (1992)
84. H.Hadraba, D.Drdlik, Z.Chlup, K.Maca, I.Dlouhy. *Key Eng. Mater.*, **507**, 209 (2012)
85. B.Ferrari, R.Moreno. *J. Eur. Ceram. Soc.*, **30**, 1069 (2010)
86. P.M.Biesheuvel, H.Verweij. *J. Am. Ceram. Soc.*, **82**, 1451 (1999)
87. M.Gonzalez-Cuenca, P.M.Biesheuvel, H.Verweij. *AIChE J.*, **46**, 626 (2000)
88. B.Ferrari, R.Moreno, J.A.Cuesta. *Key Eng. Mater.*, **314**, 175 (2006)
89. O.Van der Biest, S.Put, G.Anne, J.Vleugels. *J. Mater. Sci.*, **39**, 779 (2004)
90. L.Stappers, L.Zhang, O.Van der Biest, J.Fransaer. *J. Colloid Interface Sci.*, **328**, 436 (2008)
91. L.Stappers, L.Zhang, O.Van der Biest, J.Fransaer. *Key Eng. Mater.*, **412**, 9 (2009)
92. A.J.Pascall, K.T.Sullivan, J.D.Kuntz. *J. Phys. Chem. B*, **117**, 1702 (2013)
93. J.S.Park, D.Saintillan. *Key Eng. Mater.*, **507**, 47 (2012)
94. Yu.L.Klimontovich. *Physics-Uspekhi*, **37**, 737 (1994)
95. B.Giera, L.A.Zepeda-Ruiz, A.J.Pascall, J.D.Kuntz, C.M.Spadaccini, T.H.Weisgraber. *J. Electrochem. Soc.*, **162**, D3030 (2015)
96. B.Giera, L.A.Zepeda-Ruiz, A.J.Pascall, T.H.Weisgraber. *Langmuir*, **33**, 652 (2017)
97. D.Bartuschata, U.Rude. *J. Comput. Sci.*, **27**, 147 (2018)
98. R.Mayén-Mondragón, G.Falk, R.Clasen, R.Moreno. *J. Am. Ceram. Soc.*, **95**, 593 (2011)
99. R.Mayén-Mondragón, J.Genesca-Llongueras. *ECS Trans.*, **76** (1), 53 (2017)
100. FlexPDE, PDE Solutions, http://www.pdesolutions.com (Last accessed on 06.09.2019)
101. M.Z.Bazant, T.M.Squires. *Curr. Opin. Colloid. Interface Sci.*, **15**, 203 (2010)
102. Y.Daghighi; D.Li. *Microfluid Nanofluid*, **9**, 593 (2010)
103. A.V.Delgado, F.González-Caballero, R.J.Hunter, L.K.Koopal, J.Lyklema. *J. Colloid. Interface Sci.*, **309**, 194 (2007)
104. O.Schnitzer, E.Yariv. *Phys. Fluids*, **26**, 122002 (2014)
105. https://www.mtm.kuleuven.be/Onderzoek/Ceramics/old-info/EPD (Last accessed on 06.09.2019)
106. I.Zhitomirsky. *Adv. Colloid Interface*, **97**, 279 (2002)
107. J.Wu, Y.Jiang, C.Johnson, X.Liu. *J. Power Sources*, **177**, 376 (2008)
108. N.V.Demeneva, S.I.Bredikhin. *Russ. J. Electrochem.*, **50**, 725 (2014)
109. W.Lee, J.U.Lee, H.-J.Cha, J.-H.Byun. *RSC Adv.*, **3**, 25609 (2013)
110. E.G.Kalinina, E.Yu.Pikalova, A.V.Menshikova, I.V.Nikolaenko. *Solid State Ionics*, **288**,110 (2016)
111. A.Panigrahi, L.Besra, B.P.Singh, S.P.Sinha, S.Bhattacharjee. *Adv. Powder Technol.*, **22**, 570 (2011)
112. C.Fleckenstein, C.Mochales, S.Frank, F.Kochbeck, R.Zehbe, C.Fleck, W.D.Mueller. *Adv. Appl. Ceram.*, **113** (1), 35 (2013)
113. C.Mochales, S.Frank, R.Zehbe, T.Traykova, C.Fleckenstein, A.Maerten, C.Fleck, W.D.Mueller. *Phys. Chem. B*, **117**, 1694 (2012)
114. R.Zehbe, C.Mochales, D.Radzik, W.-D.Müller, C.Fleck. *J. Eur. Ceram. Soc.*, **36**, 357 (2016)
115. R.N.Basu, C.A.Randall, M.J.Mayo. *J. Am. Ceram. Soc.*, **84**, 33 (2001)
116. J.Tabellion, R.Clasen. *J. Mater. Sci.*, **39**, 803 (2004)
117. S.-M.Yu, K.-T.Lee. *J. Korean Ceram. Proc. Soc.*, **52**, 315 (2015)
118. S.-M.Yu, K.-T.Lee. *J. Ceram. Proc. Res.*, **17**, 290 (2016)
119. G.Falk, K.Klein, C.Rivinius. *Online Chapter 1: Oxide Ceramic Functional Thin Layer Processing by Thermal and Laser Sintering of Green Layers*. INTECH open science, 2013; https://www.intechopen.com/books/sintering-applications/oxide-ceramic-functional-thin-layer-processing-by-thermal-and-laser-sintering-of-green-layers (Last accessed on 06.09.2019)
120. M.Ammam. *RSC Adv.*, **2**, 7633 (2012)
121. A.Chávez-Valdez, A.R.Baccaccini. *Electrochem. Acta*, **65**, 70 (2012)
122. B.Neirinck, O.Van der Biest, J.Vleugels. *J. Phys. Chem. B*, **117**, 1516 (2013)
123. L.Besra, T.Uchikoshi, T.S.Suzuki, Y.Sakka. *J. Eur. Ceram. Soc.*, **29**, 1837 (2009)
124. B.Neirinck, J.Fransaer, O.Van der Biest, J.Vleugels. *Electrochem. Commun.*, **11**, 57 (2011)
125. O.E.Oskouyi, M.Shahmiri, A.Maghsounipour, M.Hasheminiasari. *J. Alloys Compd.*, **785**, 220 (2019)
126. E.G.Kalinina, E.Yu.Pikalova, A.P. Safronov. *Russ. J. Appl. Chem.*, **90**, 701 (2017)
127. E.G.Kalinina, E.Yu.Pikalova, V.D.Zhuravlev, S.V.Scherbinin, A.P.Safronov. *Russ. J. Appl. Chem.*, **90**, 862 (2017)
128. B.Ferrari, R.Moreno. *J. Electrochem. Soc.*, **147**, 2987 (2000)
129. H.Negishi, K.Yamaji, N.Sakai, T.Horita, H.Yanagishita, H.Yokokawa. *J. Mater. Sci.*, **39**, 833 (2004)
130. E.G.Kalinina, O.M.Samatov, A.P.Safronov. *Inorg. Mater.*, **52**, 858 (2016)
131. D.Das, R.N.Basu. *J. Alloys Compd.*, **729**, 71 (2017)
132. E.G.Kalinina, A.A.Efimov, A.P.Safronov. *Thin Solid Films*, **612**, 66 (2016)
133. T.Uchikoshi, K.Ozawa, B.D.Hatton, Y.Sakka. *J. Mater. Res.*, **16**, 321 (2001)

134. J.S.Cherng, J.R.Sau, C.C.Chung. *J. Solid State Electrochem.*, **12**, 925 (2008)
135. T.Talebi, B.Raissi, A.Maghsoudipour. *Int. J. Hydrogen Energy*, **35**, 9434 (2010)
136. T.Ishihara, K.Sato, Y.Takita. *J. Am. Ceram. Soc.*, **79**, 913 (1996)
137. Y.Fukada, N.Nagarajan, W.Mekky. *J. Mater. Sci.*, **39**, 787 (2004)
138. *Encyclopedia of Reagents for Organic Synthesis*. (Ed. L.Paquette). (New York: Wiley, 2004)
139. S.Panigrahi, S.Bhattacharjee, L.Besra, B.P.Singh, S.P.Sinha. *J. Eur. Ceram. Soc.*, **30**,1097 (2010)
140. M.J.López-Robledo, J.Silva-Treviño, T.Molina, R.Moreno. *J. Eur. Ceram. Soc.*, **33**, 297 (2013)
141. Patent US 7683098 (2010)
142. S.Chibowski, M.Wiśniewska, T.Urban. *Adsorbtion*, **16**, 321 (2010)
143. S.Bonnas, J.Tabellion, J.Hausselt. *Key Eng. Mater.*, **314**, 69 (2006)
144. J.A.Lewis. *J. Am. Ceram. Soc.*, **83**, 2341 (2000)
145. H.Xu, I.P.Shapiro, P.Xiao. *Key Eng. Mater.*, **412**, 165 (2009)
146. S.H.Amirnordin, H.A.Rahman, H.Z.Abdullah, H.Taib. *Adv. Mater. Res.*, **488 – 489**, 1358 (2012)
147. P.Sarkar, X.Huang. *J. Am. Ceram. Soc.*, **76**, 1055 (1993)
148. D.A.H.Hanaor, M.Michelazzi, C.Leonelli, C.C.Sorrell. *J. Eur. Ceram. Soc.*, **32**, 235 (2012)
149. H.Xu, I.P.Shapiro, P.Xiao. *J. Eur. Ceram. Soc.*, **30**, 1105 (2010)
150. H.Ichiboshi, K.Myoujin, N.Kodera, T.Ogihara. *Key Eng. Mater.*, **566**, 137 (2013)
151. J.Will, M.K.M.Hruschka, L.Gubler, L.J.Gauckler. *J. Am. Ceram. Soc.*, **84**, 328 (2001)
152. I.N.Sora, R.Pelosato, A.Simone, L.Montanaro, F.Maglia, G.Chiodelli. *Solid State Ionics*, **177**, 1985 (2006)
153. I.Krkljuš, Z.Branković, K.Duriš, V.Vukotić, G.Branković, S.Bernik. *Int. J. Appl. Ceram. Tecnol.*, **5**, 548 (2008)
154. E.G.Kalinina, A.P.Safronov, Yu.A.Kotov. *Russ. J. Electrochem.*, **47**, 671 (2011)
155. L.Hui, P.Xueman, X.Mingxia, X.Tingxian. *Mater. Sci. Eng. A*, **465** (1 – 2), 13 (2007)
156. E.Jothinathan, O.Van der Biest, J.Vleugels. *Adv. Appl. Ceram.*, **111**, 459 (2012)
157. I.Zhitomirsky, A.Petric. *J. Eur. Ceram. Soc.*, **20**, 2055 (2000)
158. C.Szepanski, J.Grobe-Brauckmann, C.Argirusis. *Key Eng. Mater.*, **412**, 209 (2009)
159. F.Chen, M. Liu. *J. Eur. Ceram. Soc.*, **21**, 127 (2001)
160. Y.Sakka, T.Uchikoshi. *KONA Powder Part. J.*, **28**, 74 (2010)
161. M.J.Santillán, A.Caneiro, N.Quaranta, A.R.Boccaccini. *J. Eur. Ceram. Soc.*, **29** 1125 (2009)
162. G.Suarez, N.T.K.Nguyen, N.M.Rendtorff, Y.Sakka, T.Uchikoshi. *Ceram. Int.*, **42**, 19283 (2016)
163. L.Fan, B.Zhu, P.-C.Su, C.He. *Nano Energy*, **45**, 148 (2018)
164. J.Choi, Y.Jung, J.Kim, D.Shin. *Ceram. Int.*, **39**, S663 (2013)
165. Yu.A.Kotov, V.V.Osipov, M.G.Ivanov, O.M.Samatov, V.V.Platonov, E.I.Azarkevich, A.M.Murzakaev, A.I.Medvedev. *Techn. Phys.*, **47**, 1420 (2002)
166. M.Ivanov, Yu.Kotov, V.Lisenkov, V.Osipov, V.Platonov, V.Solomonov. *Adv. Sci. Technol.*, **45**, 291 (2006)
167. V.V.Osipov, Yu.A.Kotov, M.G.Ivanov, O.M.Samatov, V.V.Lisenkov, V.V.Platonov, A.M.Murzakaev, A.I.Medvedev, E.I.Azarkevich. *Laser Phys.*, **16**, 116 (2006)
168. A.P.Safronov, E.G.Kalinina, T.A.Smirnova, D.V.Leiman, A.V.Bagazeev. *Russ. J. Phys. Chem. A*, **84**, 2122 (2010)
169. E.G.Kalinina, N.A.Lyutyagina, D.V.Leiman, A.P.Safronov. *Nanotechnol. Russ.*, **9** (5 – 6), 274 (2014)
170. Y.Itagaki, Y.Yamamoto, H.Aono, H.Yahiro. *J. Ceram. Soc. Jpn.*, **125**, 528 (2017)
171. A.R.Studart, E.Amstad, L.J.Gauckler. *Langmuir*, **23**, 1081 (2007)
172. I.Zhitomirsky, A.Petric. *Mater. Lett.*, **46**, 1 (2000)
173. K.Raju, D.-H.Yoon. *Mater. Lett.*, **110**, 188 (2013)
174. L.Jia, Z.Lü, X.Huang, Z.Liu, K.Chen, X.Sha, G.Li, W.Su. *J. Alloys Compd.*, **424**, 299 (2006)
175. K.Kobayashi, I.Takahashi, M.Shiono, M.Dokiya. *Solid State Ionics*, **152 – 153**, 591 (2002)
176. K.Yamaji, H.Kishimoto, Y.Xiong, T.Horita, N. Sakai, H.Yokokawa. *Solid State Ionics*, **175**, 165 (2004)
177. S.Nakayama, M.Miyayama. *Key Eng. Mater.*, **350**, 175 (2007)
178. D.R.Ou, T.Mori, F.Ye, M.Miyayama, S.Nakayama, J.Zou. *J. Electrochem. Soc.*, **156**, B825 (2009)
179. M.-Y.Cheng, C.-Y.Shiau, P.-H.Liu, J.-C.Chang. *J. Solid State Electrochem.*, **15**, 773 (2011)
180. F.Bozza, R.Polini, E.Traversa. *Fuel Cells*, **8**, 344 (2008)
181. K.Z.Fung, T.Y.Chen. *Solid State Ionics*, **188**, 64 (2011)
182. E.D.Bartolomeo, M.Zunic, L.Chevallier, A.D'Epifanio, S.Licoccia, E.Traversa. *ECS Trans.*, **25**, 577 (2009)
183. M.Zunic, L.Chevallier, E.D.Bartolomeo, A.D.Epifanio, S.Licoccia, E.Traversa. *Fuel Cells*, **11**, 165 (2011)
184. C.Argirusis, J.Grosse-Brauckmann, G.Sourkouni, G.Taillades, J.Roziere. *Key Eng. Mater.*, **412**, 125 (2009)
185. B.Choudhary, S.Anwar, L.Besra, S.Anwar. *Int. J. Appl. Ceram. Technol.*, **16**, 1022 (2019)
186. F.Bozza, N.Bonanos. *Solid State Ionics*, **213**, 98 (2012)
187. E.G.Kalinina, E.Yu.Pikalova, A.P.Safronov. *Inorg. Mater.*, **53**, 987 (2017)
188. M.Asamoto, H.Yamaura, H.Yahiro. *J. Power Sources*, **196**, 1136 (2011)
189. Y.Itagaki, F.Matsubara, M.Asamoto, H.Yamaura, H.Yahiro, Y.Sadaoka. *ECS Trans.*, **7**, 1319 (2007)
190. Y.Itagaki, S.Watanabe, T.Yamaji, M.Asamoto, H.Yahiro, Y.Sadaoka. *J. Power Sources*, **214**,153 (2012)
191. M.J.Santillan, A.Caneiro, F.C.Lovey, N.Quaranta, A.R.Boccaccini. *Int. J. Appl. Ceram. Tecnol.*, **7** (1), 30 (2010)
192. Y.Itagaki, K.Shinohara, S.Yamaguchi, H.Yahiro. *J. Ceram. Soc. Jpn.*, **123**, 235 (2015)
193. M.Asamoto, S.Miyake, Y.Itagaki, Y.Sadaoka, H.Yahiro. *Catalysis Today*, **139**, 77 (2008)
194. Z.Wang, N.Zhang, J.Qiao, K.Sun, P.Xu. *Electrochem. Commun.*, **11**, 1120 (2009)
195. L.V.Kovalev, M.V.Yarmolich, M.L.Petrova, J.Ustarroz, H.A.Terryn, N.A.Kalanda, M.L.Zheludkevich. *ACS Appl. Mater. Int.*, **6**, 19201 (2014)
196. M.Bobruk, S.Molin, M.Chen, T.Brylewski, P.V.Hendriksen. *Mater. Lett.*, **213**, 394 (2018)
197. S.Molin, A.G.Sabato, H.Javed, G.Cempura, A.R.Boccaccini, F.Smeacetto. *Mater. Lett.*, **218**, 329 (2018)
198. Y.Zhang, A.Javed, M.Zhou, S.Liang, P.Xiao. *Int. J. Appl. Ceram. Technol.*, **11**, 332 (2014)
199. R.Wang, Z.Sun, U.B.Pal, S.Gopalan, S.N.Basu. *J. Power Sources*, **376**, 100 (2018)
200. Z.Sun, S.Gopalan, U.B.Pal, S.N.Basu. *Surf. Coat. Technol.*, **323**, 49 (2017)
201. R.Irankhah, B.Raissi, A.Maghsoudipour, A.Irankhah, S.Ghashghai. *J. Mater. Eng. Perform.*, **25**, 1515 (2016)
202. T.Ishihara, K.Shimose, T.Kudo, H.Nishiguchi, T.Akbay, Y.Takita. *J. Am. Ceram. Soc.*, **83**, 1921 (2000)
203. R.N.Basu, O.Altin, M.J.Mayo, C.A.Randall, S.Eser. *J. Electrochem. Soc.*, **148**, A506 (2001)
204. Z.Peng, M.Liu. *J. Am. Ceram. Soc.*, **84**, 283 (2001)
205. Y.H.Lee, C.W.Kuo, C.J.Shin, I.M.Hung, K.Z.Fung, S.B.Wen, M.C.Wang. *Mater. Sci. Eng. A*, **445 – 446**, 347 (2007)
206. K.Yang, J.-H.Shen, K.-Y.Yang, I.-M.Hung, K.-Z.Fung, M.-C.Wang. *J. Alloys Compd.*, **436**, 351 (2007)
207. E.G.Kalinina, N.M.Bogdanovich, D.I.Bronin, E.Yu.Pikalova, A.A.Pankratov. *Russ. J. Appl. Chem.*, **92**, 191 (2019)

208. S.Cherng, C.C.Wu, W.H.Chen, T.H.Yeh. *Ceram. Int.*, **39**, S601 (2013)
209. L.Besra, C.Compson, M.Liu. *J. Power Sources*, **173**, 130 (2007)
210. T.Uchikoshi, S.Furumi, N.Shirahata, T.S.Suzuki, Y.Sakka. *J. Am. Ceram. Soc.*, **91**, 1674 (2008)
211. H.T.Suzuki, T.Uchikoshi, K.Kobayashi, T.S.Suzuki, T.Sugiyama, K.Furuya, M.Matsuda, Y.Sakka, F.Munakata. *J. Ceram. Soc. Jpn.*, **117**, 1246 (2009)
212. T.Hosomi, M.Matsuda, M.Miyake. *J. Eur. Ceram. Soc.*, **27**, 173 (2007)
213. D.Das, R.N.Basu. *Adv. Appl. Ceram.*, **113**, 2651 (2014)
214. G.Savo, A.Rainer, A.D'Epifanio, S.Licoccia, E.Traversa. *Mater. Res. Soc. Symp. P*, **835**, K3.1.1 (2005)
215. E.G.Kalinina, E.Yu.Pikalova, A.S.Farlenkov. *Russ. J. Appl. Chem.*, **91**, 934 (2018)
216. M.Matsuda, T.Hosomi, K.Murata, T.Fukui, M.Miyake. *J. Power Sources*, **165**, 102 (2007)
217. F.Harbah, H.Nienburg. *J. Eur. Ceram. Soc.*, **18**, 675 (1998)
218. H.Negishi, N.Oshima, K.Sakaki, K.Haraya, Y.Idemoto, N.Koura, H.Yanagoshita. *Desalination*, **200** (1 – 3), 71 (2006)
219. M.Bredol, J.Micior, S.Klemme. *J. Mater. Sci.*, **49**, 6975 (2014)
220. Patent RF 2638205 C1 (2017)
221. B.A.Horri, C.Selomulya, H.Wang. *Int. J. Hydrogen Energy*, **37**, 19045 (2012)
222. V.V.Ivanov, Yu.A.Kotov, A.S.Lipilin, A.P.Safronov, A.V.Nikonov, E.G.Kalinina, Al.A.Rempel, O.R.Timoshenkova, S.V.Zayats. *Int. J. Altern. Energy Ecology*, **10** (66), 35 (2008)
223. M.Matsuda, T.Hosomi, K.Murata, T.Fukui, M.Miyake. *Electrochem. Solid State Lett.*, **8** (1), A8 (2005)
224. F.Bozza, R.Polini, E.Traversa. *Electrochem. Commun.*, **11**, 1680 (2009)
225. F.Bozza, R.Polini, E.Traversa. *J. Am. Ceram. Soc.*, **92**, 1999 (2009)
226. B.S.Prakash, R.Pavitra, S.S.Kumar, S.T.Aruna. *J. Power Sources*, **381**, 136 (2018)
227. A.N.Kovalchuk, A.V.Kuz'min, D.A.Osinkin, A.S.Farlenkov, A.A.Solov'ev, A.V.Shipilova, I.V.Ivanov, N.M.Bogdanovich, S.M.Beresnev. *Russ. J. Electrochem.*, **54**, 541 (2018)
228. E.G.Kalinina, E.Yu.Pikalova, A.A.Kolchugin. *Russ. J. Electrochem.*, **54**, 723 (2018)
229. J.Lyagaeva, G.Vdovin, L.Hakimova, D.Medvedev, A.Demin, P.Tsiakaras. *Electrochem. Acta*, **251**, 554 (2017)
230. D.Medvedev, A.Kalyakin, A.Volkov, A.Demin, P.Tsiakaras. *Electrochem. Commun.*, **76**, 55 (2018)
231. A.V.Kuzmin, A.Yu.Stroeva, M.S.Plekhanov, V.P.Gorelov, A.S.Fralenkov. *Int. J. Hydrogen Energy*, **43**, 19206 (2018)
232. N.Kochetova, I.Alyabysheva, I.Animitsa. *Solid State Ionics*, **306**, 118 (2017)
233. E.P.Antonova, A.A.Kolchugin, E.Yu.Pikalova, D.A.Medvedev, N.M.Bogdanovich. *Solid State Ionics*, **306**, 55 (2017)
234. J.Lyagaeva, D.Medvedev, E.Pikalova, S.Plaksin, A.Brouzgou, A.Demin, P.Tsiakaras. *Int. J. Hydrogen Energy*, **42**, 1715 (2017)
235. D.Medvedev, J.Lyagaeva, S.Plaksin, A.Demin, P.Tsiakaras. *J. Power Sources*, **273**, 716 (2015)
236. E.Yu.Pikalova, A.A.Kolchugin, V.A.Sadykov, E.M.Sadovskaya, E.A.Filonova, N.F.Eremeev, N.M.Bogdanovich. *Int. J. Hydrogen Energy*, **43**, 17373 (2018)
237. T.Alston, K.Kendall, M.Palin, M.Prica, P.Windibank. *J. Power Sources*, **71**, 271 (1998)
238. Y.Du, C.Finnerty, J.Jiang. *J. Electrochem. Soc.*, **155**, B972 (2008)
239. A.V.Nikonov, A.V.Spirin, A.S.Lipilin, V.R.Khrustov, S.N.Paranin. *Russ. J. Electrochem.*, **54**, 547 (2018)
240. Y.Gan, C.Ren, M.Lee, C.Yang, X.Xue. *J. Solid State Electrochem.*, **22**, 2929 (2018)
241. C.Ren, Y.Gan, C.Yang, M.Lee, R.D.Green, X.Xue. *J. Appl. Electrochem.*, **48**, 959 (2018)
242. A.Tarutin, A.Kasyanova, J.Lyagaeva, G.Vdovin, D.Medvedev. *J. Energy Chem.*, **40**, 65 (2020)
243. M.Morales, M.E.Navarro, X.G.Capdevila, J.J.Roa, M.Segarra. *Ceram. Int.*, **38**, 3713 (2012)
244. E.V.Shubnikova, M.P.Popov, S.F.Byshkov, S.A.Chizhik, A.P.Nemudry. *Chem. Eng. J.*, **372**, 251 (2019)
245. N.Droushiotis, A.Hankin, C.Rozain, G.H.Kelsall. *J. Electrochem. Soc.*, **161** (3), F271 (2014)
246. S.-M.Yu, K.-T.Lee. *J. Ceram. Proc. Res.*, **17**, 672 (2016)
247. S.-H.Lee, K.-T.Lee. *J. Ceram. Proc. Res.*, **19**, 285 (2018)
248. P.Sarkar, L.Yamarte, H.Rho, L.Johanson. *Int. J. Appl. Ceram. Technol.*, **4**, 103 (2007)
249. S.T.Jamil, M.H.D.Othman, M.A.Rahman, J.Jaafar, A.F.Ismail, K.Li. *J. Eur. Ceram. Soc.*, **35**, 1 (2015)
250. T.Suzuki, Y.Funahashi, T.Yamaguchi, Y.Fujishiro, M.Awano. *Solid State Ionics*, **180**, 546 (2009)
251. T.Yamaguchi, S.Shimizu, T.Suzuki, Y.Fujishiro, M.Awano. *Mater. Lett.*, **62**, 1518 (2008)
252. M.Torrell, A.Morata, P.Kayser, M.Kendall, K.Kendall, A.Tarancón. *J. Power Sources*, **285**, 439 (2015)
253. C.M.Dakwal, W.Bujalski, K.Kendall. *J. Power Sources*, **193**, 241 (2009)
254. Z.Yang, M.Guo, N.Wang, C.Ma, J.Wang, M.Han. *Int. J. Hydrogen Energy*, **42**, 24948 (2017)
255. N.Shaigan, W.Qu, D.G.Ivey, W.Chen. *J. Power Sources*, **195**, 1529 (2010)
256. S.I.Bredikhin, A.A.Zhokhov, E.A.Frolova, N.V.Ledukhovskaya, I.E.Kuritsyna, V.V.Sinitsyn, E.V.Korovkin. *Russ. J. Electrochem.*, **45**, 520 (2009)
257. Z.H.Bi, J.H.Zhu, J.L.Batey. *J. Power Sources*, **195**, 3605 (2010)
258. V.Sauchuk, S.Megel, E.Girdauskaite, N.Trofimenko, M.Kusnezoff, A.Michaelis. *Russ. J. Electrochem.*, **47**, 522 (2011)
259. N.V.Gavrilov, V.V.Ivanov, A.S.Kamenetskikh, A.V.Nikonov. *Surf. Coat. Technol.*, **206**, 1252 (2011)
260. J.Puranen, M.Pihlatie, J.Lagerbom, T.Salminen, J.Laakso, L.Hyvärinen, M.Kylmälahti, O.Himanen, J.Kiviaho, P.Vuoristo. *Int. J. Hydrogen Energy*, **39**, 17246 (2014)
261. J.W.Stevenson, Z.G.Yang, G.G.Xia, Z.Nie, J.D.Templeton. *J. Power Sources*, **231**, 256 (2013)
262. Z.Yang, G.-G.Xia, G.D.Maupin, J.W.Stevenson. *Surf. Coat. Technol.*, **20**, 4476 (2006)
263. G.V.Pattarkine, N.Dasgupta, A.V.Virkar. *J. Electrochem. Soc.*, **155**, B1036 (2008)
264. R.Lacey, A.Pramanick, J.C.Lee, B.Jiang, D.D.Edwards, R.Naum, S.T.Misture. *Solid State Ionics*, **181**, 1294 (2010)
265. W.J.Shong, C.K.Liu, C.Y.Chen, C.C.Peng, H.J.Tu, G.T.Fey, R.Y.Lee, H.M.Kao. *Mater. Chem. Phys.*, **127**, 45 (2011)
266. L.Conceição, L.Dessemond, E.Djurado, M.M.V.M.Souza. *J. Power Sources*, **241**, 159 (2013)
267. J.-J.Choi, J.Ryu, B.-D.Hahn, W.-H.Yoon, B.-K.Lee, J.-H.Choi, D.-S.Park. *J. Alloys Compd.*, **492**, 488 (2010)
268. B.A.Pint. *Oxid. Met.*, **45** (1 – 2), 1 (1996)
269. S.Fontana, R.Amendola, S.Chevalier, P.Piccarod, G.Caboche, M.Viviani, R.Molins, M. Sennour. *J. Power Sources*, **171**, 652 (2007)
270. S.Bose. In *High Temperature Coatings*. (2nd Edn.). (London: Academic Press, Elsevier, 2018). P. 71
271. A.Petric, H.Ling. *J. Am. Ceram. Soc.*, **90**, 1515 (2007)
272. J.Yoo, S.-K.Woo, J.H.Yu, S.Lee, G.W.Park. *Int. J. Hydrogen Energy*, **34**, 1542 (2009)
273. H.Abdoli, P.Alizadeh. *Mater. Lett.*, **80**, 53 (2012)
274. H.Zhu, S.Geng, G.Chen, F.Wang. *J. Alloys Compd.*, **782**, 100 (2019)

275. S.Molino, A.G.Sabato, M.Bindi, P.Leone, G.Cempura, M.Salvo, P.Cabanas, A.R.Boccachini, F.Smeacetto. *J. Eur. Ceram. Soc.*, **37**, 4781 (2017)
276. Y.Liu, J.W.Fergus, C.D.Cruz. *J. Am. Ceram. Soc.*, **96**, 1841 (2013)
277. C.Lee, J.Bae. *Thin Solid Films*, **516**, 6432 (2008)
278. J.C.W. Mah, A.Muchtar, M.R.Somalu, M.J.Chazali. *Int. J. Hydrogen Energy*, **42**, 9219 (2017)
279. T.Brylewski, K.Przybylski. *Mater. Sci. Forum*, **813**, 595 (2008)
280. C.Johnson, R.Gemmen, N.Orlovskaya. *Composites, Part B: Engineering*, **35**, 167 (2004)
281. S.Frangini, A.Masi, L.Della Seta, M.Bianco, J.Van Herle. *J. Electrochem. Soc.*, **165** (2), F97 (2018)
282. S.Fontana, S.Chevalier, G.Caboche. *Oxid. Met.*, **28**, 307 (2012)